Searches for New Charged Long-Lived Particles With the ATLAS Detector Using Disappearing Tracks and Ionization Energy Loss Signatures

by

Nathan Dale Young

A dissertation accepted and approved in partial fulfillment of the

requirements for the degree of

Doctor of Philosophy

in Physics

Dissertation Committee:

Stephanie Majewski, Chair

Graham Kribs, Core Member

Laura Jeanty, Advisor

Ben Elias, Institutional Representative

University of Oregon

Spring 2026

© 2026 Nathan Dale Young
This work is openly licensed via **CC BY-NC 4.0**.

DISSERTATION ABSTRACT

Nathan Dale Young

Doctor of Philosophy in Physics

Title: Searches for New Charged Long-Lived Particles With the ATLAS Detector Using Disappearing Tracks and Ionization Energy Loss Signatures

The search for long-lived particles provides an exciting and well motivated place that Beyond The Standard Model physics could be lurking. This dissertation presents contributions to two complementary ATLAS searches for charged long-lived particles with lifetimes of order 1 ns.

The first extends the ATLAS disappearing track search to previously unexplored $\tilde{\tau}$ benchmark models, including the $\tilde{\tau}$ coannihilation and GMSB scenarios. The observed results are consistent with Standard Model expectations within 2σ, leading to exclusion limits of 320 GeV for a 1 ns lifetime in the CMSSM $\tilde{\tau}$ coannihilation scenario and 300 GeV for a 1 ns lifetime in the GMSB $\tilde{\tau}$ scenario.

The second introduces a new search strategy combining disappearing track signatures with high ionization energy loss. The analysis employs a fully data-driven background estimation using two complementary methods: an ABCD approach and a template-based method. Validation studies demonstrate closure of both techniques, while projected sensitivity studies indicate significantly improved sensitivity to charged long-lived particles with lifetimes near 1 ns.

This dissertation also presents contributions to the development of the ATLAS Inner Tracker for HL-LHC operation, including studies of module performance under thermal cycling and the design of dedicated test infrastructure for loaded local support structures.

Together, these contributions advance both the detector capabilities and analysis techniques required for future charged long-lived particle searches at ATLAS.

This dissertation includes previously published coauthored material.

CURRICULUM VITAE

NAME OF AUTHOR: Nathan Dale Young

GRADUATE AND UNDERGRADUATE SCHOOLS ATTENDED:

University of Oregon, Eugene, OR, USA
University of Arizona, AZ, USA
Pima Community College, AZ, USA

DEGREES AWARDED:

Doctor of Philosophy, Physics, 2026, University of Oregon
Master of Science, Physics, 2022, University of Oregon
Bachelor of Science, Physics, 2020, University of Arizona
Associate of Science, Physics, 2018, Pima Community College

AREAS OF SPECIAL INTEREST:

Long Lived Particle Searches
Silicon Detectors

PROFESSIONAL EXPERIENCE:

Research Assistant, University of Oregon, 2020 - 2026
Undergraduate Research Assistant, University of Arizona, 2019 - 2020

GRANTS, AWARDS AND HONORS:

Department of Energy Office of Science Graduate Student Research Program Recipient
US ATLAS Summer Undergraduate Program for Exceptional Researchers

PUBLICATIONS:

ATLAS Collobration, (2026). "Search for long-lived charginos and τ-sleptons using final states with a disappearing track in pp collisions at $\sqrt{s} = 13$ TeV with the ATLAS detector" *arXiv URL:* `https://arxiv.org/abs/2603.08315` Submitted to JHEP

ACKNOWLEDGEMENTS

First, I would like to thank my wife, Madison, for her unwavering support and patience; for falling in love with me and joining me for a sojourn in California for a year. Her encouragement during the most challenging parts of this process made completing this PhD possible.

I would also like to thank my parents and grandparents for their constant support and for instilling in me the value of education from an early age.

I also would like to thank my mother-in-law and father-in-law for their generosity and hospitality, and for ensuring I was always well-fed throughout the latter half of my PhD.

I am grateful to my colleagues in ATLAS, especially those at SLAC and Ondrej. Working on this collaboration has given me the opportunity to meet and learn from many exceptional people, and your support, insight, and friendship have helped me grow immensely as both a physicist and a person.

Finally, I would like to thank my advisor Laura for her guidance throughout my PhD. Your mentorship, patience, and expertise have taught me more than could be expressed here, and this work would not have been possible without your support.

To Grandpa, who taught me how to ask questions.

And

To Bebe, who taught me which questions matter most.

TABLE OF CONTENTS

Chapter Page

I. INTRODUCTION 20
II. OVERVIEW AND MOTIVATION 21
2.1. Standard Model of Particle Physics 21
2.1.1. Fermions 21
2.1.2. Bosons 22
2.2. Motivation For Physics Beyond the Standard Model 23
2.3. Supersymmetry 26
2.3.1. Constrained Minimal Supersymmetric Standard Model . . . 28
2.3.2. Gauge Meditated SUSY Breaking 30
2.3.3. Anomaly Mediated SUSY Breaking 31
III. EXPERIMENTAL SETUP 33
3.1. The Large Hadron Collider 33
3.2. The ATLAS Detector 35
3.2.1. Inner Detector 37
3.2.1.1. Pixel Detector 37
3.2.1.2. Semiconductor Tracker 39
3.2.1.3. Transition Radiation Tracker 40
3.2.2. Calorimeters 41
3.2.2.1. Electromagnetic Calorimeter 41
3.2.2.2. Hadronic Calorimeter 42
3.2.3. Muon Spectrometer 42
IV. EXPERIMENTAL UPGRADES 44

Chapter Page

4.1. Phase 1 upgrades . . . 45
4.2. Phase 2 upgrades . . . 45
4.3. ATLAS ITk . . . 45
4.3.1. ITk Strips . . . 46
4.3.2. ITk Pixels . . . 46
V. OBJECT RECONSTRUCTION . . . 58
5.1. Tracking . . . 58
5.1.1. Track Reconstruction . . . 58
5.1.2. Tracklet Reconstruction . . . 60
5.1.3. Vertex Updater . . . 60
5.1.4. Kinked Tracklets . . . 61
5.1.5. Soft Pion . . . 62
5.2. Object Reconstruction . . . 63
5.2.1. Election . . . 63
5.2.2. Muon . . . 64
5.2.2.1. Combined Muon . . . 64
5.2.2.2. Segment-tagged Muon . . . 64
5.2.2.3. Calorimeter-tagged muons . . . 64
5.2.2.4. Extrapolated muons . . . 65
5.2.3. Jet . . . 65
5.2.4. Missing Transverse Energy . . . 65
5.3. Measurements . . . 66
5.3.1. Momentum . . . 66
5.3.2. Momentum Error . . . 67
5.4. dEdx measurements . . . 68

Chapter Page

5.4.1. Small number of collisions . . . 68

5.4.2. Landau . . . 70

5.4.3. Bethe–Bloch . . . 71

VI. DISAPPEARING TRACKS . . . 73

6.1. Preface . . . 73

6.2. Introduction . . . 73

6.3. ATLAS detector . . . 80

6.4. Data and simulated event samples . . . 82

6.5. Event reconstruction . . . 85

6.6. Analysis strategy . . . 91

6.7. Background estimation . . . 93

6.8. Systematic uncertainties . . . 104

6.9. Results . . . 106

6.10. Conclusion . . . 116

VII. DISAPPEARING TRACKS WITH HIGH IONIZATION ENERGY LOSS . . . 117

7.1. Analysis Introduction . . . 117

7.2. Data . . . 117

7.2.0.1. Event selection . . . 118

7.2.0.2. Event retrieval . . . 118

7.2.0.3. Event reconstruction . . . 118

7.3. Simulation . . . 119

7.3.1. Wino . . . 119

7.3.2. Stau . . . 120

7.4. Signal Region and Selections . . . 120

7.4.1. Event Picking . . . 121

Chapter Page

7.4.1.1. Tracklet Momentum 122

7.4.1.2. Event Missing Transverse Energy 122

7.4.1.3. Track Isolation 122

7.4.2. Baseline Tracklet Selections 122

7.4.3. Signal Regions: inclusive Regions 125

7.4.4. Signal Regions: kinked tracklet 125

7.4.4.1. Kinked veto 125

7.4.4.2. Kinked tracklet requirement 127

7.5. Background Estimation 128

7.5.1. ABCD Method in $\mathrm{d}E/\mathrm{d}x$ and p_T 129

7.5.2. Two component $\mathrm{d}E/\mathrm{d}x$ template 133

7.5.2.1. Template Extraction: MIPs 134

7.5.3. Template Extraction: Fakes 134

7.6. Results and Conclusion 138

VIII. CONCLUSION 139

REFERENCES CITED 141

LIST OF FIGURES

Figure Page

2.1. Standard model elementary particles on the left and their superpartners on the right. [2]. 21

2.2. 1 loop Higgs quantum corrections example from a) fermions and b) SUSY scalars 24

2.3. Rotation curves for NGC 6503, Note the circle marks with error bars are the measured data. [4] 25

3.1. Schematic of the LHC accelerator complex [12], showing the sequence of accelerators used to prepare and inject proton beams into the LHC ring. Image credit:CERN. 34

3.2. Schematic view of the ATLAS detector [14], showing the main subsystems arranged around the interaction point. Image credit: CERN 35

3.3. Left: Schematic view of the ID, showing the beam pipe, pixel barrel, SCT barrel, and TRT. Right: schematic view of charged particle track; red stars are cluster hits, the track is in black, green indicates the intersection of the track with the silicon layer, and blue represents the distance between the track and cluster hit on the surface of the silicon. Image credit: CERN [14]. 38

3.4. Schematic view of silicon microstrip detector. Credit: [17] 40

3.5. Schematic view of the Calorimeters[14], showing the electromagnetic and hadronic calorimeters. Image credit: CERN. 41

3.6. Schematic layout of the ATLAS MS showing the barrel and end-cap regions along with the locations of the different detector technologies used for muon tracking and triggering. Credit: CERN [18] 43

Figure Page

4.1. Cut away view of ITk in one quadrant only. Layout is only in positive z direction. Full detector is symmetric about the z=0 and extends in a full cylinder around beam line. 4.1(a) Shows one quadrant of the full ITk. 4.1(b) Shows one quadrant of ITk Pixels. 48

4.2. View of ITk triplet and quad modules. Note the attached power and data flex cables attached. 49

4.3. Schematic of the quarter shell support structure of the inner pixel system. 50

4.4. Schematic of ITk service chain. 51

4.5. CAD models of boxes used for loaded local supports. 54

4.6. CAD models of the various staves for Layer 1 and Layer 2. Note the flexes are bend into shape of final cable routing. 55

4.7. Disconnected bump bonds from one sensor before and after 100 thermal cycles. Blue pixels indicate disconnected bump bonds. Red pixels indicate connected bump bonds. 57

5.1. Schematic view of the various signals of different common SM particles [23]. 63

5.2. Schematic view of sagitta measurement for three hits in silicon. Note, not draw to scale. 68

5.3. Bethe-Bloch $\mathrm{d}E/\mathrm{d}x$ for muons incident on silicon [5]. 72

6.1. Summary of exclusion limits on $\tilde{\tau} \rightarrow \tilde{G}\tau$ from various ATLAS searches [28]. 74

6.2. Representative signal diagrams for (a) the electroweak production of $\tilde{\chi}_1^{\pm}\tilde{\chi}_1^0$, and τ-slepton pair production in (b) CMSSM-inspired or (c) GMSB-inspired SUSY models. The signal signature consists of a long-lived $\tilde{\chi}_1^{\pm}$ or τ-slepton, missing transverse momentum, and quarks or gluons, which are observed as jets (j). When considering the electroweakino scenarios, the production of $\tilde{\chi}_1^{+}\tilde{\chi}_1^{-}$ is also considered, as is $\tilde{\chi}_1^{\pm}\tilde{\chi}_2^0$ specifically in the higgsino scenario. 79

6.3. Representative distributions related to the reconstruction of tracklets and charged pions: (a) event yields and reconstruction efficiencies for three- and four-layer tracklet reconstruction as a function of $\tilde{\chi}_1^{\pm}$ decay radius; (b) BDT output score used to judge if an event contains a low-energy pion, showing the training dataset (solid histogram) and the test dataset (points); (c) event yields and reconstruction efficiency for charged pions as a function of the true pion transverse momentum as measured in the lab-frame, where the acceptance includes all charged-pion reconstruction effects but not geometric acceptance from tracklet reconstruction (which is assumed to already have been reconstructed). The true transverse momentum is defined as $p_{\mathrm{T}} = \sqrt{p_x^2 + p_y^2}$ in the global detector coordinate system with the z-axis along the beam pipe. For (a) and (c) the filled histogram displays the total yield without applying a selection, while the dashed lines present the yield after applying the tracklet selection or tracklet+pion selection. The points denote the reconstruction efficiency. A representative higgsino signal scenario with $m(\tilde{\chi}_1^{\pm}) = 250\,\mathrm{GeV}$ and $\tau(\tilde{\chi}_1^{\pm}) = 0.04\,\mathrm{ns}$ is shown. 90

6.4. Schematic diagram illustrating how the signal scenarios are detected and how the background processes may enter the SR selections. The detector layers are not shown to scale. Taken from Ref. [71]. 93

6.5. Individual components used in the estimation of the fake background: (a) shows the original template, $N^{\mathrm{TRfake}}(p_{\mathrm{T}})$, as a solid line. The templates after the application of the transfer factors are shown as dashed lines; (b) shows the $|d_0|/\sigma(d_0)$ dependence introduced when extrapolating over $|z_0 \sin\theta|$ and the binwise, with respect to $|d_0|/\sigma(d_0)$, transfer factors $\mathrm{TF}^{\mathrm{fake}}_{d_0\text{-correction}}(d_0)$ used to remove the dependence; and (c) shows a comparison between the pure fake and hybrid fake contributions and the p_{T}-dependent transfer factors $\mathrm{TF}^{\mathrm{fake}}_{\mathrm{hybrid}}(p_{\mathrm{T}})$ used to extrapolate from the template region that contains pure fakes to the SR, which contains a mixture of hybrid and pure fake components. 96

Figure Page

6.6. Individual contributions used in the estimation of the electron background: (a) presents the original electron p_{T} template, $N^{\mathrm{TRe}}(p_{\mathrm{T}})$, as a solid line, with the templates also shown after the application of each transfer/smearing factor as dashed lines; (b) shows the transfer factor, $\mathrm{TF}^{e}_{\text{tracklet}}$, used to correct for the likelihood of reconstructing an electron track as a tracklet; (c) shows the transfer factors, $\mathrm{TF}^{e}_{\text{calo-veto}}$, used to correct for the likelihood of an electron not being associated with a calorimeter energy cluster; and (d) shows the smearing functions, f^{e}_{smear}, used to correct the measured electron track p_{T} to the tracklet p_{T} (defined on the figure). While the tracklet p_{T} template and the TFs are dependent upon both p_{T} and η, the components are shown with their dependence upon the tracklet p_{T} distribution as a representative distribution. 98

6.7. Schematic diagram for the background estimation strategy, describing the usage of template regions (TRs), and relaxed selections to calculate transfer factors (TFs) before performing the fit using control regions (CRs). The kinematic regions are orthogonal due to selections on $E_{\mathrm{T}}^{\mathrm{miss}}$, tracklet p_{T}, and tracklet $E_{\mathrm{T}}^{\mathrm{clus}}$, with high calorimeter energies ('calo-side') dominated by the hadron background, and low calorimeter energies ('calo-veto') dominated by the fake background. 102

6.8. A summary of the systematic uncertainties affecting the background estimates in the SRs after the likelihood fit to data in the CRs is performed ('Post-fit'). The total uncertainty is indicated by a solid black line. The individual uncertainties may not sum in quadrature to the total uncertainty, due to correlations between the different components. The uncertainties arising from the estimation of the fake-tracklet background, which are the dominant uncertainties, are shown as blue dashed lines. 106

6.9. The post-fit yields in the CRs. All statistical and systematic uncertainties are considered in the error bands. Three representative pre-fit signal yields are indicated with dashed lines. . . . 107

Figure Page

6.10. The post-fit tracklet p_{T} distributions in () $\mathrm{VR}^{\mathrm{4MidS}}$, () $\mathrm{VR}^{\mathrm{3High0}\pi}$, and () $\mathrm{VR}^{\mathrm{3Mid1}\pi}$. The dashed vertical line denotes the boundary between the CR and VR selections. The pre-fit signal distributions are indicated with dashed lines. The lower pad shows the ratio of the observed yields to the post-fit predicted background yields. The last bin includes overflow events. All statistical and systematic uncertainties are considered in the error bands. 108

6.11. The observed and expected event yields in the VRs and SRs. The lower pads show the ratio of the observed yields to the post-fit predicted background yields and the statistical significance [139] of the observed data. A red arrow is used to indicate that a ratio value is outside the displayed interval. The background estimates are calculated from the background-only fit. All statistical and systematic uncertainties are considered in the error bands. Three representative pre-fit signal yields are indicated with dashed lines. . . . 109

6.12. The post-fit tracklet p_{T} distributions in (a) $\mathrm{SR}^{\mathrm{4High}}$, (b) $\mathrm{SR}^{\mathrm{4Mid}}$, (c) $\mathrm{SR}^{\mathrm{3High0}\pi}$, and (d) $\mathrm{SR}^{\mathrm{3High1}\pi}$. The dashed vertical line denotes the boundary between the CR/VR and SR selections. The lower pad shows the ratio of the observed data yields to the post-fit predicted background estimates. A red arrow is used to indicate that a ratio value is outside the displayed interval. The last bin includes overflow events. All statistical and systematic uncertainties are considered in the error bands. Three representative pre-fit signal yields are indicated with dashed lines. 113

6.13. The expected (dashed line) and observed (solid line) 95% CL exclusion contours for wino production as a function of the chargino mass and () lifetime, or () mass splitting of the electroweakinos. The dotted lines indicates the $\pm\sigma_{\mathrm{theory}}$ from signal cross-section uncertainties, while the solid band indicates the $\pm\sigma_{\mathrm{exp}}$ from experimental systematic uncertainties and statistical uncertainties on the data yields. The solid grey area shows the region excluded by Ref. [71]. The dashed-dotted line is the prediction of the chargino lifetime or wino mass splitting as a function of the chargino mass as predicted by the SM loop corrections [42]. 114

Figure Page

6.14. The expected (dashed line) and observed (solid line) 95% CL exclusion contours for higgsino production as a function of the chargino mass and () lifetime, or () mass splitting of the electroweakinos. The dotted lines indicates the $\pm\sigma_{\text{theory}}$ from signal cross-section uncertainties, while the solid band indicates the $\pm\sigma_{\text{exp}}$ from experimental systematic uncertainties and statistical uncertainties on the data yields. The solid grey area shows the region excluded by Ref. [71]. The dashed-dotted line is the prediction of the chargino lifetime or higgsino mass splitting as a function of the chargino mass as predicted by the SM loop corrections [49]. 114

6.15. The expected (dashed line) and observed (solid line) 95% CL exclusion contours for τ-slepton production in () CMSSM-inspired scenarios and () GMSB-inspired scenario. The dotted lines indicates the $\pm\sigma_{\text{theory}}$ from signal cross-section uncertainties, while the solid band indicates the $\pm\sigma_{\text{exp}}$ from experimental systematic uncertainties and statistical uncertainties on the data yields. 115

7.1. Feynman diagrams for (left) pair-produced charginos and (right) pair-produced staus. 120

7.2. Schematic view of the signal regions. On the left being for decay-agnostic signal regions. On the right being for decay-specific regions. Note that in this case the Δm is specifically the mass splitting between the BSM particle and the sum of decay products. Credit: Yoshifumi Narukawa. 121

7.3. Distributions of the key selection variables for signal and background processes, with $\mathrm{d}E/\mathrm{d}x <$ 1.2 to avoid signal region. (a) MET distribution, (b) p_T, (c) ptcone40 Clear separation between signal and background is observed, motivating the chosen selection thresholds at the dashed lines shown. 123

7.4. Final signal cutflow for event picking selections. 124

7.5. Tail fraction percentages in the low-MET control. 131

7.6. dEdx shapes of different slices of p_T in the low-MET control. All slices are normalized to show relative differences. 132

7.7. Electron, muon, and hadron $\mathrm{d}E/\mathrm{d}x$ templates. 135

Figure Page

7.8. Extracted MIP $\mathrm{d}E/\mathrm{d}x$ template, $\mathrm{pdf}_{\mathrm{MIP}}$. 136

7.9. Extracted fake $\mathrm{d}E/\mathrm{d}x$ template, $\mathrm{pdf}_{\mathrm{fake}}$. 137

7.10. Expected exclusion limits for $\tilde{\tau}$ and $\tilde{\chi}_1^{\pm}$ models for lifetime of 1 ns. 138

LIST OF TABLES

Table Page

2.1. Summary of fermion masses and quantum numbers in the Standard Model. 23

4.1. Stave locations and pixel properties. 47

4.2. Pixel ring locations and sensor properties. 49

4.3. Table showing number of disconnected bump bonds after thermal cycling. 57

5.1. Summary of tracklet reconstruction requirements. 60

5.2. Summary of LRT reconstruction requirements. 62

5.3. Definitions of variables used in the Bethe-Bloch equation. 72

6.1. Summary of the signal region selection requirements. 91

6.2. Summary of the event and tracklet selection requirements for the CRs associated with the four-layer SRs. 101

6.3. Summary of the event and tracklet selection requirements for the CRs associated with the three-layer SRs that contain a low-energy charged pion. 102

6.4. Summary of the event and tracklet selection requirements for the CRs associated with the three-layer SRs that veto a low-energy charged pion. 103

6.5. Summary of the event and tracklet selection requirements for the validation regions. 103

6.6. Summary of the observed and post-fit expected SR yields, with 'Bkg.' denoting background, and the model-independent fit results. All systematic and statistical uncertainties are considered. The calculated p_0-value is capped at 0.5 and shown together with the corresponding significance in standard deviations (Z). 110

7.1. Event Picking Selections applied to run 2 and partial run 3 dataset. . . . 125

Table Page

7.2. The baseline tracklet selections used for all signal regions, applied in addition to baseline selections. 126

7.3. Signal region selections. Note these are in addition to the baseline selections defined in 7.4.2 126

7.4. Kinked Veto event selections. 127

7.5. Additional selections used for low-mass signal region selections. 127

7.6. Event selections for the kink-required SR, which targets large mass-splitting signals like the GMSB stau. A kinked tracklet is required as a unique probe for these signal events. Since significant background rejection is achieved from the kink and the $\mathrm{d}E/\mathrm{d}x$ requirement, the $E_{\mathrm{T}}^{\mathrm{miss}}$ and vertex-constrained p_{T} thresholds are loosened to 100 GeV and 40 GeV, respectively, to maximize signal acceptance. 128

7.7. Tracklet selections for the kink-required SR, which targets large mass-splitting signals like the GMSB stau. A kinked tracklet is required as a unique probe for these signal events. Since significant background rejection is achieved from the kink and the $\mathrm{d}E/\mathrm{d}x$ requirement, the $E_{\mathrm{T}}^{\mathrm{miss}}$ and vertex-constrained p_{T} thresholds are loosened to 100 GeV and 40 GeV, respectively, to maximize signal acceptance. 128

7.8. Inclusive Region background estimation. 133

7.9. Tracklet selections used to define the fake enriched region. 137

CHAPTER I

INTRODUCTION

The pursuit of understanding the fundamental building blocks of the Universe has long been a central goal of physics. Over the past century, significant progress has been made in describing the elementary particles, their interactions, and the underlying fields. Despite these achievements, several important open questions remain, including the nature of dark matter and the hierarchy problem associated with the Higgs boson. These open questions provide strong motivation for the continuing investigation into the fundamental structure of the Universe.

The ATLAS detector is designed to study these building blocks in an effort to address such questions. As a general purpose detector at the Large Hadron Collider (LHC), ATLAS records proton-proton collisions at center-of-mass energies of up to 13.6 TeV. The data collected from ATLAS is used to perform precision measurements of Standard Model and to search for evidence of physics beyond the Standard Model.

This dissertation presents work on both physics analyses and detector upgrade tasks. The two analyses presented in this dissertation search for signatures of disappearing tracks and the combination of the disappearing tracks with ionization energy loss. Both analyses target the direct detection of charged long-lived particles predicted in supersymmetric models. The analysis targeting a disappearing track signature found in chapter VI is previously published co-authored material by the ATLAS Collaboration [1]. The detector upgrade work focuses on the ATLAS Inner Tracker, contributing to preparations for the High-Luminosity LHC era and ensuring the continued performance of the ATLAS detector with higher pileup and integrated luminosity.

CHAPTER II

OVERVIEW AND MOTIVATION

2.1 Standard Model of Particle Physics

The Standard Model (SM) of particle physics represents one of the most significant achievements of modern theoretical and experimental physics. Developed through decades of theoretical innovation and experimental discovery, it provides a remarkably successful framework for describing the fundamental particles and their interactions. Extensive experimental tests have confirmed its predictions with high precision. The SM is a quantum gauge field theory that describes the known elementary particles and three of the four fundamental forces: electromagnetic, weak, and strong. This description is based on the local symmetries under the groups $\mathrm{SU}(3)_C \times \mathrm{SU}(2)_L \times \mathrm{U}(1)_Y$. Particles in this framework are understood as excitations of their corresponding quantum fields.

The SM elementary particles are shown in Fig. 2.1.

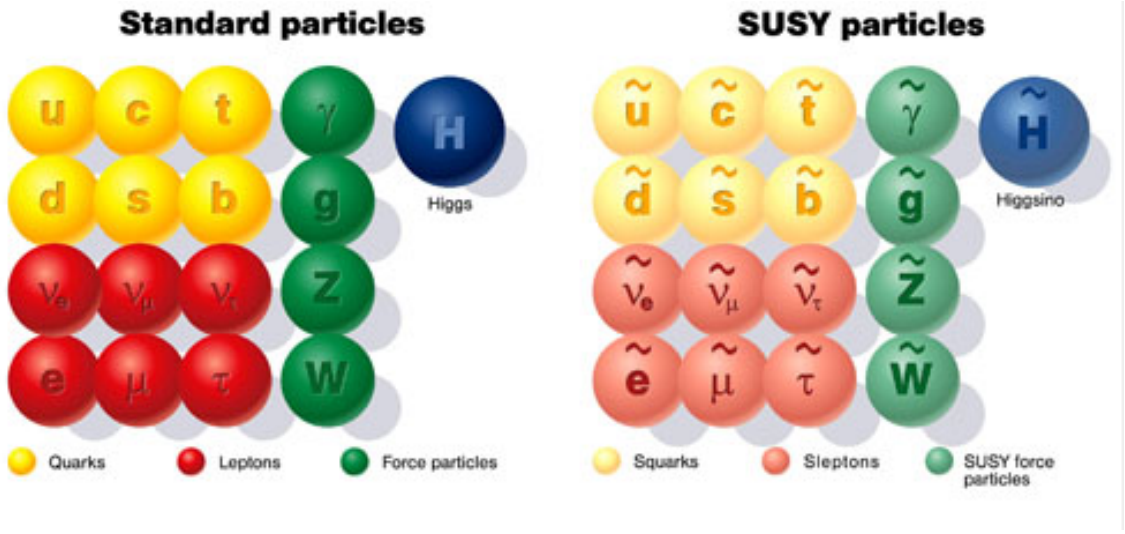


Figure 2.1. Standard model elementary particles on the left and their superpartners on the right. [2].

2.1.1 Fermions. Particles can be classified in several ways, one of the simplest being by their spin. Particles with half-integer spin are known as fermions.

All elementary fermions in the Standard Model have spin-1/2 and constitute all the observable matter in the universe. Fermions are divided into two classes: leptons and quarks, each organized into three generations. Each generation has identical electric and strong charge but differs in mass.

Each generation of leptons consists of a charged lepton and a neutrino. Neutrinos carry no electric charge and do not interact via the electromagnetic force. Neutrinos also do not carry color charge, and therefore interact only via the weak force. This makes them among the most difficult particles to detect experimentally. Charged leptons carry one unit of electric charge and interact via both the electromagnetic and weak interactions.

Quarks carry both electric and color charge and therefore participate in all three interactions. They are divided into up-type and down-type quarks. Due to color confinement, quarks are not observed as free particles, but only as bound states in color-neutral hadrons.

Color charge is the quantum number associated with the strong interaction, described by the gauge group $\mathrm{SU}(3)_C$. Quarks can exist in any one of three colored states, often represented as r, g, b for red, green, and blue (Not to be confused with photon colors in the visible spectrum. It is just a convenient analogy to help keep track of the charges).

A summary of the quantum numbers of fermions is given in Table 2.1.

2.1.2 Bosons. Bosons are particles with integer spin and include the force carriers of the Standard Model. The gauge bosons are spin-1 vector particles that arise from the underlying gauge symmetries and mediate the fundamental interactions. These consist of the photon, which mediates the electromagnetic interaction; eight gluons, which mediate the strong interaction between colored particles; and the $W^{\pm}$ and Z^0 bosons, which mediate the weak interaction.

Table 2.1. Summary of fermion masses and quantum numbers in the Standard Model.

Fermion	Symbol Used	Mass	Electric Charge	Color Charge
Electron	e	0.5110 MeV	-1	0
Muon	μ	105.7 MeV	-1	0
Tau	τ	1776 MeV	-1	0
Electron Neutrino	ν_e	< 0.8 eV	0	0
Muon Neutrino	ν_μ	< 0.8 eV	0	0
Tau Neutrino	ν_τ	< 0.8 eV	0	0
Up Quark	u	2.16 MeV	2/3	Yes
Down Quark	d	4.70 MeV	-1/3	Yes
Charm Quark	c	1.27 GeV	2/3	Yes
Strange Quark	s	93.5 MeV	-1/3	Yes
Top Quark	t	182.6 GeV	2/3	Yes
Bottom Quark	b	4.18 GeV	-1/3	Yes

In addition to the gauge bosons, the Standard Model contains a scalar, spin-0, particle known as the Higgs boson. The Higgs field is introduced as an electroweak symmetry breaking mechanism. Through the Higgs mechanism, the electroweak symmetry $\mathrm{SU}(2)_L \times \mathrm{U}(1)_Y$ is spontaneously broken to $\mathrm{U}(1)_{\mathrm{em}}$. This symmetry breaking gives rise to masses for the $W^\pm$ and Z^0 bosons, while the photon remains massless, and also allows fermions to acquire mass through Yukawa couplings to the Higgs field.

2.2 Motivation For Physics Beyond the Standard Model

Despite the remarkable success of the Standard Model, there remain several open questions in particle physics. Notably, the Standard Model does not provide an explanation for dark matter, nor does it address the hierarchy problem. These issues do not indicate that the Standard Model is incorrect, but rather suggest that it is an incomplete description of particle physics.

The hierarchy problem arises from the sensitivity of the Higgs boson parameters to quantum corrections. Consider the Higgs potential

$$V(\Phi) = m_H^2|\Phi|^2 + \lambda|\Phi|^4, \tag{2.1}$$

where Φ is the complex scalar Higgs doublet, m_H^2 is the negative mass squared parameter, and λ is the Higgs self coupling parameter. Radiative corrections from loop diagrams involving Standard Model particles modify the Higgs mass parameter according to

$$m_H^2 = m_{H,\text{bare}}^2 + \Delta m_H^2.$$

For example, a fermion loop, as illustrated in Fig. 2.3, gives a correction of the form

$$\Delta m_H^2 \sim -\frac{|\lambda_f|^2}{8\pi^2}\Lambda_{\text{UV}}^2 + ... \tag{2.2}$$

λ_f is the Yukawa coupling and Λ_{UV} is the ultraviolet cutoff scale.

These corrections grow quadratically with the cutoff scale, implying that if the Standard Model is valid up to very high energies, the Higgs mass receives large quantum corrections. Maintaining the Higgs mass at the electroweak scale therefore requires a delicate cancellation between the bare mass parameter and these radiative corrections. This apparent fine-tuning is generally regarded as unnatural and provides strong motivation for physics beyond the Standard Model [3].



Figure 2.2. 1 loop Higgs quantum corrections example from a) fermions and b) SUSY scalars

In addition to the hierarchy problem, another open problem in particle physics is the existence of dark matter. Astrophysical and cosmological observations provide strong evidence for the existence of large amounts of non-luminous matter, known as dark matter, in the universe. One of the earliest pieces of evidence comes from measurements of galactic rotation curves, which show that star's rotational velocities in galaxies at large radii remain approximately constant, as seen in Fig. 2.3. In contrast, if visible matter

accounted for the majority of the galactic mass, the rotational velocity of stars would be expected to decrease with increasing distance from the galactic center. Additional evidence for dark matter arises from observations such as gravitational lensing and the dynamics of galaxy clusters, both of which indicate the presence of additional mass contributing to the gravitational potential.

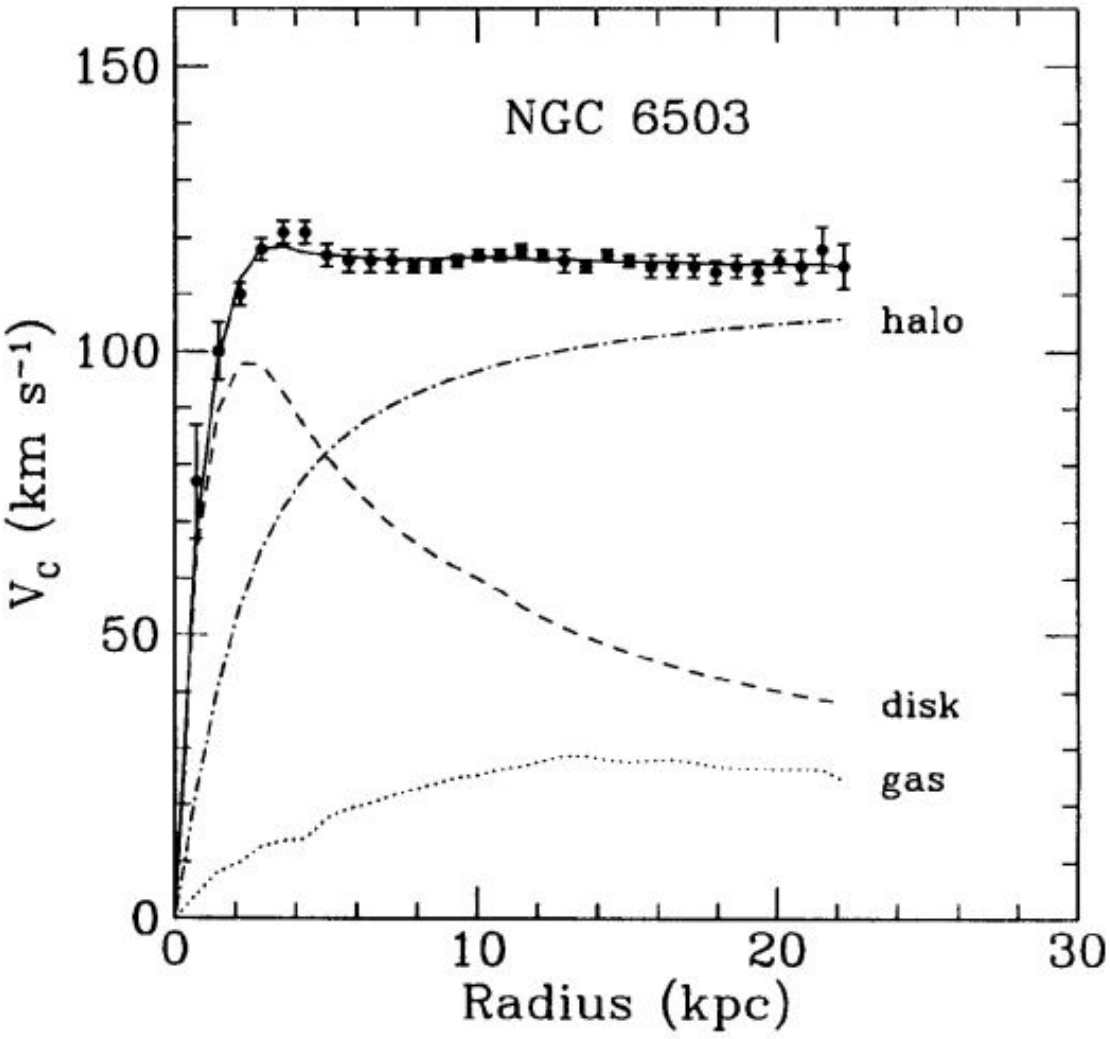


Figure 2.3. Rotation curves for NGC 6503, Note the circle marks with error bars are the measured data. [4]

Except for gravitational wave observations from detectors such as LIGO, Virgo, and KAGRA, most astronomical measurements rely on the detection of photons. Since no

direct detection of dark matter has yet been achieved, it is inferred that dark matter does not interact electromagnetically, and its presence is instead deduced indirectly through its gravitational effects on visible matter and radiation.

These observations imply that a significant fraction of the matter content of the universe is not directly observable, with current estimates indicating that approximately 84.4% of the total matter density is dark matter, compared to about 15.6% baryonic (visible) matter [5].

Both the hierarchy problem and the existence of dark matter point toward physics beyond the Standard Model. These observations motivate the development of new theoretical frameworks and continued experimental searches for undiscovered particles. While the specific theory that extends the Standard Model remains unknown, several well-motivated candidates have been proposed of which supersymmetry is one of the most extensively studied.

2.3 Supersymmetry

Supersymmetry (SUSY) is a theoretical extension of the Standard Model that introduces a spacetime symmetry relating fermions and bosons. This symmetry predicts the existence of a rich new set of particles, known as superpartners, which extend the Standard Model particle content. Supersymmetry provides a compelling framework to address the hierarchy problem and also offers viable candidates for dark matter.

The defining feature of supersymmetry is the existence of supersymmetric transformations, Q, that transform bosonic states into fermionic states and vice versa:

$$Q\,|\text{boson}\rangle = |\text{fermion}\rangle\,, \tag{2.3}$$

$$Q\,|\text{fermion}\rangle = |\text{boson}\rangle\,. \tag{2.4}$$

Particles in supersymmetric theories are organized into supermultiplets, in which each bosonic degree of freedom is paired with a fermionic degree of freedom. For example, each Weyl fermion is associated with two real scalar superpartners, typically arranged

into a complex scalar field [6]. Similarly, spin-1 gauge bosons are paired with spin-1/2 fermionic superpartners known as gauginos. These superpartners extend the Standard Model particle content, leading to a rich phenomenology and providing new particles to search for experimentally.

The full set of predicted superpartners is illustrated in Fig. 2.1. The scalar superpartners of the Standard Model leptons and quarks are collectively referred to as sleptons and squarks, respectively. Their names are formed by prefixing the corresponding Standard Model particle name with "s", for example the scalar partner of the tau lepton is the stau. Similarly, the fermionic superpartners of the Standard Model gauge bosons are known as gauginos. Their names are conventionally formed by appending the suffix "ino" to the corresponding gauge boson name.

Supersymmetric particles are conventionally denoted using the same symbol as their Standard Model partners with a tilde placed above the symbol to distinguish them. Following electroweak symmetry breaking, the charged and neutral gauginos mix with the higgsinos; the gauge eigenstates are not identical to the mass eigenstates. The resulting charged mass eigenstates are known as charginos and the neutral mass eigenstates as neutralinos, denoted by $\tilde{\chi}^{\pm}$ and $\tilde{\chi}^{0}$, respectively.

The scalar superpartners of fermions introduce additional contributions to the Higgs mass through loop corrections, as illustrated in Fig. 2.3(b). These scalar loop contributions enter with an opposite sign relative to the fermion loops due to their differing spin statistics.

For a fermion and its corresponding scalar super partner, the combined correction to the Higgs mass parameter can be written schematically as

$$\Delta m_H^2 \sim \frac{\lambda_S}{16\pi^2}\left[\Lambda_{\mathrm{UV}}^2 - 2m_S^2 \ln\left(\frac{\Lambda_{\mathrm{UV}}}{m_S}\right)\right] - \frac{|\lambda_f|^2}{8\pi^2}\Lambda_{\mathrm{UV}}^2, \tag{2.5}$$

where λ_f is the fermion Yukawa coupling, λ_S is the scalar coupling, and m_S is the scalar mass.

In the limit of exact supersymmetry, where $\lambda_S = |\lambda_f|^2$ and the fermion and scalar masses are degenerate, the quadratic divergences cancel exactly. This cancellation stabilizes the Higgs mass against large radiative corrections and provides a natural solution to the hierarchy problem. In realistic models where supersymmetry is broken, this cancellation is only approximate, leaving behind only a log divergence. Despite SUSY being broken it still significantly reduces the degree of fine-tuning required in the Higgs field.

Supersymmetry must be a broken symmetry. The mechanism of SUSY breaking leads to a variety of possible phenomenological scenarios. The searches in this dissertation consider three different scenarios for SUSY, constrained minimal supersymmetric standard model, gauge-mediated supersymmetry breaking, and anomaly mediated supersymmetry breaking. The scenarios relevant to this dissertation are theoretically motivated and involve long-lived charged particles that decay into Standard Model states. In all cases discussed, some or all of the decay products escape detection, resulting in missing energy signatures. Although these are not the only mechanisms that can produce long-lived charged particles in beyond the Standard Model scenarios, these scenarios provide a well-motivated and experimentally accessible region of parameter space. This makes them a natural and systematic target for the searches presented in this dissertation.

2.3.1 Constrained Minimal Supersymmetric Standard Model.

One compelling SUSY model that provides a dark matter candidate is the constrained minimal supersymmetric standard model (CMSSM). In this model, the neutralino ($\tilde{\chi}_1^0$) can be the lightest SUSY particle and is a natural long-lived stable particle that provides a dark matter candidate, while the next to lightest SUSY particle (NLSP) is the charged stau ($\tilde{\tau}$).

A naive calculation of the relic abundance of $\tilde{\chi}_1^0$ typically predicts an overproduction of dark matter compared to current cosmological observations. A

mechanism that can significantly reduce this relic density is $\tilde{\tau}$–$\tilde{\chi}_1^0$ coannihilation [7]. If the $\tilde{\tau}$ and $\tilde{\chi}_1^0$ are nearly mass-degenerate, they remain in thermal equilibrium for a longer period during freeze-out in the early universe. During this process, coannihilation channels involving $\tilde{\tau}$ increase the effective annihilation cross-section, thereby reducing the relic abundance of $\tilde{\chi}_1^0$. This mechanism can bring the predicted relic density into agreement with current observational constraints.

The mass splitting $\Delta m = m_{\tilde{\tau}} - m_{\tilde{\chi}^0}$ provides key insights into the decay width and phenomenology of the $\tilde{\tau}$. As Δm decreases, the available phase space becomes increasingly suppressed, leading to a smaller decay width and consequently a longer lifetime.

If the mass splitting between the $\tilde{\tau}$ and the neutralino exceeds the tau mass, $\Delta m(\tilde{\tau}, \tilde{\chi}_1^0) = m_{\tilde{\tau}} - m_{\tilde{\chi}_1^0} > m_\tau$, then the decay width of the $\tilde{\tau}$ is dominated by the two-body decay $\tilde{\tau} \to \tilde{\chi}_1^0 \tau$.

The decay width for this process is approximately [8]

$$\begin{aligned}\Gamma(\tilde{\tau} \to \tau\tilde{\chi}_1^0) =& \frac{1}{16\pi m_{\tilde{\tau}}^3}(m_{\tilde{\tau}}^4 + m_{\tilde{\chi}_1^0}^4 + m_\tau^4 - 2m_{\tilde{\tau}}^2 m_{\tilde{\chi}_1^0}^2 - 2m_{\tilde{\tau}}^2 m_\tau^2 - 2m_\tau^2 m_{\tilde{\chi}_1^0}^2)^{\frac{1}{2}} \\ & \times \left[\left(|c_L|^2 + |c_R|^2 \right) \left((\Delta m)^2 + 2(\Delta m) m_{\tilde{\chi}_1^0} - m_\tau^2 - 2\left(c_L c_R^* + c_L^* c_R \right) m_{\tilde{\chi}_1^0} m_{\tilde{\tau}} \right) \right]\end{aligned} \tag{2.6}$$

Here, c_L and c_R are the left- and right-handed couplings to the τ, respectively. These depend on the electroweak parameters, including the hypercharge and weak coupling constants, the weak mixing angle, as well as the $\tilde{\tau}$ and $\tilde{\chi}_1^0$ mixing angles.

In the region where $\Delta m \approx m_\tau$ the width is significantly reduced and the $\tilde{\tau}$ is long-lived, with a typical lifetime of $\mathcal{O}(1\text{ ns})$, which is relevant for the phenomenology considered in this dissertation.

As the mass splitting, Δm, decreases further, the two-body decay channel $\tilde{\tau} \to \tilde{\chi}_1^0 \tau$ becomes kinematically inaccessible once $\Delta m < m_\tau$. In this regime, the $\tilde{\tau}$ instead decays via suppressed three- and four-body processes.

The dominant decay modes include

$$\tilde{\tau} \to \tilde{\chi}_1^0 \, \nu_\tau \, a_1, \tag{2.7}$$

$$\tilde{\tau} \to \tilde{\chi}_1^0 \, \nu_\tau \, \rho, \tag{2.8}$$

$$\tilde{\tau} \to \tilde{\chi}_1^0 \, \nu_\tau \, \pi, \tag{2.9}$$

$$\tilde{\tau} \to \tilde{\chi}_1^0 \, \nu_\tau \, \bar{\nu}_e \, e, \tag{2.10}$$

$$\tilde{\tau} \to \tilde{\chi}_1^0 \, \nu_\tau \, \bar{\nu}_\mu \, \mu, \tag{2.11}$$

where the available decay channels depend on the value of the mass splitting Δm and the corresponding kinematically accessible phase space.

This behavior is phenomenologically important, as in all of these scenarios the $\tilde{\tau}$ can appear as a long-lived charged particle before decaying into relatively soft Standard Model final states. These decay products carry low momentum, making them challenging to detect experimentally. In addition, the $\tilde{\chi}^0$, being weakly interacting, escapes the detector without depositing energy, resulting in missing transverse momentum in the final state.

2.3.2 Gauge Meditated SUSY Breaking. Another scenario of interest for this dissertation is gauge-mediated supersymmetry breaking (GMSB).

In GMSB models, the supersymmetry breaking is thought to take place in some hidden sector and communicated to the visible sector via the Standard Model gauge interactions. This is achieved through messenger fields, which couple to the hidden sector responsible for supersymmetry breaking and transmit this breaking to the quarks, leptons, and Higgs fields, as well as their supersymmetric partners.

In the parameter space relevant for this analysis, the lightest supersymmetric particle (LSP) is the gravitino ($\tilde{G}$), which is typically very light, and the next-to-lightest supersymmetric particle (NLSP) is the stau ($\tilde{\tau}$).

In these models, the dominant decay mode is $\tilde{\tau} \to \tilde{G} \, \tau$. This signature is experimentally easier to detect than in models such as the CMSSM, as the τ can carry

a significant amount of momentum and is therefore more readily reconstructed. As a result, GMSB scenarios are often used as benchmark models in searches for long-lived supersymmetric particles.

In this framework, the $\tilde{\tau}$ decay width is given by [9]

$$\Gamma(\tilde{\tau} \to \tau \tilde{G}) \simeq \frac{1}{48\pi} \frac{m_{\tilde{\tau}}^5}{m_{3/2}^2 M_*^2}\,, \tag{2.12}$$

where $m_{3/2}$ is the gravitino mass and M_* is the reduced Planck scale.

This expression highlights an important feature of GMSB phenomenology. In contrast to models such as the CMSSM, the $\tilde{\tau}$ lifetime in GMSB is primarily controlled by the weak coupling between the $\tilde{\tau}$, τ, and $\tilde{G}$, which is governed by the small gravitino mass. In particular, for small $m_{3/2}$, this suppression results in a long-lived $\tilde{\tau}$.

2.3.3 Anomaly Mediated SUSY Breaking. The final scenario of interest to this dissertation is Anomaly Mediated Supersymmetry Breaking (AMSB). In this scenario, supersymmetry is assumed to be broken in some hidden sector, similarly to GMSB. In AMSB the breaking is communicated to the visible sector through superconformal anomalies in supergravity.

A distinctive feature of AMSB is the near mass degeneracy between the charged and neutral winos. The mass splitting arises predominantly from electroweak loop corrections. These corrections lead to a mass difference of approximately $\Delta m_{\tilde{\chi}^0, \tilde{\chi}_1^\pm} \approx 165\,\text{MeV}$ [10].

This small mass splitting allows for the decay channel $\tilde{\chi}_1^\pm \to \tilde{\chi}^0 \pi^\pm$. The corresponding decay width is given by [11]

$$\Gamma(\tilde{\chi}_1^\pm \to \pi^\pm \tilde{\chi}_1^0) = \frac{1}{2\pi} F_\pi^2 \left(\frac{g^2}{M_W^2 V_{ud}}\right)^2 \Delta m^3 \left(1 - \frac{m_\pi^2}{\Delta m^2}\right)^{1/2} \left(1 - \frac{\Delta m}{m_{\tilde{\chi}_1^0}} + \frac{\Delta m^2 - m_\pi^2}{4 m_{\tilde{\chi}_1^0}}\right)\,. \tag{2.13}$$

Here, F_π is the pion decay constant, g is the weak coupling constant, M_W is the W boson mass, and V_{ud} is the relevant element of the CKM matrix coupling the W-boson to the quarks in the pion.

This scenario is analogous to the compressed spectra cases discussed previously, in which a small mass splitting leads to a suppressed decay width and consequently a long-lived charged particle. The small value of $\Delta m_{\chi^\pm,\chi^0}$ results in a soft pion in the final state, which can be difficult to reconstruct experimentally.

CHAPTER III

EXPERIMENTAL SETUP

This chapter describes the experimental setup used to collect the data for the long-lived particle searches presented in Sections VI and VII. All results presented in this dissertation are based on data collected by the ATLAS detector at the Large Hadron Collider (LHC) at CERN.

3.1 The Large Hadron Collider

The LHC is currently the world's largest and highest-energy particle accelerator, with a total circumference of approximately 27 km. It is located about 100 m underground, straddling the border between Switzerland and France near Geneva. The LHC accelerates protons to nearly the speed of light using radio-frequency (RF) cavities and superconducting magnets, and brings counter-rotating proton beams into collision at four interaction points evenly spaced around the accelerator ring. At each interaction point resides one of the four main experiments: ATLAS, CMS, LHCb, and ALICE. The center-of-mass energy of proton–proton collisions was 13 TeV during Run 2 and 13.6 TeV during Run 3.

Protons are produced from hydrogen gas and accelerated through a sequence of injector machines prior to entering the LHC. Since hydrogen is initially in molecular form, electrons are first added to form H^- ions. These ions are then passed through a stripping foil, removing the electrons and producing protons (H^+). The protons are initially accelerated by RF cavities and focused using quadrupole magnets in the Linear Accelerator 4 (LINAC4), reaching an energy of 160 MeV.

Subsequently, the proton beam is injected into the Proton Synchrotron Booster (PSB), where it is further accelerated to 2 GeV. From there, the beam is transferred through the Proton Synchrotron (PS) and the Super Proton Synchrotron (SPS), where it undergoes additional acceleration and bunch shaping before final injection into the LHC. A detailed description of the injector chain performance can be found in Ref. [13].

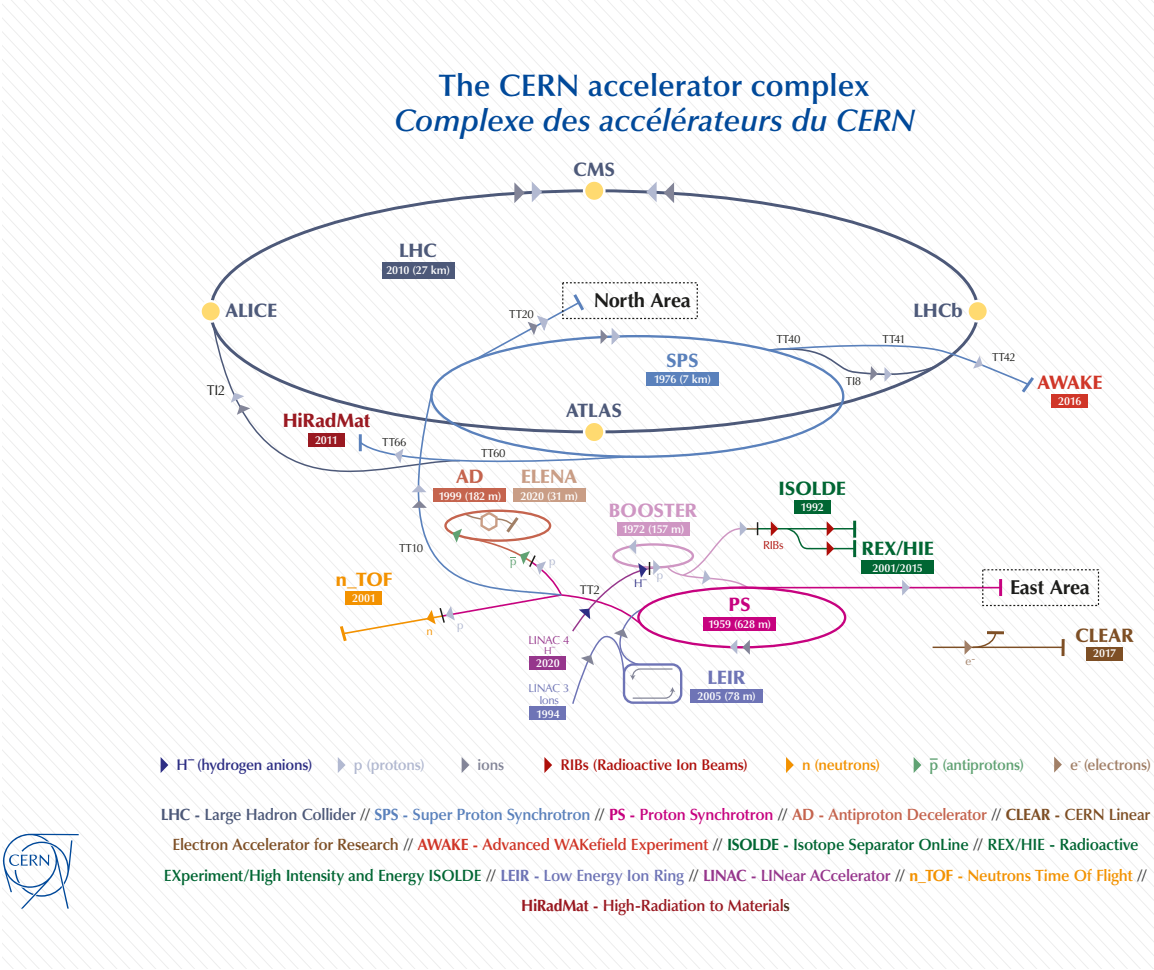


Figure 3.1. Schematic of the LHC accelerator complex [12], showing the sequence of accelerators used to prepare and inject proton beams into the LHC ring. Image credit:CERN.

Finally, the prepared proton bunches are injected into the LHC, where they are accelerated to their final energies and brought into collision at the four interaction points. A schematic view of the LHC injection chain and other experiments done at the LHC can be seen in Fig. 3.1

3.2 The ATLAS Detector

The ATLAS detector is a general purpose particle detector located at one of the four interaction points of the LHC. It is approximately 46 m long, 25 m in diameter, weighs about 7000 tons, and consists of multiple subsystems arranged concentrically around the interaction point. A CAD view of a cross-section of the ATLAS detector can be seen in Fig. 3.2.

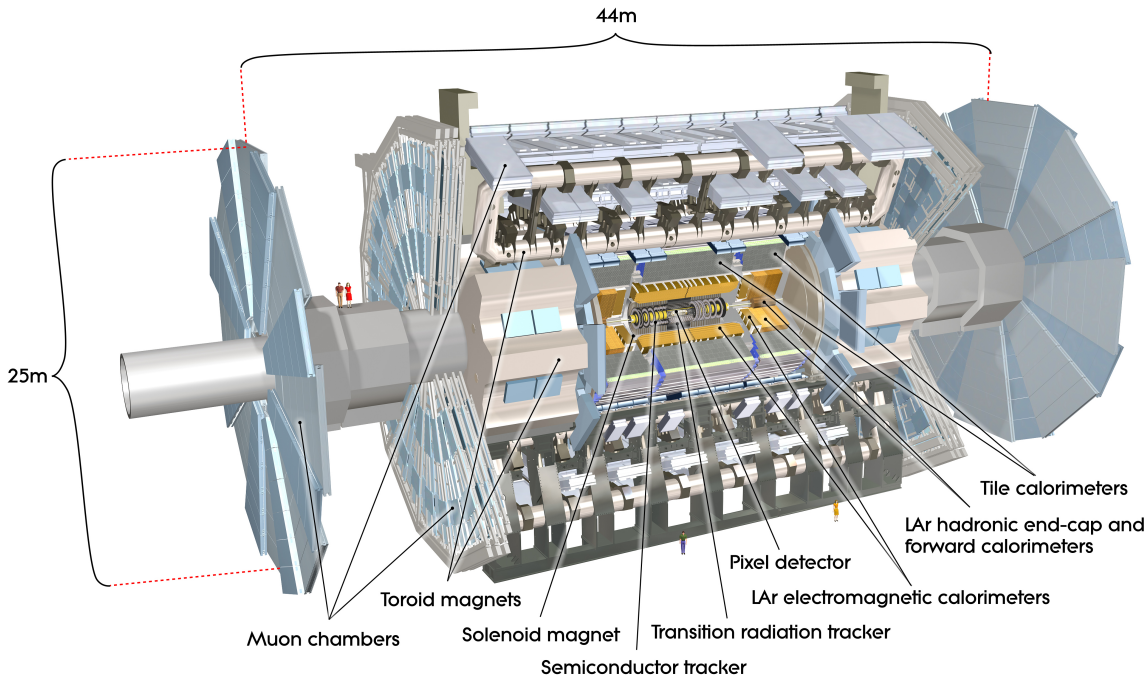


Figure 3.2. Schematic view of the ATLAS detector [14], showing the main subsystems arranged around the interaction point. Image credit: CERN

Starting from the interaction point and moving radially outward, the main subsystems are the Inner Detector (ID), the central solenoid magnet, the electromagnetic

and hadronic calorimeters, the toroidal magnet system, and the Muon Spectrometer (MS). Each subsystem is designed to measure specific properties of particles produced in proton–proton collisions.

The Inner Detector is the closest subsystem to the interaction point and is responsible for reconstructing the trajectories of charged particles. It provides precise measurements of track positions and momenta within a 2 T magnetic field generated by the central solenoid, which surrounds the ID. Outside the solenoid lies the electromagnetic calorimeter, which measures the energies of electrons and photons through the development of electromagnetic showers. Surrounding this is the hadronic calorimeter, designed to measure the energies of hadrons via hadronic showering, working in conjunction with the electromagnetic calorimeter to provide a complete measurement of the event energy flow.

Enclosing the calorimeters is the toroidal magnet system, which supplies the magnetic field required for the MS. The MS forms the outermost layer of ATLAS and is optimized for the detection and momentum measurement of muons. Due to their relatively large mass, long lifetime, and weak interactions with matter, muons typically traverse the ID and calorimeters with minimal energy loss, making the MS essential for their identification. The MS employs a combination of tracking chambers and magnetic fields to measure the curvature of muon trajectories, enabling precise momentum determination.

The ATLAS detector uses a right-handed coordinate system. The origin is at the nominal interaction point with the Z axis along the beam pipe. The Y axis points upwards and the X axis points to the center of the LHC ring. In ATLAS the normal angles θ and ϕ are used where θ is the polar angle measured from the positive z axis and ϕ is the azimuthal angle measured in the x-y plane from the x-axis. One important variable used in ATLAS is pseudorapidity, η, which is defined as $\eta = -\ln(\tan(\theta/2))$ where θ is the polar angle measured from the positive z axis. Pseudorapidity is useful

for ATLAS as the difference in pseudorapidity between particles, $\Delta\eta$, is invariant under Lorentz boosts along the beam axis with the assumption that the momentum of a particle is much larger than mass of the particle, $pc \gg mc^2$.

3.2.1 Inner Detector. The inner detector (ID) is a marvel of technology and innovation that was used in collaboration with other detector systems on ATLAS to not only discover a new particle but to confirm that it is a scalar Higgs Boson. The ID is at the center of the ATLAS detector and measures momentum, position, impact parameter, charge, and some particle identification including via ionization loss, of charged particles that pass though it. The ID consists of three main components: the Pixel Detector, the Semiconductor Tracker (SCT), and the Transition Radiation Tracker (TRT). The layout and radial sizes of the ID can be seen in Fig. 3.3

Particles that transverse the Pixel Detector, the SCT, and the TRT have momentum resolution which can be parameterized as

$$\frac{\sigma_{p_{\mathrm{T}}}}{p_{\mathrm{T}}} = 0.05\% \times p_{\mathrm{T}}\ [\mathrm{GeV}] \oplus 1\%. \tag{3.1}$$

3.2.1.1 Pixel Detector. The Pixel Detector is located closest to the interaction point and is composed of multiple layers of silicon pixel sensors, providing charged-particle tracking over radial distances from 33.5 mm to 122.5 mm. It consists of the Insertable B-Layer (IBL), three barrel layers, and three end-cap disks on each side of the detector. This configuration provides up to four space-point measurements for charged particles within a pseudorapidity coverage of $|\eta| < 2.5$.

The innermost pixel layer, known as the Insertable B-Layer (IBL), was installed during the first long shutdown of the LHC to enhance tracking and vertexing performance. The IBL is positioned at a radius of 33.5 mm from the beamline, enabling high-precision measurements close to the interaction point. It is constructed from 14 staves, each containing 32 front-end chips mounted on silicon sensors.

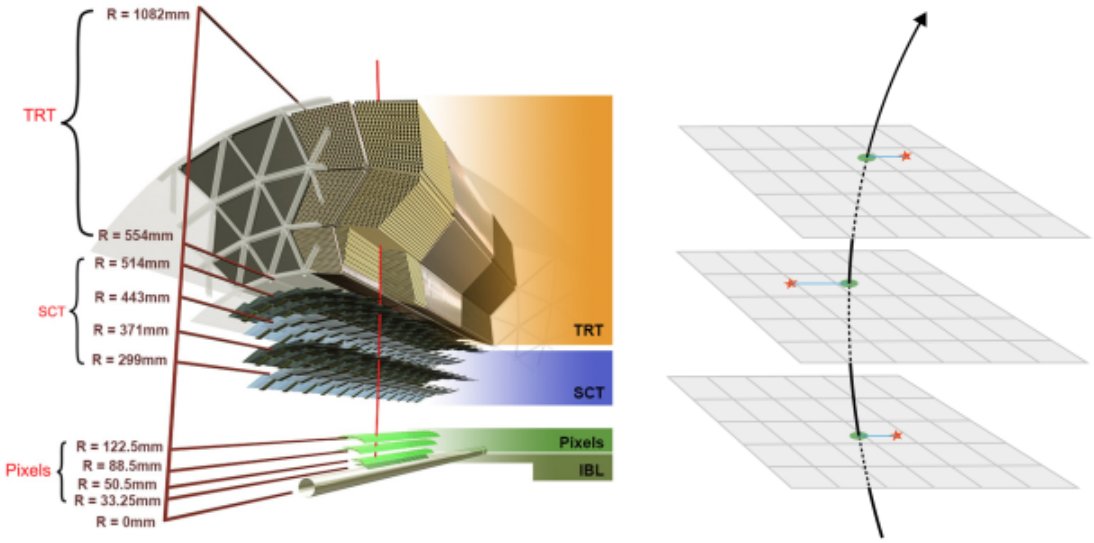


Figure 3.3. Left: Schematic view of the ID, showing the beam pipe, pixel barrel, SCT barrel, and TRT. Right: schematic view of charged particle track; red stars are cluster hits, the track is in black, green indicates the intersection of the track with the silicon layer, and blue represents the distance between the track and cluster hit on the surface of the silicon. Image credit: CERN [14].

Two sensor technologies are employed in the IBL: planar sensors and 3D sensors. Planar sensors are used in the central region of each stave, while 3D sensors are utilized in the forward regions due to their superior radiation tolerance. The superior radiation tolerance of 3D sensors vs planar sensors comes from a reduction in the electrode separation which reduces the probability of charge trapping. Each sensor is segmented into pixels with dimensions of 50 μm in ϕ and 250 μm in z. Each stave contains 80 columns and 336 rows of pixels, resulting in approximately 12 million pixels in the full IBL.

The remaining three barrel layers of the Pixel Detector, referred to as the B-layer, Layer 1, and Layer 2, are located at radii of 50.5 mm, 88.5 mm, and 122.5 mm, respectively. In these layers, planar silicon sensors with a thickness of 250 μm are used, with pixel dimensions of 50 μm in ϕ and 300 μm in z.

The pixel detector is capped by 3 end-caps on either side of the collision point at z distances of 495 mm, 580 mm, 650 mm.

A pixel module consists of a silicon sensor bump-bonded to dedicated readout chips. The sensors are based on reverse-biased silicon diodes. Applying a reverse bias voltage creates a depleted region within the sensor volume. Charged particles traversing this depletion region generate approximately 90 electron-hole pairs per micrometer, with each pair requiring about 3.6 eV to be produced [15]. The resulting charge carriers drift under the applied electric field, inducing a measurable signal on the electrodes.

Direct measurement of the collected charge would require power-intensive analog-to-digital conversion. Instead, the pixel readout employs a digital scheme in which the induced signal is first amplified and shaped, and then compared to a predefined threshold. The duration for which the signal remains above this threshold, referred to as the Time-over-Threshold (ToT), is a function of the deposited charge. Due to the non-linear response of the electronics, careful calibration is performed. The first step of calibration is threshold tuning. A threshold scan is performed to measure the hits per injection as a function of injected charge. The threshold is then tuned to ensure that the signal-to-noise ratio is greater than 50 [16]. After the threshold tuning a ToT scan can be done by injecting known charges and measuring the corresponding ToT response, meaning that for a given pixel there is a map between the ToT and charge deposited in a given pixel.

3.2.1.2 Semiconductor Tracker.

The Semiconductor Tracker (SCT) is located outside the Pixel Detector and provides precision tracking at radial distances between approximately 299 mm and 560 mm from the beamline, covering a pseudorapidity range of $|\eta| < 2.5$. The SCT is a silicon microstrip detector designed to complement the Pixel Detector by extending the tracking lever arm and improving momentum resolution, see Fig. 3.4 for schematic view of silicon sensors.

The SCT consists of 4088 silicon strip modules arranged in four barrel layers and two end-caps, each comprising nine disks. Each module contains two back-to-back silicon strip sensors mounted with a small stereo angle, enabling three-dimensional space-point reconstruction.

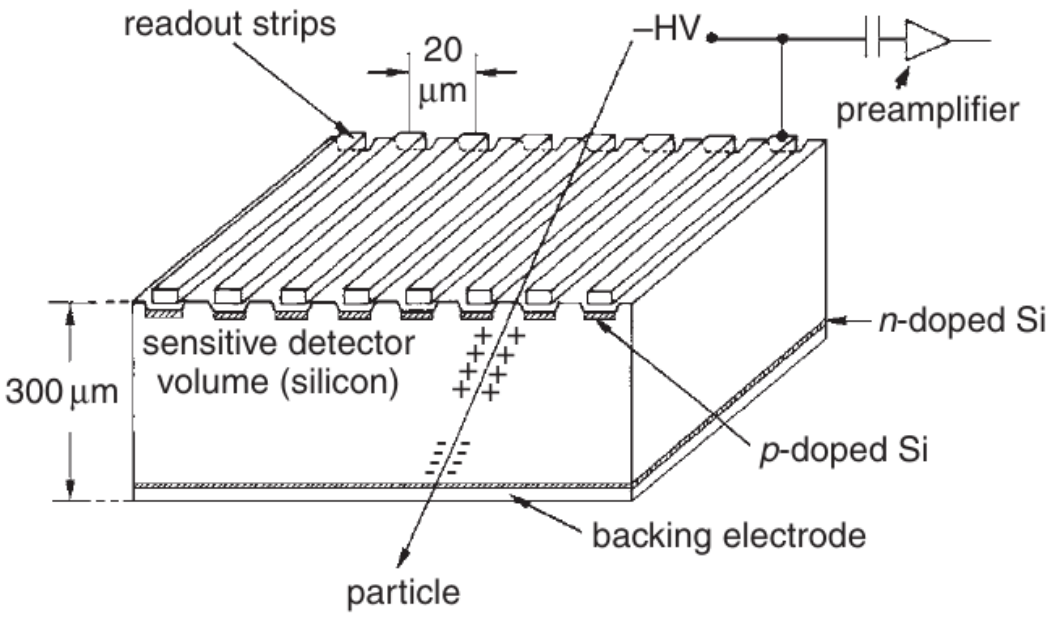


Figure 3.4. Schematic view of silicon microstrip detector. Credit: [17]

3.2.1.3 Transition Radiation Tracker. The Transition Radiation Tracker (TRT) forms the outermost component of the ID. It is composed of straw tubes filled with a xenon-based gas mixture, which serve both as tracking detectors and as transition radiation detectors for electron identification.

As charged particles traverse the straw tubes, they ionize the gas, and the resulting electrons drift toward the central anode wires where the signals are read out. Each straw has a diameter of 4 mm, allowing the TRT to provide up to approximately

36 measurements per track, significantly increasing the number of tracking points in the outer region of the ID.

A limitation of the TRT is that it provides position measurements only in the R–ϕ plane. Nevertheless, when combined with the Pixel Detector and SCT, the TRT enhances pattern recognition and improves track momentum resolution by providing tracking over a larger radial distance.

3.2.2 Calorimeters. ATLAS employs two main calorimeter systems: the electromagnetic calorimeter and the hadronic calorimeter, as seen in Fig. 3.5. Together, these systems are designed to absorb and measure the energies of particles emerging from the interaction point after they traverse the ID.

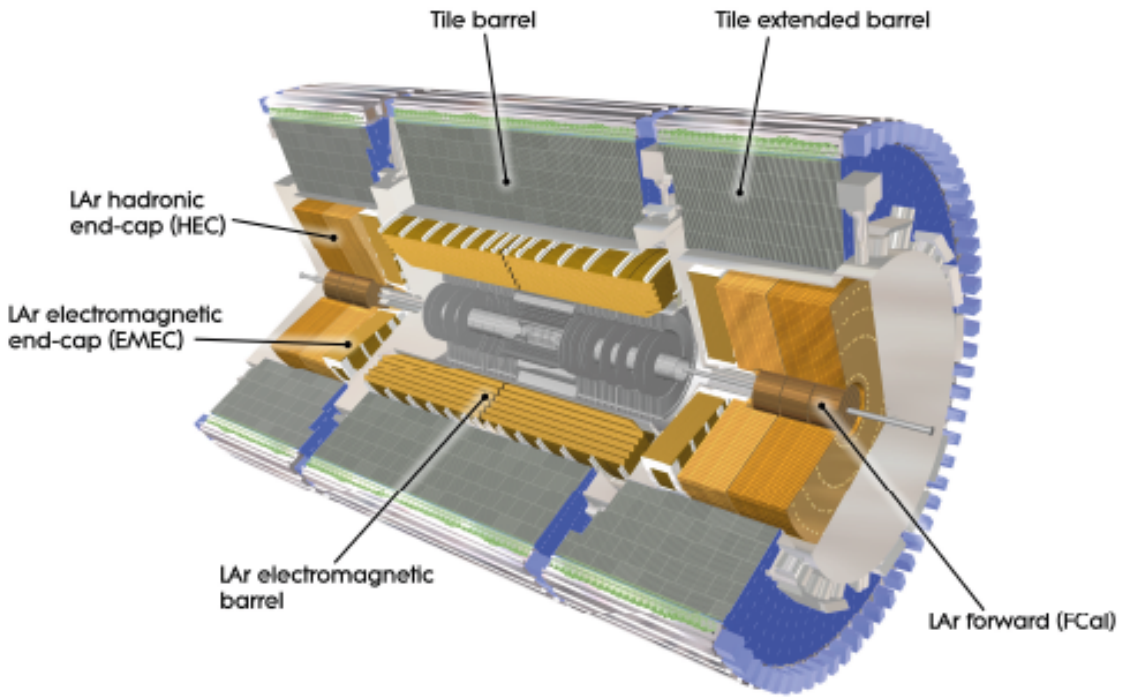


Figure 3.5. Schematic view of the Calorimeters[14], showing the electromagnetic and hadronic calorimeters. Image credit: CERN.

3.2.2.1 Electromagnetic Calorimeter. The electromagnetic calorimeter is a sampling calorimeter that uses lead as the absorber material and liquid argon as the active medium. Incident electrons and photons initiate electromagnetic

showers in the lead absorbers, with the resulting ionization signals collected in the liquid argon layers to provide precise energy measurements.

The electromagnetic calorimeter is divided into a barrel section and two end-cap sections. The barrel region covers a pseudorapidity range of $|\eta| < 1.475$, while the end-cap regions extend the coverage to $1.375 < |\eta| < 3.2$.

3.2.2.2 Hadronic Calorimeter. The hadronic calorimeter is also a sampling calorimeter, employing steel and copper as absorber materials and scintillating tiles and liquid argon as active media. It is designed to measure the energies of hadrons through the development of hadronic showers.

Similar to the electromagnetic calorimeter, the hadronic calorimeter is divided into a barrel section and two end-cap sections. The barrel region covers $|\eta| < 1.4$, while the end-cap regions extend the coverage to $1.4 < |\eta| < 4.8$. In the forward and end-cap regions, liquid argon technology is used to accommodate the higher radiation levels.

3.2.3 Muon Spectrometer. Due to their relatively large mass and weak interactions with matter, muons typically traverse the ID and calorimeters while depositing only small amounts of ionization energy. As a result, the outermost subsystem of ATLAS is dedicated to reconstructing the momentum and trajectory of these weakly interacting charged particles.

The MS is constructed using five detector technologies: Thin Gap Chambers (TGCs), Resistive Plate Chambers (RPCs), Monitored Drift Tubes (MDTs), Small-Strip Thin Gap Chambers (sTGCs), and Micromegas. The majority of the precision tracking measurements are provided by the Monitored Drift Tubes.

The MS consists of a barrel region and two end-cap regions. The barrel region covers the pseudorapidity range $|\eta| < 1.2$, while the end-cap regions extend the coverage to $1.0 < |\eta| < 2.7$. A schematic view of the MS and its various detector components is shown in Fig. 3.6.

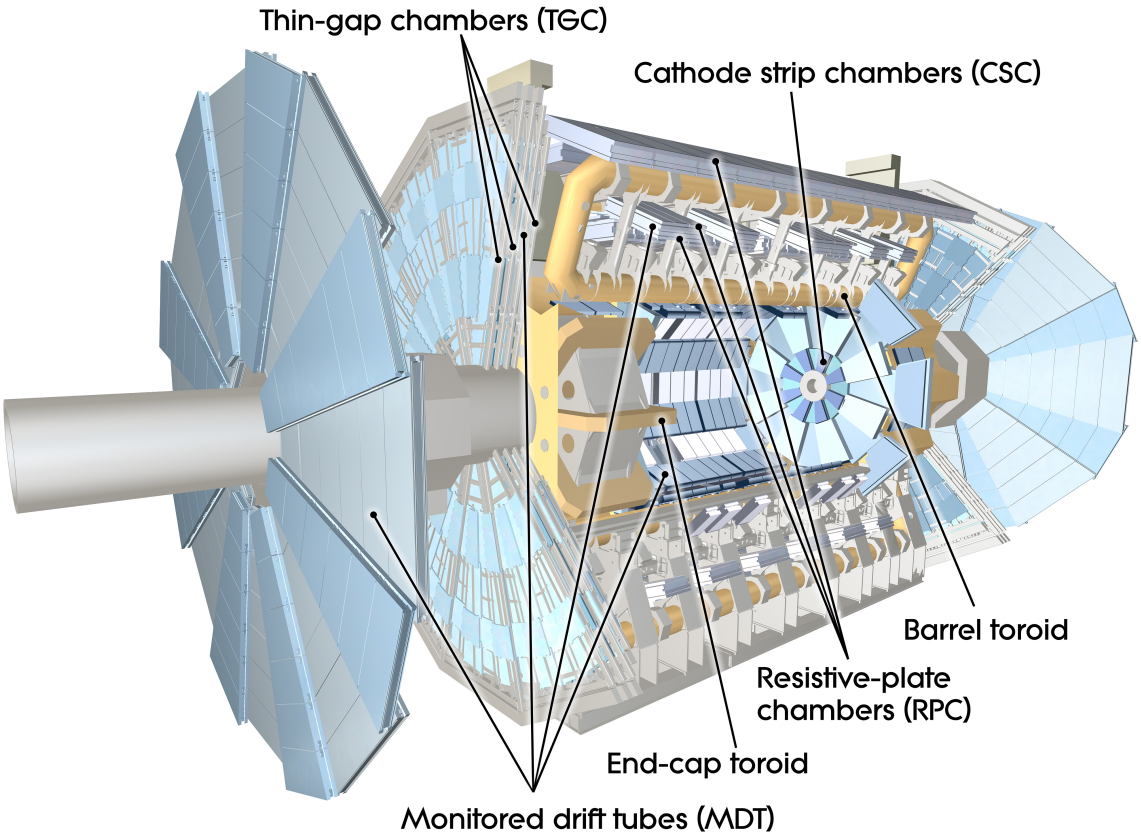


Figure 3.6. Schematic layout of the ATLAS MS showing the barrel and end-cap regions along with the locations of the different detector technologies used for muon tracking and triggering. Credit: CERN [18]

CHAPTER IV

EXPERIMENTAL UPGRADES

The highest peak integrated luminosity of the ATLAS detector to date was $\mathcal{L} = 2.61 \times 10^{34}$ cm^{-2}s^{-1}, which is beyond its original design specifications from the early 2000s for luminosity of $\mathcal{L} = 10^{34}$ cm^{-2}s^{-1}. As the LHC has steadily increased its instantaneous and integrated luminosity, the ATLAS detector has required a series of upgrades to cope with higher data rates, increased detector occupancy, and elevated radiation levels.

Beginning in approximately 2030, the LHC will enter the High-Luminosity phase (HL-LHC). During this period, the instantaneous luminosity is expected to increase to approximately

$$\mathcal{L} = 5 - 7.5 \times 10^{34} \text{ cm}^{-2}\text{s}^{-1}.$$

At this luminosity, an average of approximately 200 proton–proton interactions per bunch crossing is anticipated, compared to the typical 20–50 interactions observed during run 2. This dramatic increase in pileup presents significant challenges for event reconstruction, triggering, and data acquisition.

To meet these challenges and continue exploring the particle physics phenomena at the HL-LHC, the ATLAS detector is undergoing extensive upgrades. These upgrades are designed to improve radiation tolerance, increase detector granularity, enhance readout bandwidth, and maintain or improve physics performance under extreme operating conditions. Major upgrade components include a complete replacement of the ID with a new all-silicon Inner Tracker (ITk), upgrades to the Muon Spectrometer, new front-end and readout electronics for the calorimeters, and substantial improvements to the trigger and data acquisition systems.

The ATLAS upgrade program is divided into two phases. Phase 1 upgrades were completed during the Long Shutdown 2 period and commissioned by 2024. Phase 2 upgrades are scheduled for completion by 2030, prior to the start of HL-LHC operations.

4.1 Phase 1 upgrades

The Phase 1 upgrade program focused on improving detector performance and trigger capabilities in preparation for run 3 of the LHC. Key components of this phase included upgrades to the Muon Spectrometer, the introduction of new trigger electronics, and improvements to detector readout systems. These upgrades enabled ATLAS to operate efficiently at higher luminosities and increased event rates during run 3.

4.2 Phase 2 upgrades

The Phase 2 upgrade program is designed to prepare the ATLAS detector for sustained operation during the HL-LHC era and is scheduled for completion in 2030. Phase 2 will introduce significant upgrades to the ATLAS trigger and data acquisition system, on/off detector electronics upgrades for LAr Calorimeter, Tile Calorimeters, and the muon detectors. Phase 2 will also include a new tracking detector, High Granularity Timing Detector and Muon Chambers. The combined effects of integrated luminosity and the planned increase of instantaneous luminosity result in the ID no longer being sufficient for tracking and vertexing in ATLAS beyond run 3. Thus, an integral part of the phase 2 upgrades is the replacement of the ID with ITk.

The ITk is designed to accommodate the 200 proton-proton collisions per bunch crossing expected at the HL-LHC. To meet these demands, the detector features substantially higher granularity, enhanced radiation hardness, and a 1 MHz readout capability.

The design and performance of the ITk are described in detail in the ATLAS Technical Design Reports [19, 20], and the ITk forms the primary focus of this chapter.

4.3 ATLAS ITk

The primary goal of the ITk upgrade is to maintain or improve charged-particle tracking performance in the high-luminosity environment of the HL-LHC. Two major challenges must be addressed to achieve this goal: the substantially increased detector

occupancy due to high pileup, and the extreme radiation levels expected over the lifetime of the detector.

The innermost layers of the ITk are expected to experience radiation fluences exceeding 2×10^{16} n_{eq}/cm^2 and total ionizing doses of up to approximately 1.7 Grad. To operate reliably under these conditions, the ITk employs radiation hard silicon sensor technologies, advanced readout electronics, and a detector layout optimized for performance and longevity. The first layer of the ITk is also designed to be replaceable, allowing for potential replacement during the HL-LHC era.

ITk is split into two main systems: the Pixel Detector and the Strip Detector. A brief overview of the Strip detector will be given then the rest of this section will focus on the Pixel Detector as this is the area of ITk that the majority of the work for this dissertation was done.

4.3.1 ITk Strips. The ITk Strips surrounds the Pixel Detector and provides at least 4 hits for charged particles traversing the detector within a pseudorapidity range of $|\eta| < 2.7$. ITk Strips will start at about a radius of 400 mm and extend to 1000 mm and have $165m^2$ of silicon micro-strip sensors. The Strip Detector is made up of overlapping silicon strip sensors ITk Strips is designed to keep occupancy at $\sim 1\%$ during the HL-LHC runs.

4.3.2 ITk Pixels. ITk Pixels is made from two systems, the Inner System and the Outer System. The outer three layers of the ITk Pixels are called the Outer system. The innermost two layers of ITk Pixels are called the Inner System. The location of specific layer and pixel size for the Inner System can be found in Tab. 4.1 and 4.2. The basis of the whole ITk pixel detector is the pixel module, which detects the passage of charged particles. The pixel module is made of a silicon detector bonded directly to the front-end electronics for readout. The front-end electronics are designed by the RD53 collaboration, which has designed a front-end for ATLAS and CMS. The RD53 front-end being used for the Pixel Detectors is called the ITkPixV2. The pixel modules are built

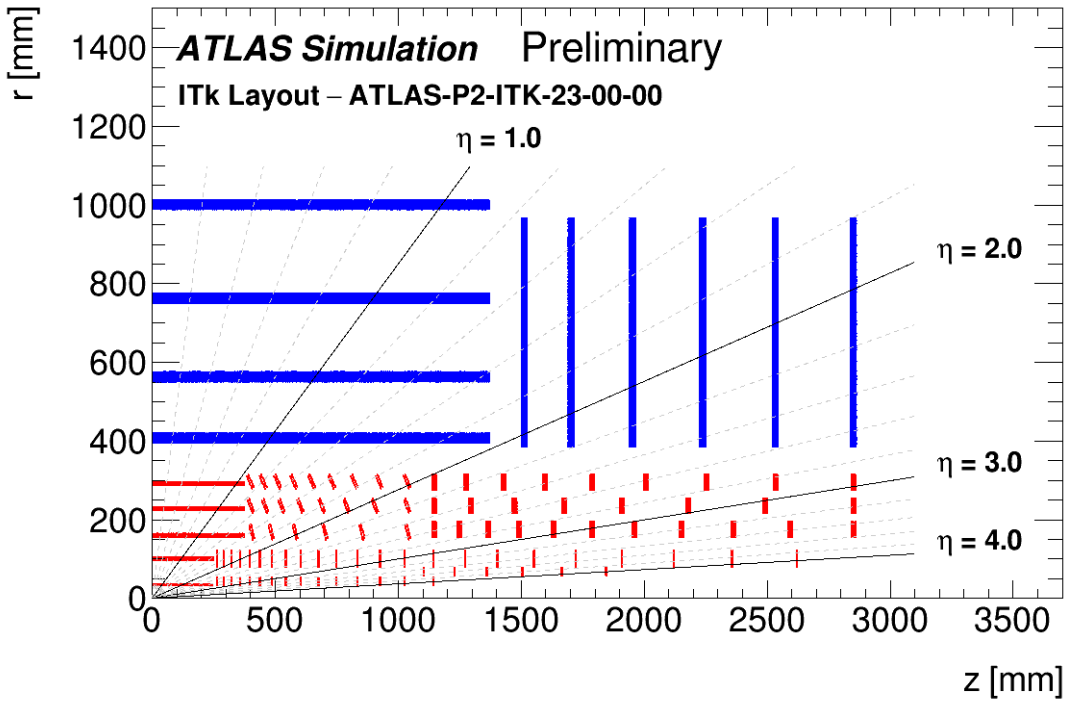
as either quad modules, 4 ITkPixV2 front-ends bump bonded to a single silicon sensor, or as triplets, 3 RD53 front-ends each bonded together to individual silicon sensors, as can be seen in Fig. 4.2. The pixel modules will be attached to local supports either rings or staves made of carbon fiber laminates and high thermal-conductive foam core with titanium pipes traversing the center for cooling. Cooling for ITk is provided by a CO_2 evaporative cooling system that is designed to maintain the temperature of the silicon sensors at -35°C to mitigate radiation damage effects and prolong sensor life. These rings and staves are mounted into shells that will provide outer structure for ITk as can be seen in Fig. 4.3.

The US ATLAS program is responsible for the two innermost layers of Pixel Detector called the Inner System. Assembly of the Inner System is being done at SLAC National Laboratory with major contributions from several universities and national labs all over the US. To facilitate this assembly a robust and efficient setup for module testing and quality assurance was needed at SLAC. Given the nature of ITk, once installed the detector will be inaccessible making it critical to ensure that all systems are fully functional before installation. To meet this requirement extensive testing is performed at each stage of the assembly process.

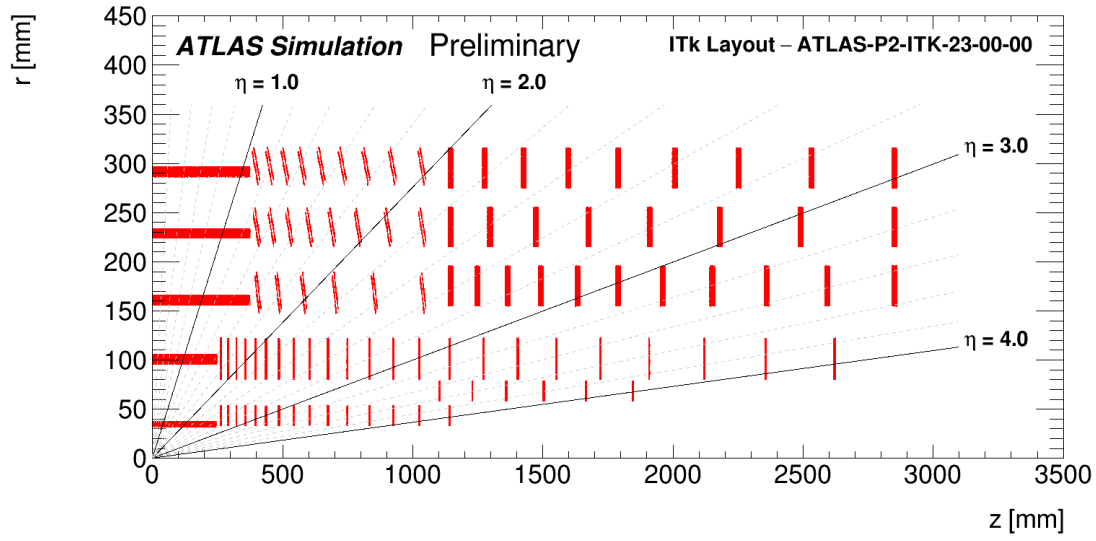
Table 4.1. Stave locations and pixel properties.

Layer	Radius [mm]	Z Range [mm]	Pixel Size [μm]	Sensor Thickness
L0	34	±245	25x100	270
L1	99	±245	50x50	100
L2	160	±372	50x50	150
L3	228	±372	50x50	150
L4	291	±372	50x50	150

The construction of the Inner Tracker (ITk) requires many components to be designed, manufactured, and assembled correctly. The components that make up the Inner System are the mechanical supports, the services, and the modules themselves.



(a) ITk Stave and Ring Layout [21]. Blue lines indicate ITk Strip stave and ring Locations. Red Lines indicate ITk Pixel stave and ring locations.

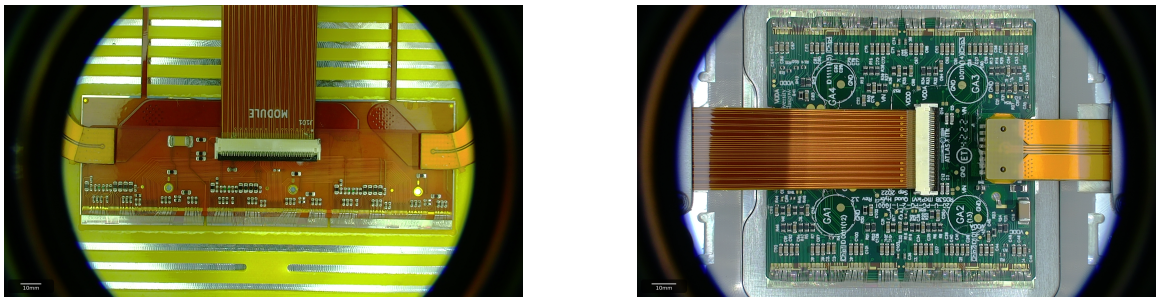


(b) Zoom in of ITK Pixel System [21]. Note that first two layers are the Inner System and the outside 3 layers are the Outer System.

Figure 4.1. Cut away view of ITk in one quadrant only. Layout is only in positive z direction. Full detector is symmetric about the z=0 and extends in a full cylinder around beam line. 4.1(a) Shows one quadrant of the full ITk. 4.1(b) Shows one quadrant of ITk Pixels.

Table 4.2. Pixel ring locations and sensor properties.

Layer	Radius [mm]	Pixel Size [μm]	Sensor Thickness [μm]
0	33.20	50x50	250
.5	58.7	50x50	250
1	80.00	50x50	150
2	154.50	50x50	150
3	214.55	50x50	150
4	274.60	50x50	150



(a) ITk triplet module (b) ITk quad module

Figure 4.2. View of ITk triplet and quad modules. Note the attached power and data flex cables attached.

The mechanical support structure consists of two main elements: local supports and shells. Each local support is constructed from a carbon-fiber laminate with a high thermal-conductivity foam core. These materials were chosen due to their high strength-to-weight ratio and good thermal conductivity. The low weight is important to the mission of ATLAS, as it minimizes the amount of material interactions that high energy particles undergo as they traverse the detector. The high thermal conductivity is important as effectively cooling the modules will reduce radiation damage and prolong the effective life of the detector.

The local supports include staves, which are straight structures used in the barrel region, and rings, which are circular structures used in the end-cap regions. Detector modules are directly bonded to the local supports using a thermally compound, SE4445. Although not actually a glue or adhesive, SE4445 provides the necessary adhesive to keep the modules precisely in place. SE445 also provides good thermal conductivity and is

sufficiently radiation tolerant to ensure that its properties do not significantly degrade under the high ionizing radiation doses expected at the HL-LHC.

A titanium cooling pipe runs through the center of each support structure, delivering evaporative CO_2 cooling directly to the detector modules.

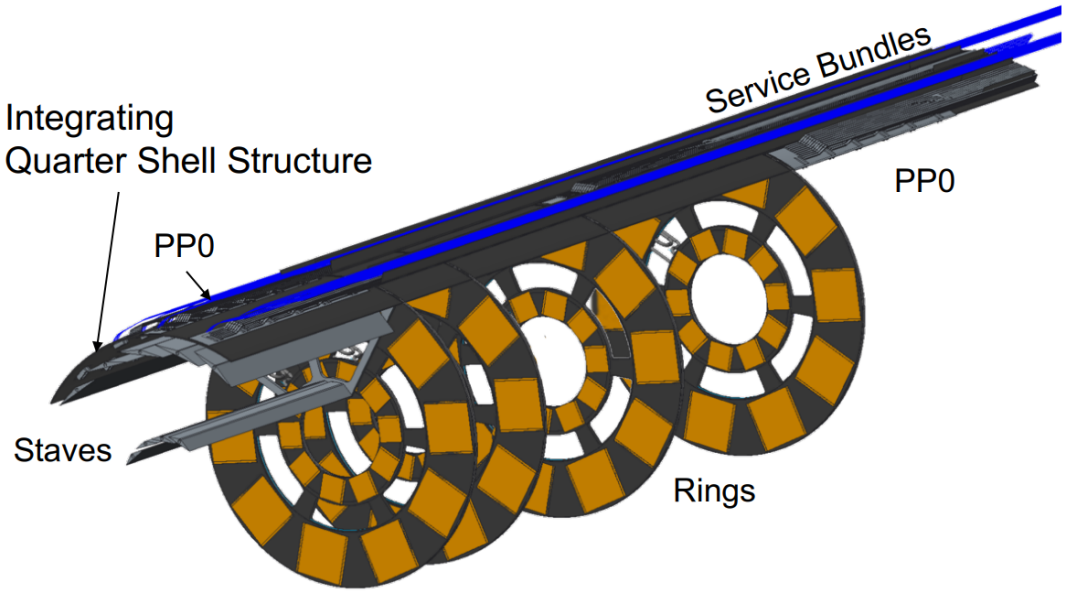


Figure 4.3. Schematic of the quarter shell support structure of the inner pixel system.

The local supports are mounted within larger quarter shell structures that provide mechanical stability and define the overall geometry of the Inner System. As the name suggests, each quarter shell is one quarter of the cylindrical structure. There are three sections that will be made in the Inner System, the inner barrel and two end-caps. A CAD model of a quarter shell for the barrel and one end-cap can be seen in Fig. 4.3. The barrel and end-cap structures are not rigidly constrained with respect to one another in the z-direction. The complete Inner System is supported such that it remains free to accommodate thermal and mechanical movements along the beam axis.

All electrical power and data lines are called services. Type 0 services route the power, DCS, and data via flex cables from the modules to patch panels (PP0). The PP0s

are mounted directly on the quarter shells and have several unique designs depending on their location and on whether they service quad or triplet modules. Type 1 services run from the PP0s to the edge of the detector with twinaxial cables. At the end of type 1 services the data is converted into optical signals, this is done outside the main detector volume due to the lack of radiation hard digital to optical converters.

Additional services are present further along the service chain, as illustrated in Fig. 4.4, but these components lie outside the Inner System and are therefore beyond the scope of this section.

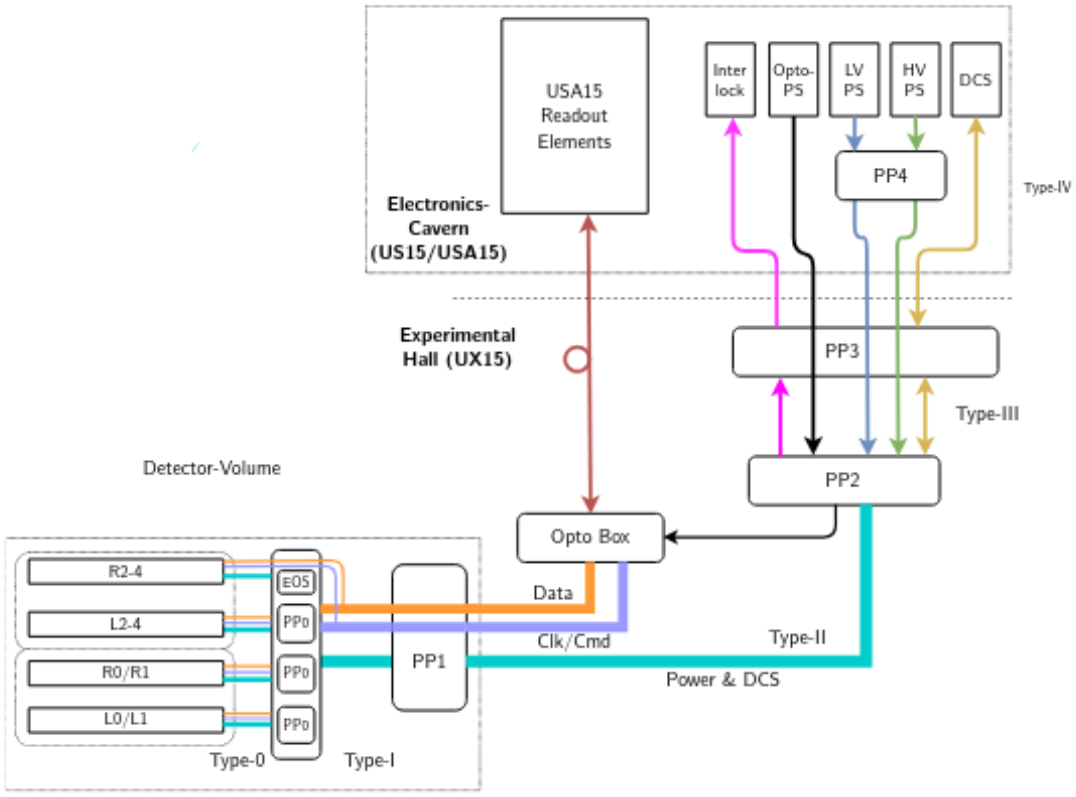


Figure 4.4. Schematic of ITk service chain.

The first step of integration is the called "loading". The process of loading involves bonding the modules directly to the local supports using the thermal compound SE4445. This process is of the utmost importance as it ensures that the modules are

precisely loaded with only 25 microns between modules. It is also important to ensure that the modules are able to dissipate heat effectively to the local supports, ensuring reduced radiation damage and longevity of the sensors.

Before loading the modules are extensively tested. Testing begins at the production sites where they validate the functionality of the modules. Once at SLAC the modules are visually inspected and electronically tested to ensure no damage occurred during shipping.

The local supports likewise are tested before loading. Again once shipped to SLAC they are tested visually and then using a CMM they are measured for flatness.

The loaded local supports then will be placed in a test box and cooled to -35°C. The test boxes were designed and partially constructed as part of the work contributing to this dissertation. Their design was driven by several key requirements: minimizing the internal volume to allow rapid drying of the enclosed air and thereby preventing condensation, providing electrical feedthroughs for power and data connections, accommodating different stave and ring geometries, and incorporating interlock systems to protect both operators and equipment. The final designs are shown in Fig. 4.5.

The stave test box employs two mirrored PP0 boards that accommodate power and data connections for all stave variants. To achieve this, the staves must be mounted in one of three distinct orientations. The required orientation depends on whether the flex-cable connector is located on the upper or lower side of the flex. This distinction reflects the cable-routing constraints of the detector. The 8 varieties of staves can be seen in Fig. 4.6

The ring test box requires three PP0 boards to accommodate the different types of rings. Due to the different angular locations of the cooling and data lines for different rings, the simplest solution for connecting all required services for testings was to fix all cooling line connections at a single location while allowing the PP0 boards to move.

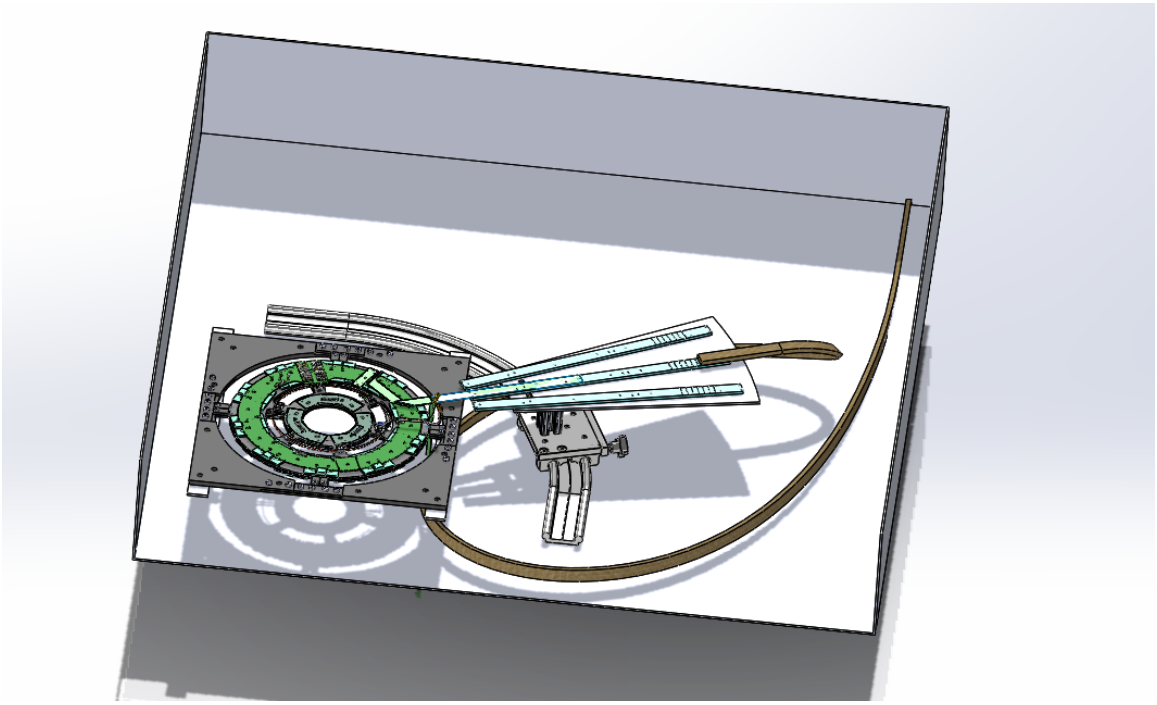
Consequently, the PP0 boards are mounted on a track that permits motion through a 120° arc around the ring, enabling all possible rings to be tested in one box.

To connect the cooling lines to the loaded local supports a connection will have to be made to the delicate titanium cooling pipes. This connection was developed at Argonne National Laboratory and is done by using a Yor-Lok like fitting with a special soft ferrule. Normally with a Yor-Lok fittings the tubing is compressed and deformed to create a tight seal against the ferrule and fittings. In this case the ferrule is made of a soft metal and deforms to create a tight seal against the titanium pipe without deforming the titanium pipe. This connection allows the local supports to be cooled to the operating temperature of -35°C while in the dry box.

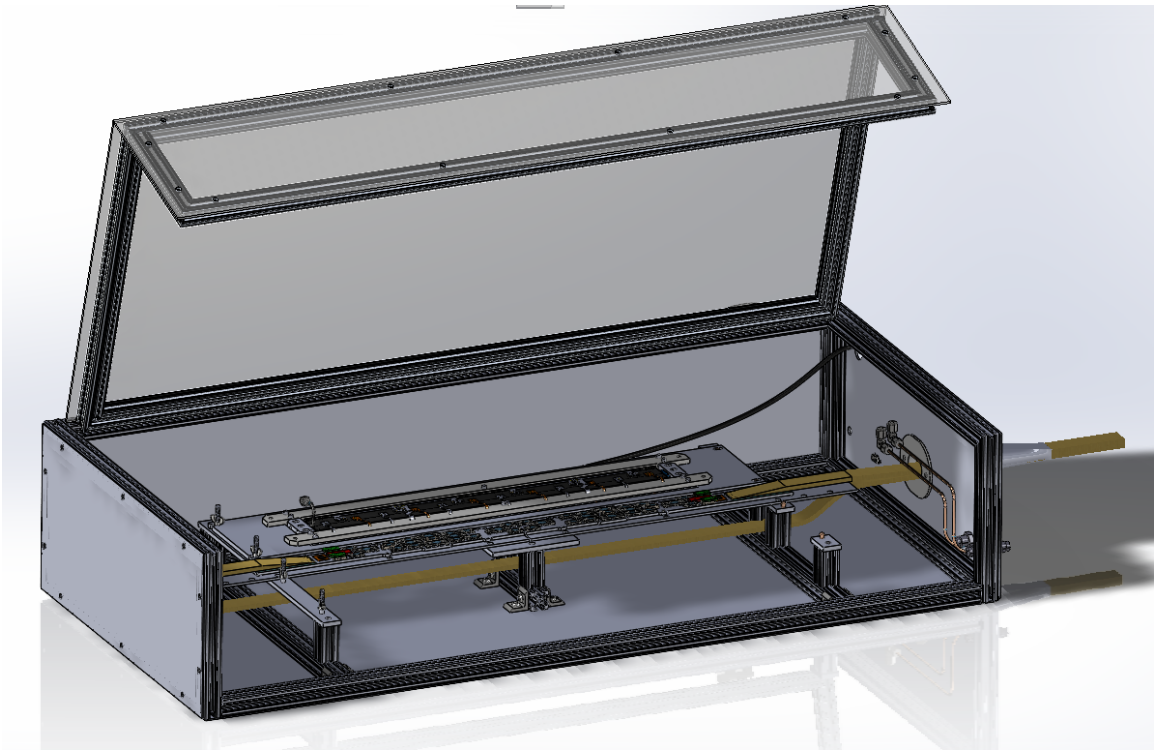
While at -35°C the local supports will undergo a series of tests to ensure that the modules are fully functional after loading. This test is imperative as it is the last chance to test the modules before the cooling pipes are welded together and the quarter shells are shipped to CERN. After testing the local supports are mounted in the shells the titanium cooling pipes are orbital welded together. The fully assembled shell will then be shipped to CERN for installation in ATLAS.

Due to thermal expansion and contraction during detector operation, the risk of mechanical damage to detector modules during thermal cycling was a major concern.

This concern is particularly relevant because the thermal coefficient of expansion (TCE) of carbon fiber can be as low as $-1.0 \times 10^{-6}\,\mathrm{K}^{-1}$, whereas silicon has a TCE of approximately $16.0 \times 10^{-6}\,\mathrm{K}^{-1}$. As a result, silicon expands with increasing temperature while carbon fiber may contract, leading to a significant mismatch in thermal expansion behavior. This mismatch in TCE has the potential to induce mechanical stress at the interface between the detector modules and the local supports, which could lead to delamination during repeated thermal cycling. To address this concern, a dedicated thermal cycling test was developed in which a pixel module was bonded to a representative local support structure and subjected to repeated temperature variations.

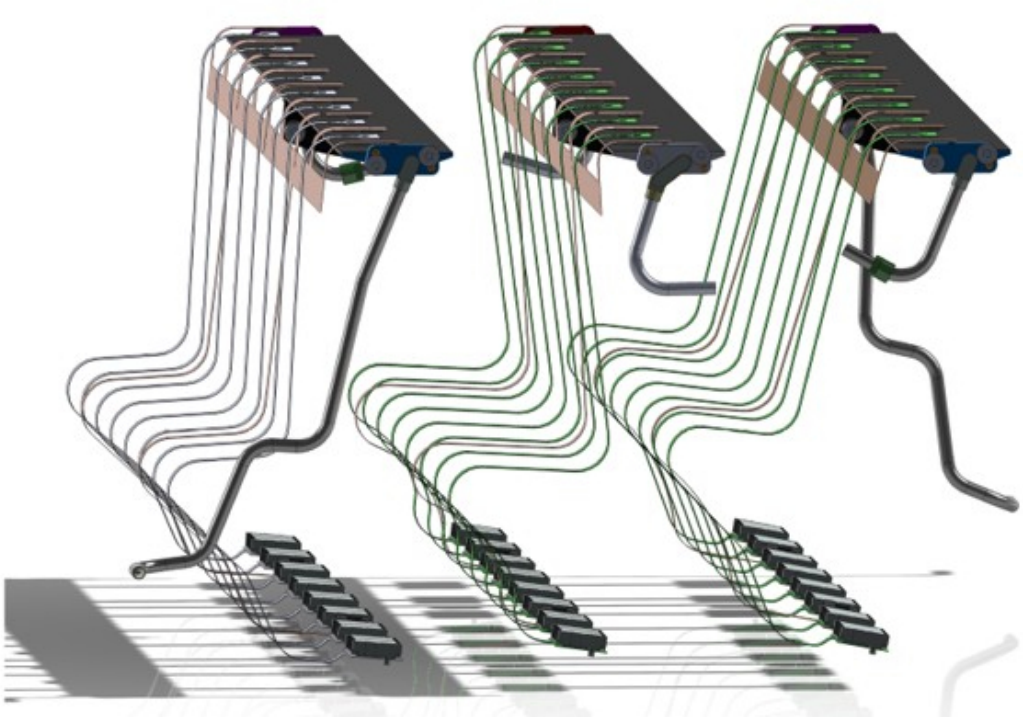


(a) Ring Box.

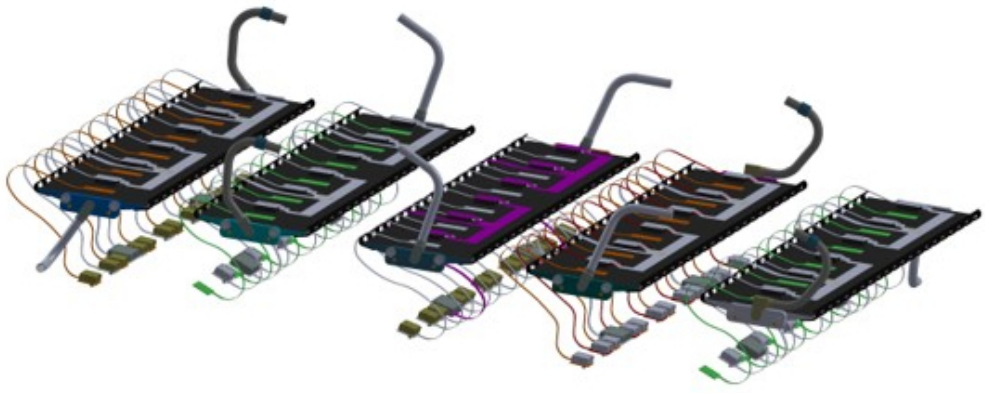


(b) Stave Box

Figure 4.5. CAD models of boxes used for loaded local supports.



(a) Layer 0 staves with triplet modules and flex cables, tan flexes are for power, green and gray flexes are for data



(b) Layer 1 staves with quad modules and flex cables, gray flexes are for power, orange, green, purple flexes are for data.

Figure 4.6. CAD models of the various staves for Layer 1 and Layer 2. Note the flexes are bend into shape of final cable routing.

For this test, a pixel module was glued to a piece of carbon fiber foam made from the same material used in production local supports. Stycast epoxy was used as the glue for this study. Although SE4445 is used in the final detector assembly, it was not employed for this test because it is initially very soft and becomes stiffer only after significant radiation exposure. Stycast epoxy is more rigid than SE4445 that has received the radiation dose expected in the HL-LHC, and therefore provides a conservative, worst-case scenario for evaluating thermal cycling robustness.

Once mounted, the module was thermally cycled between $-55°$C and $60°$C for a total of 100 cycles. Due to the design and stack of the module it expected that any damage induced by thermal cycling would most likely manifest as broken or disconnected bump bonds between the silicon sensor and front ends which we call delamination. To assess potential damage, a bump-bond scan was performed following the thermal cycling procedure. The bump-bond test operates by individually checking each pixel for capacitive coupling to its neighboring pixels. Charge is injected into the neighboring pixels surrounding the pixel under test, and the response of the central pixel is then measured. If a bump bond is broken, the pixel under test registers no signal. If the bump bond is intact, capacitive coupling between neighboring pixels produces a small but measurable charge, indicating a functional connection.

Results from the first 100 thermal cycles can be seen in Fig. 4.7 and Tab. 4.3. After the 100 thermal cycles 380 of the 460,800 total pixels changed to a disconnected status when compared to the baseline scan. The results show that the number of disconnected bump bonds at the start is roughly the same as the number of disconnected bump bonds after 100 thermal cycles, showing that delamination is not likely to occur during ITk operation in ATLAS. This test was continued to 1000 thermal cycles and the results were consistent with the 100 cycle test, showing no significant increase in disconnected bump bonds after 1000 thermal cycles.

Table 4.3. Table showing number of disconnected bump bonds after thermal cycling.

Thermal cycles	0	1	5	25	50	75	100
Chip 17759	1849	1965	1971	1982	1973	1992	1994
Chip 1774A	1488	1668	1683	1501	1755	1501	1720
Chip 17738	1470	1477	1487	1480	1487	1480	1473

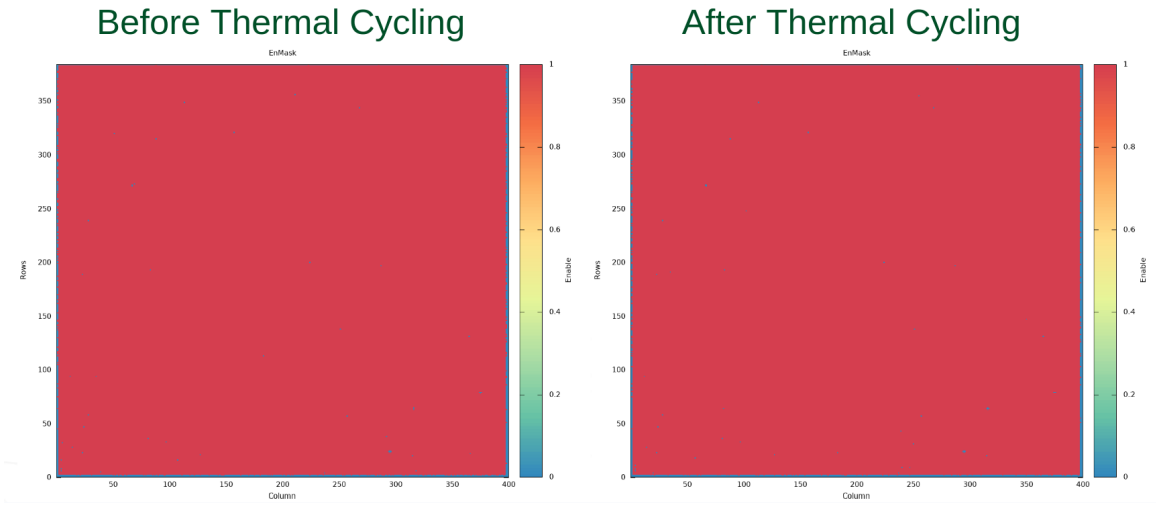


Figure 4.7. Disconnected bump bonds from one sensor before and after 100 thermal cycles. Blue pixels indicate disconnected bump bonds. Red pixels indicate connected bump bonds.

CHAPTER V

OBJECT RECONSTRUCTION

Once data sets are recorded in the ATLAS detector, they are initially stored in a raw format that is not directly suitable for physics analysis. A dedicated reconstruction chain is therefore applied to transform these raw detector signals into higher-level physics objects.

This section describes the reconstruction of the main physics objects used in ATLAS. It is important to note that all reconstructed objects are subject to finite resolution and potential misconstruction effects. For example, a reconstructed track may arise from a random combination of detector hits, and reconstructed electrons or other particle candidates may originate from alternative physical processes or detector effects.

As a result, each reconstructed object is associated with a quantified probability of correctly representing the underlying true particle. Understanding and controlling these reconstruction uncertainties is essential for precision measurements and searches for rare processes.

5.1 Tracking

Tracks are reconstructed objects in the ATLAS detector and are used to describe the trajectories of charged particles produced in pp collisions. They provide measurements closest to the beam line and are therefore essential for vertex reconstruction and for associating tracks to the primary interaction vertex. Track reconstruction is performed in multiple stages in order to balance reconstruction efficiency with computational cost.

5.1.1 Track Reconstruction.

The first pass of track reconstruction proceeds through the following steps:

- **Clustering:** The first step of tracking is to group individual sensor hits in the Inner Detector into clusters. A hit is defined as energy deposited in a pixel above

a predefined threshold. Neighboring hits are merged into clusters, where neighbors are defined as pixels sharing an edge or a corner, up to eight neighbors. A neural network is then applied to identify clusters that may originate from multiple particles, merged clusters, and to estimate their properties.

- **Seeding:** Clusters in different detector layers are combined to form track seeds. These seeds are typically constructed from triplets of clusters that are consistent with a signal particle trajectory. The seeds are required to pass requirements on the transverse momentum and impact parameters.

- **Track Building:** The seeds are used to estimate initial track parameters, which are then extrapolated through the detector to search for compatible clusters in subsequent layers. This process is performed using a Kalman filter formalism, which iteratively updates the track parameters and their uncertainties as additional measurements are incorporated.

- **Ambiguity Resolution:** Multiple track candidates can share clusters or represent duplicate reconstructions of the same particle. An ambiguity resolution procedure is applied to select the best set of tracks by assigning a score based on criteria such as the number of hits, shared hits, missing hits, and track fit quality. Tracks failing to meet a defined threshold are discarded.

- **Extension to the TRT:** Finally, track candidates are extended into the TRT, where additional hits can be associated to improve momentum resolution and particle identification.

The result of the tracking algorithm is track objects defined by a helical path through the detector with 5 variables, $(d_0, z_0, \phi, \theta, \frac{q}{p})$.

For tracks to be kept they must pass a set of requirements. Until recently standard tracks were only considered to be valid if they had at least 7 silicon hits. This has recently changed and new standard tracking now requires at least 8 silicon hits.

Interestingly, the number of tracks reconstructed is roughly linear in pileup, μ. If pileup is too high though it becomes nonlinear due to fake track reconstruction starting to dominate.

5.1.2 Tracklet Reconstruction. After the first pass tracking procedure is completed, a second-pass tracking algorithm is performed to reconstruct tracklets, defined as short tracks composed mainly of hits in the pixel detector. This second-pass reconstruction uses hits that were not assigned to tracks in the primary tracking stage.

Tracklets are seeded exclusively from pixel detector clusters, as the primary goal is to identify charged particles that decay within the Inner Detector volume. To ensure sufficient reconstruction quality, at least three pixel hits are required. The selection criteria used for tracklet reconstruction are summarized in Tab. 5.1.

Table 5.1. Summary of tracklet reconstruction requirements.

Selection
$p_T > 5\,\text{GeV}$
$\lvert\eta\rvert < 2.2$
Pixel clusters ≥ 3
Pixel holes $= 0$
Shared hits $= 0$
$d_0 < 10$ mm
$z_0 < 250$ mm

5.1.3 Vertex Updater. Tracklets used in this analysis are reconstructed from a limited number of hits in the pixel detector, resulting in a relatively short lever arm for momentum measurement. This leads to a correspondingly large uncertainty in the transverse momentum, which scales approximately as

$$\sigma_{p_T} \propto \frac{1}{L^2},$$

where L is the effective lever arm of the track fit. A detailed discussion of momentum reconstruction and its associated uncertainty is given in Secs. 5.3.1 and 5.3.2.

For pixel only tracklets that hit all four pixel layers, the lever arm is the distance between the innermost pixel layer (IBL) and the outermost pixel layer, corresponding to approximately 90 mm in the transverse plane, see Fig. 3.3. If the particle is instead assumed to originate from a reconstructed vertex, the effective lever arm increases to approximately 122.5 mm, resulting in a significant improvement in momentum resolution.

To exploit this, a vertex-constrained refit is applied to tracklets after reconstruction. The procedure is as follows:

- Tracklets are reconstructed using the normal second-pass tracklet reconstruction.
- The distance between each tracklet and all reconstructed vertices (including pile-up vertices) is computed.
- Each tracklet is refitted under the hypothesis that it originates from the nearest vertex.
- The track parameters are updated, with the perigee defined relative to the selected vertex, resulting in a vanishing impact parameter by construction.

This procedure increases the effective lever arm by approximately 33 mm, leading to improved momentum resolution and better agreement with the true particle kinematics in simulation. Unless otherwise stated, the vertex-constrained momentum is used throughout this dissertation when referring to tracklet p_T.

5.1.4 Kinked Tracklets. An additional second-pass tracking algorithm, known as Large Radius Tracking (LRT), is performed to reconstruct displaced tracks originating away from the interaction point. A summary of the LRT requirements is provided in Tab. 5.2.

Kinked tracklets are identified by associating tracklets with LRT tracks. A kink candidate is defined when a tracklet and an LRT track have a distance of the closest

approach less than 1.5 mm, with the position of the closest approach occurring within a radius of 122.5 mm to 300 mm.

These kinked signatures can arise from two primary sources: particles material interactions or the decay of a long-lived particle within the detector volume.

Table 5.2. Summary of LRT reconstruction requirements.

Requirement	LRT
max. d_0 [mm]	300
max. z_0 [mm]	500
min. p_{T} [GeV]	1
max. $\lvert\eta\rvert$	3.0
max. silicon holes	1
max. double holes	0
max. hole gap	1
road width [mm]	5
seeding	SCT only
min. silicon hits	8
min. unshared silicon hits	6
max. track χ^2/DoF	9

5.1.5 Soft Pion. A dedicated reconstruction procedure is used to identify soft pion originating from the decay of short-lived charged particles. This reconstruction is performed after the tracklet reconstruction stage. In this approach, track seeds are only considered if they are consistent with originating from the endpoint of a reconstructed tracklet. This requirement significantly reduces combinatorial background while maintaining high efficiency for signal-like decays. To further reduce computational cost, the soft pion reconstruction is restricted to tracklets satisfying $p_T > 20\,\mathrm{GeV}$ and isolated from nearby high-momentum tracks. In particular, tracklets are required to be separated from tracks with $p_T > 500\,\mathrm{MeV}$ within a cone of $\Delta R < 0.4$.

This reconstruction achieves high efficiency for soft pion originating from signal events [22].

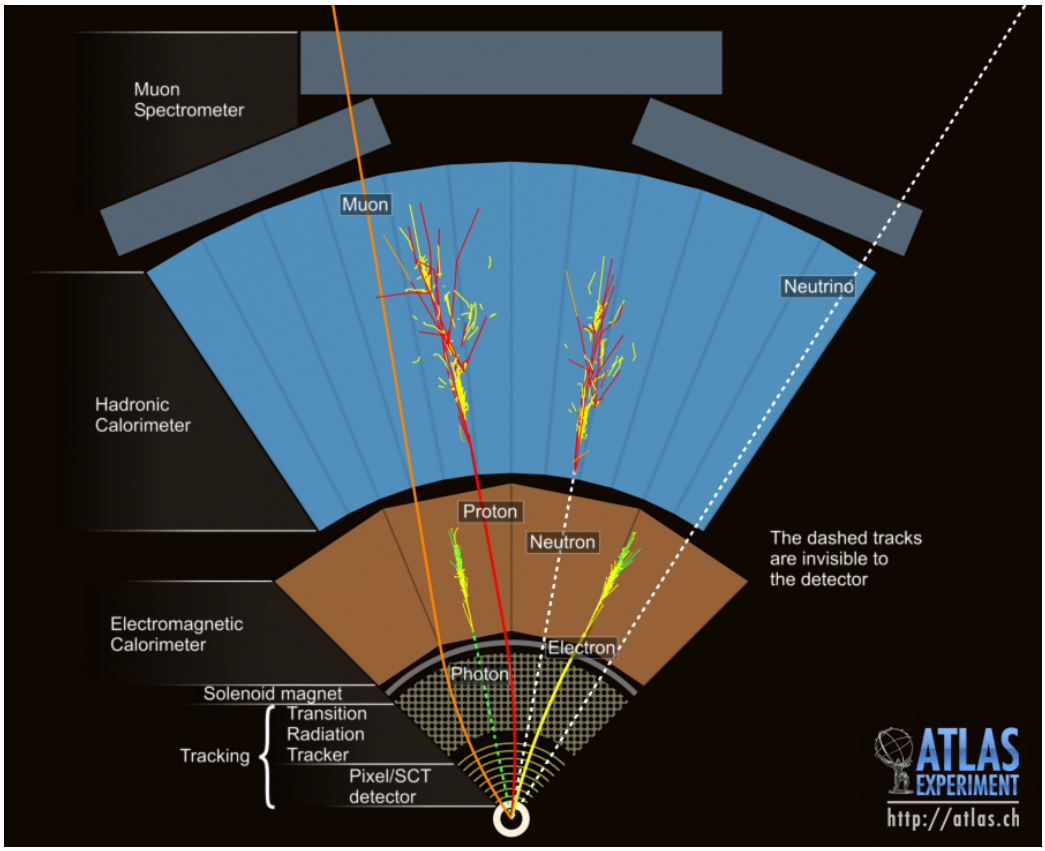


Figure 5.1. Schematic view of the various signals of different common SM particles [23].

5.2 Object Reconstruction

In addition to tracking of charged particles there are various other high level physics objects that are reconstructed for physics analysis. For the reconstruction of physic objects every subsystem is important and plays a role. The key to object reconstruction is using the various subsystems to identify and measure various particles that either pass through or are stopped in the detectors. In Fig. 5.1 you can see the various objects reconstructed and typical signals.

5.2.1 Election. As electrons traverse detector material, they predominantly lose energy via bremsstrahlung radiation. The emitted photons may subsequently convert into electron–positron pairs, which deposit energy in the calorimeters and can produce associated tracks in the ID. A key feature of this process is

the development of collimated electromagnetic showers. In some cases, these showers may begin in the ID material, leading to additional nearby hits or reconstructed tracks.

Electrons are reconstructed by first forming localized energy clusters in the electromagnetic calorimeter, which serve as seeds for electron candidates. ID tracks are then associated with these calorimeter clusters based on spatial and kinematic matching. A subsequent refinement step is performed, in which tighter selection criteria are applied to improve the discrimination between photon and electrons. [24].

5.2.2 Muon. Muons are another object reconstructed in the ATLAS detector. Due to their large mass and weak interactions with matter, muons typically pass through the various detector subsystems and leave only small amounts of ionization energy. Muons are reconstructed as four different types depending on the way they were reconstructed [25].

5.2.2.1 Combined Muon. Tracks are first reconstructed independently in ID and MS subsystems. A global track refit is then performed using hits from both the ID and MS.

The reconstruction typically follows an outside-in approach, where tracks reconstructed in the MS are extrapolated inward toward the interaction point and matched to corresponding ID tracks. A combined fit is then performed, incorporating measurements from both detectors.

5.2.2.2 Segment-tagged Muon. Muons can also be identified using segment-tagging. In this approach, ID tracks are extrapolated into the MS and matched to at least one reconstructed track segment in the MS. This method allows for the identification of muons that cross only one layer of the MS due either to their low-p_T or that they are outside normal acceptance regions of the MS.

5.2.2.3 Calorimeter-tagged muons. Muons may also be identified by matching ID tracks to energy deposits in the calorimeter that are consistent with a MIP.

This approach is particularly useful for recovering efficiency in regions where the MS has reduced acceptance, such as detector gaps required for services and support structures.

5.2.2.4 Extrapolated muons. In the forward regions, the η coverage of the MS extends beyond that of the ID. As a result, some muons in the forward region have no reconstructed ID track to be associated with. These are extrapolated muons and are reconstructed using only the MS.

5.2.3 Jet. Due to color confinement quarks do not propagate freely. Instead, quarks in pp collisions will undergo hadronization. During hadronization many color natural hadrons are produced in a collimated jet. These collimated particles in the jet will deposit energy mostly inside the hadronic calorimeter. Topo-clusters (topologically-grouped cells of energy deposits in the calorimeters) are formed as the first step of jet reconstruction [26]. Then most jets are formed using an anti-kt algorithm [27].

5.2.4 Missing Transverse Energy. The pp collisions by design in ATLAS start with no momentum in the transverse plan. Due to the properties of hadrons the momentum carried by each parton is just fraction of the total momentum of the hadron. Meaning it is not known the initial momentum of the parton that undergo hard scattering. Due to the conservation of momentum if the initial momentum in the transverse plane is zero then the final momentum in the transverse plane must also be zero. In a perfect detector the momentum of every particle produced would be measured and the vector sum of all momentum in the transverse plane would be zero. However, in practice ATLAS is unable to detect every particle produced. For example, in the standard model the neutrino doesn't leave any measurable signal in the detector. In addition, many BSM searches predict DM candidates which are also weakly interacting and escape any detection. This lack of detection provides a handle to measure potential DM models. Missing transverse energy (MET) is a measure of how much energy escapes detection in the ATLAS detector. Normally, MET is calculated as the vector sum

required to balance all other physics objects p_T out to zero, including the "soft term". The soft term is just momentum not associated with any other physics object, but that is measured in the detector.

5.3 Measurements

For this dissertation there are two important measurements; tracks momentum and the ionization energy loss of a particle.

5.3.1 Momentum. Track momentum measurements rely on the magnetic field bending the charged particle path. From the Lorentz force we can see that a particle must make a circular path in a uniform magnetic field,

$$\mathbf{F} = q(\mathbf{E} + \mathbf{v} \times \mathbf{B})$$

Thus, if we assume the magnetic field inside the ID is uniform we measure the momentum by first measuring deviation of a particle from a straight line and using that to find the result of the Lorentz force and thus the resulting momentum. This is done by first measuring the sagitta of the track. The sagitta is defined as the distance from the midpoint of an arc to the chord of that arc, see Fig. 5.2.

The sagitta can be related to radius of a circle by,

$$(R - s)^2 + \frac{L^2}{4} = R^2 \tag{5.1}$$

Now with some gentle work

$$s = R\left(1 - \sqrt{1 - \frac{L^2}{4R^2}}\right) \tag{5.2}$$

Noting that $L \ll R$ for many particles in the ATLAS detector we can expand 5.2 in terms of $\frac{L}{R}$,

$$s = \frac{L^2}{8R} \tag{5.3}$$

With the assumption that the magnetic field inside the ID is uniform and pointing along the beam line we can simply the Lorentz force and combine with Eq. 5.3 to get,

$$Pcos(\theta) = .3zBR = z\frac{.3BL^2}{8s} \tag{5.4}$$

Where B is defined as the uniform magnetic field the particle is passing through in units of Tesla. z is the charge of the particle. L is the lever arm length and s is the sagitta as shown in Fig. 5.2, in units of meters.

5.3.2 Momentum Error. Momentum error can be found by starting with equation 5.4 and assuming that $z = 1$.

$$P = .3BR \rightarrow \sigma_P = .3B\sigma_R \tag{5.5}$$

Which dividing by P on both sides and using 5.4 again we return to.

$$\frac{\sigma_P}{P} = \frac{\sigma_R}{R} \tag{5.6}$$

Now we can find the relation for σ_R by using 5.3 and the standard error propagation term,

$$\sigma_R = \sqrt{\left(\frac{1}{4}\frac{L^2}{s}\right)^2 \sigma_L^2 + \left(\frac{1}{8}\frac{L^2}{s^2}\right)^2 \sigma_s^2} \tag{5.7}$$

Where we can assume that $\sigma_L \ll \sigma_s$ meaning that we can put this all together to get

$$\sigma_R = \left(\frac{1}{8}\frac{L^2}{s^2}\right)\sigma_s \tag{5.8}$$

Then we use equation 5.6 to change back to the relevant measurements.

$$\frac{\sigma_P}{P} = \frac{1}{8}\frac{L^2}{Rs^2}\sigma_s \tag{5.9}$$

We can remove the s with equation 5.3.

$$\frac{\sigma_P}{P} = \frac{8R}{L^2}\sigma_s \tag{5.10}$$

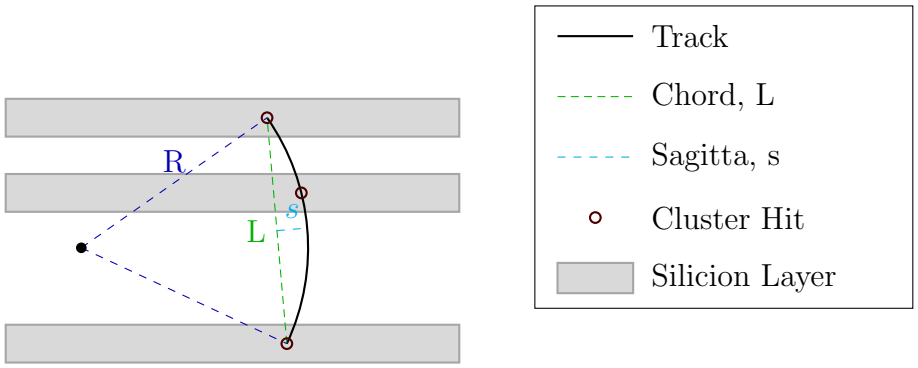


Figure 5.2. Schematic view of sagitta measurement for three hits in silicon. Note, not draw to scale.

Using equation 5.4 the result can be expressed in terms of the B field, momentum, lever arm, and error on the sagitta.

$$\frac{\sigma_P}{P^2} = \frac{8}{0.3BL^2}\sigma_s \tag{5.11}$$

The resulting expression, Eq. 5.11, highlights the importance of maximizing the track lever arm in the ATLAS detector, as the transverse momentum resolution scales inversely with the square of the lever arm, $\sigma_P \propto L^{-2}$.

5.4 dEdx measurements

Ionization energy loss is the description of energy deposited into matter as charged high energy particles pass through. For the Inner Detector most particles are high energy and thus normally pass through matter without a significant change in energy. In addition, the silicon in the Inner Detector is thin. However, the ionization energy loss in inherently a statistical process. With these assumptions the probability of ionization energy loss can be approximated.

5.4.1 Small number of collisions. With the assumption that the number of collisions is small it can also be assumed that the energy transferred is small compared to the total energy. That is

$$\langle \Delta E \rangle \ll E,$$

In this assumption is the implicit assumption that are no hard scatterings as a particle passes through the matter. This also means the trajectory of the particle can be considered approximately unperturbed by ionization losses. In this regime, the number of collisions in a thickness x is given by

$$\bar{\mathrm{N}} = x \frac{d\mathrm{N}}{dx}.$$

Since individual collisions are statistically independent, the probability of observing N collisions follows a Poisson distribution,

$$P(x, \mathrm{N}) = \frac{\bar{\mathrm{N}}^{\mathrm{N}}}{\mathrm{N}!} e^{-\bar{\mathrm{N}}} \tag{5.12}$$

The probability density W_1 of a single collision with energy loss of ω is defined as

$$W_1(\omega) = \frac{d^2\bar{\mathrm{N}}}{dx d\omega} \Big/ \frac{d\bar{\mathrm{N}}}{dx} = \frac{1}{\sigma} \frac{d\sigma}{d\omega}, \tag{5.13}$$

with the normalization condition

$$\int_0^\infty W_1(\omega)\, d\omega = 1.$$

For a fixed number of collisions N, the total energy loss distribution is obtained through repeated convolution of single-collision distributions,

$$W_N(\omega) = \underbrace{W_1 * W_1 * \cdots * W_1}_{N \text{ times}}. \tag{5.14}$$

The convolution is defined as

$$(W_1 * W_1)(\omega) = \int_0^\omega W_1(\omega') W_1(\omega - \omega') d\omega'. \tag{5.15}$$

A special case arises for $N = 0$, corresponding to no interactions in the material. In this case, the energy loss distribution is a Dirac delta function,

$$W_0(\omega) = \delta(\omega). \tag{5.16}$$

The full energy loss distribution is then given by the weighted sum over all possible numbers of collisions,

$$f(x,\Delta) = \sum_{\mathrm{N}=0}^{\infty} \frac{\bar{\mathrm{N}}^{\mathrm{N}}}{\mathrm{N}!} e^{-\bar{\mathrm{N}}} W_{\mathrm{N}}(\Delta). \tag{5.17}$$

This formulation is most useful in the regime where $\bar{\mathrm{N}} \sim \mathcal{O}(1)$, since W_{N} for high number of N quickly goes to zero.

5.4.2 Landau. In the regime of where there are many collisions, the previous discrete formulation becomes impractical. The landau method handles this case by assuming the probability per length of a given energy loss at a given energy satisfies the transport equation, as

$$\frac{\partial f(x,\Delta)}{\partial x} = \int_0^{T_0} w(\omega)[f(x,\Delta-\omega) - f(x,\Delta)]d\omega \tag{5.18}$$

with initial condition

$$f(x=0,\Delta) = \delta(\Delta).$$

Note that T_0 is the maximum energy transfer from a single collision and

Here, $w(\omega)$ is the differential interaction rate per unit length,

$$w(\omega) = \bar{\mathrm{N}} W_1(\omega) = x\frac{d^2\bar{\mathrm{N}}}{dxd\omega} = xn_a\frac{d\sigma}{d\omega} \tag{5.19}$$

Where $w(\omega)$ is the probability of energy loss ω of a particle per unit path and n_a is the number density of scatterings.

This equation can be solved using a Laplace transform,

$$L(f(x,\Delta)) \equiv \int_0^{\infty} f(x,\Delta)e^{-p\Delta}d\Delta = e^{-G(x,p)} \tag{5.20}$$

where we can define that

$$G(x,p) = \int_0^{T_0} w(\omega)\left[1 - e^{-p\omega}\right]d\omega \tag{5.21}$$

Where the inverse transform yields the final solution

$$f(x,\Delta) = \frac{1}{2\pi i}\int_{i\infty}^{-i\infty}\left[e^{p\Delta - G(x,p)}\right]dp \tag{5.22}$$

Eq. 5.22 provides an exact description of the energy loss distribution. However, in practice it cannot be evaluated in closed form.

In the thin absorber limit, this formalism reduces to the well-known Landau distribution, which describes the characteristic asymmetric fluctuations in energy loss observed in thin materials such as silicon sensors. This distribution provides a good description of measured dE/dx spectrum in tracking detectors, where the number of collisions is relatively small.

5.4.3 Bethe–Bloch. The mean ionization energy loss per unit length for a particle with velocity β is given by the Bethe-Bloch equation,

$$\left\langle -\frac{dE}{dx}\right\rangle = Kz^2\frac{Z}{A}\frac{1}{\beta^2}\left[\frac{1}{2}\ln\left(\frac{2m_e c^2\beta^2\gamma^2 W_{\max}}{I}\right) - \beta^2 - \frac{\delta(\beta\gamma)}{2}\right] \tag{5.23}$$

The definitions of the variables used in Eq. 5.23 are given in Table 5.3. The Bethe-Bloch prediction for a muon traversing silicon is shown in Fig. 5.3 [5].

The density correction term $\delta(\beta\gamma)$ accounts for the screening of the incidents particles electric field by atomic electrons of the absorber medium. This becomes increasingly important at high $\beta\gamma$, where the Lorentz contraction of the particle's electric field squishes it into a disk transverse to the direction of momentum, enhancing the role of medium screening. As a result, the correction depends on the material density and modifies the relativistic rise of the energy loss at high momentum.

There are corrections that can be applied to make Eq. 5.23 describe experimental data more accurately, as found in [5]. However, the expression provides a useful conceptual understanding of the relationship between the mean energy loss and the relevant particle properties.

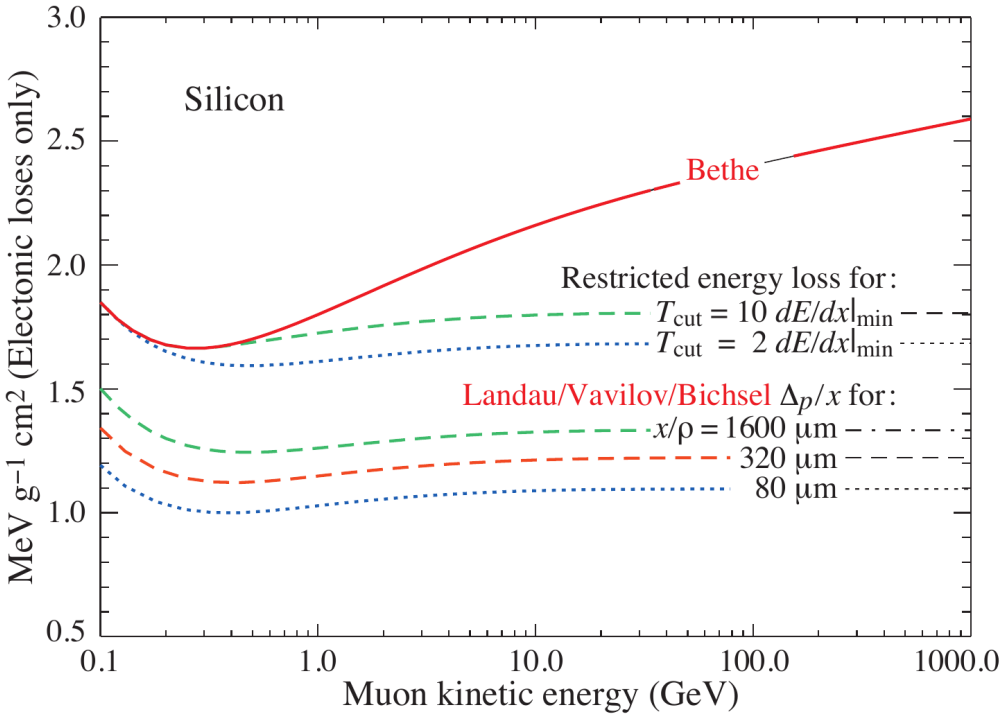


Figure 5.3. Bethe-Bloch $\mathrm{d}E/\mathrm{d}x$ for muons incident on silicon [5].

Table 5.3. Definitions of variables used in the Bethe-Bloch equation.

Symbol	**Definition**
K	Constant $4\pi N_A r_e^2 m_e c^2$
N_A	Avogadro's number
r_e	Classical electron radius
m_e	Electron mass
z	Charge of incident particle
Z	Atomic number of absorber
A	Mass number of absorber
I	Mean excitation energy of absorber
$W_{\max}$	Maximum energy transfer in a single collision
β	v/c of incident particle
γ	Lorentz factor $1/\sqrt{1-\beta^2}$
δ	Density correction term

CHAPTER VI

DISAPPEARING TRACKS

6.1 Preface

The proceeding sections of this chapter are from published works by the ATLAS collaboration [1]. The work contributing to this dissertation as part of this search focuses primarily on the addition of two slepton models. In particular, the $\tilde{\tau}$ GMSB and $\tilde{\tau}$ co annihilation models as described in Sec. 2.3, their addition to the disappearing track search, slepton generation in a model never explored on ATLAS, the validation of the samples, checking of event selection in comparison to the $\tilde{\chi}^{\pm}$ models, and event reweighting.

This work included the generation of $\tilde{\tau}$ CMSSM coannihilation samples based on the model described in Sec. 2.3.1. These samples had not previously been produced within ATLAS.

Due to the requirement that disappearing tracks decay inside the ID, the shortest lifetime samples were obtained by reweighting $\tilde{\tau}$ signal samples from a lifetime of 1 ns down to 0.02 ns to allow them to cover the same region as the $\tilde{\chi}^{\pm}$ models.

Both $\tilde{\tau}$ models (GMSB and CMSSM coannihilation) were compared to the $\tilde{\chi}^{\pm}$ models to verify that the selection efficiency was consistent across all signal models.

Finally, the validation regions were checked for signal contamination. It was found that the $\tilde{\tau}$ model exhibits significant contamination in the MET 150-300 GeV validation region. As a result, this region was changed to a signal region SR prior to unblinding.

Lastly the $\tilde{\tau}$ GMSB model has been included in the summary plot produced by ATLAS, Fig. 6.1

For completeness, the full published paper is presented in this chapter.

6.2 Introduction

Supersymmetry (SUSY) [29–34] is a theoretical framework based on a space-time symmetry that predicts the existence of a partner for each Standard Model (SM)

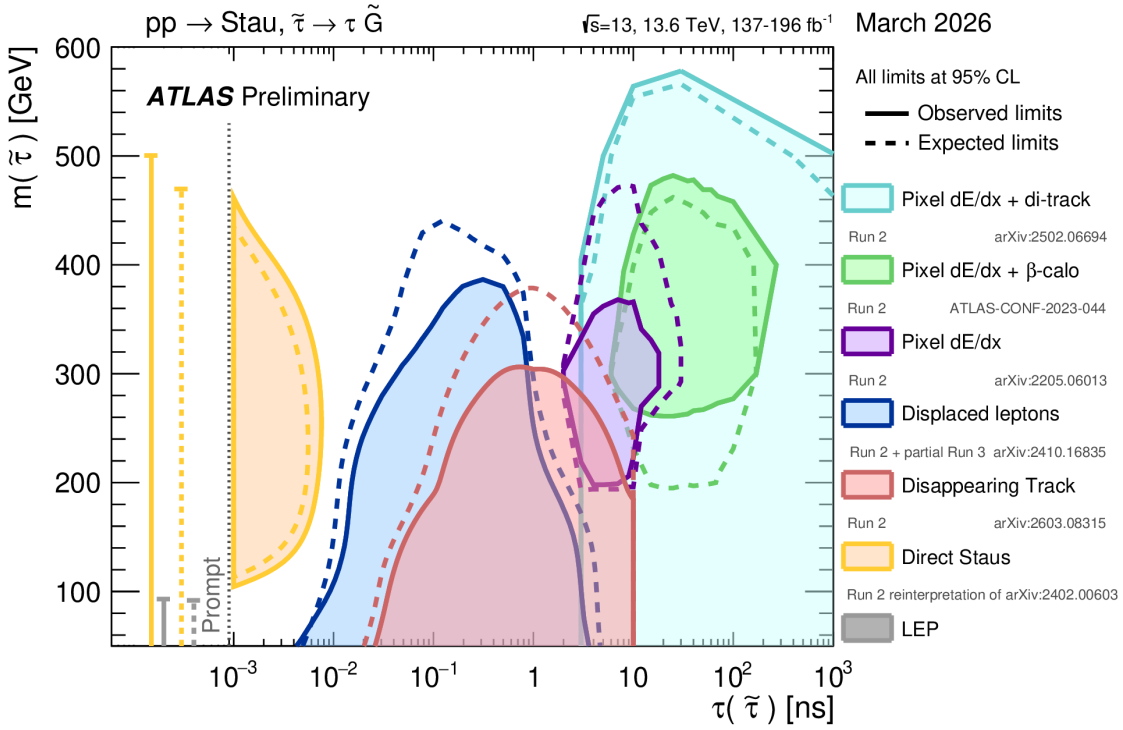


Figure 6.1. Summary of exclusion limits on $\tilde{\tau} \to \tilde{G}\tau$ from various ATLAS searches [28].

particle. These partner particles have the same quantum numbers as their SM counterparts, but differ by one half unit of spin. SUSY offers a solution to the hierarchy problem [35–38] if some of the partner particles have masses around the electroweak scale. The supersymmetric partners are named to reflect their SM counterparts: for example, the τ-slepton is the SUSY partner of the τ-lepton. The supersymmetric partners of the electroweak gauge bosons and the Higgs bosons, collectively referred to as electroweakinos, consist of the bino and winos and the higgsinos, respectively. These states mix to form the mass eigenstates: the bino, neutral wino, and neutral higgsinos mix to form the neutralinos ($\tilde{\chi}^0_{1,2,3,4}$), while the charged wino and charged higgsinos mix to form charginos ($\tilde{\chi}^\pm_{1,2}$), where the subscripts denote increasing mass. The superpartners of the third-generation charged leptons ($\tau_\mathrm{L}, \tau_\mathrm{R}$) are referred to as τ-sleptons ($\tilde{\tau}_\mathrm{L}, \tilde{\tau}_\mathrm{R}$) and mix to form two mass eigenstates $\tilde{\tau}_1$ and $\tilde{\tau}_2$, where $\tilde{\tau}_1$ is the lighter of the two and is henceforth referred to as the τ-slepton ($\tilde{\tau}$). R-parity-conserving supersymmetry [39] addresses several limitations of the SM, providing a natural candidate for dark matter (DM) in the form of the lightest supersymmetric particle (LSP) [40, 41]. In SUSY scenarios with very heavy, strongly interacting superpartners, the direct production cross-section of electroweakinos and sleptons in high-energy proton-proton (pp) collisions at the Large Hadron Collider (LHC) can significantly exceed that of strongly interacting superpartners.

In scenarios where the $\tilde{\chi}^0_1$ and $\tilde{\chi}^\pm_1$ are wino-like and all other SUSY particles are decoupled, the mass difference, $\Delta m\,(\tilde{\chi}^\pm_1, \tilde{\chi}^0_1)$, is small ($\sim$100 MeV) and arises from SM radiative corrections [42, 43]. Anomaly-mediated supersymmetry-breaking (AMSB) models [44, 45] naturally predict such mass splittings and give rise to a wino-like LSP. In these scenarios, the mass-splitting between the charged wino and neutral wino is suppressed at tree level by the approximate custodial symmetry, and has been calculated at the two-loop level to be approximately 160 MeV [42], corresponding to a chargino lifetime of $\tau(\tilde{\chi}^\pm_1) \sim 0.2$ ns and a decay length of $c\tau(\tilde{\chi}^\pm_1) \sim 60$ mm. Furthermore, a number

of 'natural' SUSY models [46–48], where the $\tilde{\chi}_2^0$ is no longer decoupled, predict a light higgsino LSP with a mass near the electroweak scale. In these scenarios, the higgsino mass parameter $|\mu|$ is small compared to the other electroweakino mass parameters, which could mean higgsinos are discoverable at the LHC. While the charged and neutral higgsino states are mass degenerate at tree level, higher-order SM loop corrections generate a mass splitting of approximately 300 MeV. For chargino masses between 91 GeV and 1000 GeV, the mass splitting ranges approximately from 280 MeV to 350 MeV [49], corresponding to chargino lifetimes of $\tau(\tilde{\chi}_1^{\pm}) \sim 0.026{-}0.048$ ns ($c\tau(\tilde{\chi}_1^{\pm}) \sim 7{-}14$ mm) [43]. Due to the small mass splitting, the $\tilde{\chi}_1^{\pm}$ is assumed to decay via $\tilde{\chi}_1^{\pm} \rightarrow \pi^{\pm}\tilde{\chi}_1^0$ with a branching fraction of 100% in the wino scenarios and 95% in the higgsino scenarios [50]. The neutralino masses are set such that $m(\tilde{\chi}_2^0) = m(\tilde{\chi}_1^0)$, hence the $\tilde{\chi}_2^0$ cannot decay to the $\tilde{\chi}_1^{\pm}$ or $\tilde{\chi}_1^0$ and is treated as a stable particle that escapes the detector, similarly to the $\tilde{\chi}_1^0$.

Models featuring light τ-sleptons can yield a dark-matter relic density consistent with cosmological observations [51] and, more generally, light sleptons can participate in the co-annihilation of neutralinos [52, 53]. Long-lived τ-sleptons arise naturally in co-annihilation dark-matter models [54–56] and in gauge-mediated supersymmetry-breaking (GMSB) models [57–59]. Two simplified SUSY models are considered for τ-sleptons in this paper. The first is inspired by the Constrained Minimal Supersymmetric Standard Model (CMSSM) [60–62], where a long-lived τ-slepton can arise from a small ($\sim$2 GeV) mass-splitting between the τ-slepton and the $\tilde{\chi}_1^0$ LSP, CP-violating phases, and the mixing angle between the left- and right-handed τ-slepton states. The CMSSM-inspired scenarios are parameterised by the τ-slepton mass and lifetime, and the τ-slepton decays with 100% branching fraction as $\tilde{\tau} \rightarrow \tau\tilde{\chi}_1^0$. The second scenario is inspired by GMSB models, where a long-lived τ-slepton can arise from small couplings to its decay products. The LSP is the almost massless gravitino ($\tilde{G}$), the superpartner of a proposed

graviton. This model is parameterised by the τ-slepton mass and lifetime, and assumes a 100% branching fraction for $\tilde{\tau} \to \tau\tilde{G}$.

In all considered scenarios, the charged SUSY particle (wino, higgsino or τ-slepton) can be produced with large momentum and live long enough to traverse multiple layers of the ATLAS pixel detector before decaying. In models containing charginos, the chargino deposits energy in the innermost tracking layers before it decays and can be reconstructed as a short track if at least three layers of the tracking detector are hit. The weakly interacting LSP will escape detection and lead to missing transverse momentum ($\vec{p}_{\mathrm{T}}^{\,\mathrm{miss}}$) and the charged pion from the chargino decay has a very low momentum and is not reconstructed as a track by existing algorithms, this gives rise to the characteristic 'disappearing track' signature where the track from the chargino stops a short distance into the detector. The algorithms used to reconstruct the short tracks, referred to as tracklets, need energy deposits (hits) in at least three pixel layers. Therefore successful reconstruction requires charginos to have transverse path lengths that at least exceed the radius of the third pixel layer at ∼88.5 mm. This makes the higgsino-like scenarios considerably more challenging than the wino-like models from an experimental perspective because of the extremely short chargino lifetime predicted in the higgsino models. A similar scenario occurs in the case of τ-slepton production, where a long-lived τ-slepton particle will traverse the inner layers of the pixel detector before decaying into a τ-lepton and the LSP. The LSP escapes the detector unobserved, resulting in missing transverse momentum, and the τ-leptons evade standard reconstruction techniques, again resulting in a signature containing a disappearing track and missing transverse momentum.

In addition to the SUSY-specific wino and higgsino models studied in this paper, the disappearing-track signature is typical of a large class of DM models that predict a DM thermal relic from a massive particle with only electroweak gauge interactions [63]. The wino and higgsino models probed in this search are part of a more generic class

of models containing spin-1/2 particles transforming under SU(2) symmetry, which give rise to nearly mass-degenerate doublets ($\tilde{\chi}_1^{\pm}$, $\tilde{\chi}_1^0$) and triplets ($\tilde{\chi}_1^{\pm}$, $\tilde{\chi}_2^0$, $\tilde{\chi}_1^0$) of new particles, respectively. In both cases, the $\tilde{\chi}_1^0$ is a DM candidate, while the $\tilde{\chi}_1^{\pm}$ gives rise to the disappearing-track signature. These DM models have gained interest in the wider community as an important area of study at future colliders [64–67].

This paper targets two electroweak production processes, the production of charginos and neutralinos, and the production of τ-slepton pairs in CMSSM- and GMSB-inspired scenarios, as shown in Figure 6.2, in the context of simplified SUSY models [68–70]. In all scenarios, the charged SUSY partner is long-lived and can be reconstructed from hits in the ATLAS pixel detector. A high-momentum jet from initial-state radiation (ISR) is required in order to ensure that significant missing transverse momentum is available for event triggering.

In order to reconstruct as many charginos as possible across a wide range of lifetimes, the shortest possible track is desired. Since a helical trajectory in 3-dimensions needs at least three measurements to seed its trajectory, the minimum track length that is possible extends out to the third pixel layer (88.5 mm). This section describes the dedicated tracking configuration implemented to reconstruct tracklets with as few as three pixel hits. An efficient track extension is developed for this configuration to allow the reconstruction of longer tracks with additional pixel or SCT hits.

Previous ATLAS searches for long-lived supersymmetric charged particles searched for events with a disappearing track with at least four pixel hits [71–73]. Their results benefited from the addition of a new innermost pixel tracking layer installed during the LHC long shutdown between Run 1 and Run 2. The extra layer of pixels enabled the reconstruction of tracks shorter than those in the previous Run-1 analysis [74] and enhanced the sensitivity to shorter charged-particle lifetimes. The Run-2 ATLAS search excluded wino-like charginos with lifetimes of 0.2 ns for masses up to 460 GeV, and higgsino-like charginos with masses up to 152 GeV [71]. Searches performed by the CMS

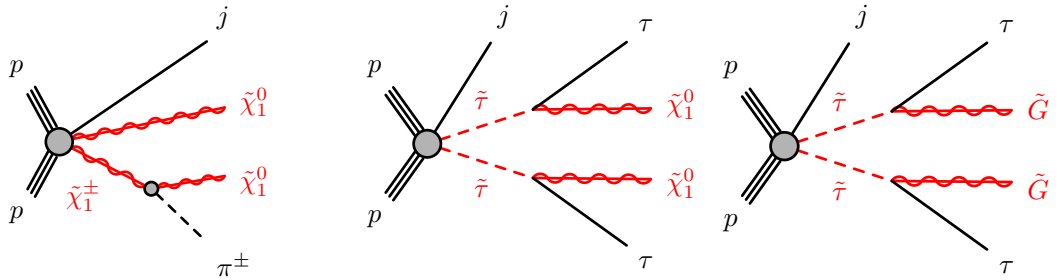


Figure 6.2. Representative signal diagrams for (a) the electroweak production of $\tilde{\chi}_1^\pm\tilde{\chi}_1^0$, and τ-slepton pair production in (b) CMSSM-inspired or (c) GMSB-inspired SUSY models. The signal signature consists of a long-lived $\tilde{\chi}_1^\pm$ or τ-slepton, missing transverse momentum, and quarks or gluons, which are observed as jets (j). When considering the electroweakino scenarios, the production of $\tilde{\chi}_1^+\tilde{\chi}_1^-$ is also considered, as is $\tilde{\chi}_1^\pm\tilde{\chi}_2^0$ specifically in the higgsino scenario.

Collaboration excluded wino-like charginos with masses below 474 GeV and a lifetime of 0.2 ns [75]. Both the ATLAS and CMS collaborations have performed searches for stable charginos and τ-sleptons using ionisation-loss or time-of-flight techniques, excluding charginos with masses smaller than 1.3 TeV for lifetimes exceeding 100 ns, and τ-sleptons with masses 200−560 GeV for lifetimes of 10 ns [76, 77].

In order to improve on these results, significant developments were made in the tracking techniques necessary for shorter lifetime scenarios. This search employs a dedicated tracking algorithm to reconstruct tracklets with as few as three pixel hits. Furthermore, to enhance sensitivity to the electroweakino production scenario, the charged pion from the decay of the $\tilde{\chi}_1^\pm$ is targeted with a specially optimised reconstruction algorithm. Due to the small mass-splitting between the $\tilde{\chi}_1^\pm$ and $\tilde{\chi}_1^0$, the charged pion has extremely low momentum, ranging from 250 to 350 MeV for the $\tilde{\chi}_1^\pm$ lifetimes considered, and typically has large impact parameters measured relative to the interaction region. In this paper, the sensitivity to charginos with wino and higgsino lifetimes motivated by SM loop corrections is significantly improved due to new analysis methods including updated signal region selection criteria, the previously

mentioned reconstruction algorithms, and improved track-quality requirements. The new track-quality criteria requires the disappearing track not to be associated with any energy deposits in the calorimeter. This significantly enhances the rejection of dominant backgrounds and accounts for two-thirds of the total improvement in the mass reach of the search in the electroweak wino-like production channel.

The paper is structured as follows: Section 6.3 introduces the ATLAS detector apparatus; Section 6.4 describes the dataset and the Monte Carlo simulation samples used; Section 6.5 discusses the object-level event reconstruction, while Section 6.6 describes the signal selection optimisation and Section 6.7 describes the background estimation techniques; Section 6.8 provides an overview of the systematic uncertainties considered, with Section 6.9 presenting the results and interpretation thereof; and finally, Section 6.10 summarises the conclusions.

6.3 ATLAS detector

The ATLAS detector [78] at the LHC covers nearly the entire solid angle around the collision point.[1] It consists of an inner tracking detector surrounded by a thin superconducting solenoid, electromagnetic and hadronic calorimeters, and a muon spectrometer incorporating three large superconducting air-core toroidal magnets.

The inner-detector system (ID) is immersed in a 2 T axial magnetic field and provides charged-particle tracking in the range $|\eta| < 2.5$. The high-granularity silicon pixel detector covers the vertex region and typically provides four measurements per track, the first hit generally being in the insertable B-layer (IBL) installed before Run 2 [79, 80]. It is followed by a silicon microstrip detector called the SemiConductor

[1] ATLAS uses a right-handed coordinate system with its origin at the nominal interaction point (IP) in the centre of the detector and the z-axis along the beam pipe. The x-axis points from the IP to the centre of the LHC ring, and the y-axis points upwards. Polar coordinates (r, ϕ) are used in the transverse plane, ϕ being the azimuthal angle around the z-axis. The pseudorapidity is defined in terms of the polar angle θ as $\eta = -\ln\tan(\theta/2)$ and is equal to the rapidity $y = (1/2)\ln[(E + p_z)/(E - p_z)]$ in the relativistic limit. Angular distance is measured in units of $\Delta R \equiv \sqrt{(\Delta y)^2 + (\Delta\phi)^2}$.

Tracker (SCT), which usually provides eight measurements per track, two per double-sided detector layer. The barrel region, $|\eta| < 1.7$, is of special interest to this analysis. Here the pixel detector comprises four layers at radii of 33.25 mm (IBL), 50.5 mm, 88.5 mm, and 122.5 mm. This is followed by the four SCT barrel layers, located at radii of 299 mm, 371 mm, 443 mm, and 514 mm. These silicon detectors are complemented by the transition radiation tracker (TRT), which enables radially extended track reconstruction up to $|\eta| = 2.0$. The TRT also provides electron identification information based on the fraction of hits (typically 30 in total) above a higher energy-deposit threshold corresponding to transition radiation.

The calorimeter system covers the pseudorapidity range $|\eta| < 4.9$. Within the region $|\eta| < 3.2$, electromagnetic calorimetry is provided by barrel and endcap high-granularity lead/liquid-argon (LAr) calorimeters, with an additional thin LAr presampler covering $|\eta| < 1.8$ to correct for energy loss in material upstream of the calorimeters. Hadronic calorimetry is provided by the steel/scintillator-tile calorimeter, segmented into three barrel structures within $|\eta| < 1.7$, and two copper/LAr hadronic endcap calorimeters. The solid angle coverage is completed with forward copper/LAr and tungsten/LAr calorimeter modules optimised for electromagnetic and hadronic energy measurements, respectively.

The muon spectrometer (MS) comprises separate trigger and high-precision tracking chambers measuring the deflection of muons in a magnetic field generated by the superconducting air-core toroidal magnets. The field integral of the toroids ranges between 2.0 and 6.0 T m across most of the detector. Three layers of precision chambers, each consisting of layers of monitored drift tubes, cover the region $|\eta| < 2.7$, complemented by cathode-strip chambers in the forward region, where the background is highest. The muon trigger system covers the range $|\eta| < 2.4$ with resistive-plate chambers in the barrel, and thin-gap chambers in the endcap regions.

The luminosity is measured mainly by the LUCID-2 detector [81], which records Cherenkov light produced in the quartz windows of photomultipliers located close to the beam pipe.

Events were selected by the first-level trigger system implemented in custom hardware, followed by selections made by algorithms implemented in software in the high-level trigger [82]. The first-level trigger accepted events from the 40 MHz bunch crossings at a rate close to 100 kHz, which the high-level trigger reduced in order to record complete events to disk at about 1.25 kHz.

A software suite [83] is used in data simulation, in the reconstruction and analysis of real and simulated data, in detector operations, and in the trigger and data acquisition systems of the experiment.

6.4 Data and simulated event samples

This search uses data from an integrated luminosity of 137 fb^{-1} of pp collisions at a centre-of-mass energy $\sqrt{s} = 13$ TeV recorded by the ATLAS experiment during Run 2 of the LHC (2015–2018). In this data-taking period, the number of interactions per bunch crossing ranged from about 8 to 70, with an average of 34 [84]. The uncertainty in the integrated luminosity is 0.83% [85], obtained using the LUCID-2 detector for the primary luminosity measurements, complemented by measurements using the ID and calorimeters. Only events recorded under stable beam conditions are used in the analysis, and general data-quality requirements ensure that all detector subsystems were operational [84]. In about 2% of Run 2 data taking the SCT experienced a significant increase in readout errors compared to standard operation. These data periods are removed as it increases the number of spuriously reconstructed pixel-only tracks which can mimic a disappearing-track signature.

The data were collected primarily with a missing transverse momentum trigger [86, 87], to target events where the sparticle system recoils against a high-p_{T} ISR jet and the undetected neutral particles lead to a large amount of missing transverse

momentum. The trigger threshold was raised as the luminosity increased during Run 2, but each threshold value provided an efficiency of >90% when requiring online a reconstructed missing transverse momentum of at least 230 GeV. Additional single-lepton ($\ell = e, \mu$) triggers are used to select regions to constrain background estimates, and these triggers operate on an efficiency plateau when applying an offline lepton transverse momentum requirement of $p_{\mathrm{T}}(\ell) > 27\,\mathrm{GeV}$ [88, 89].

Monte Carlo (MC) simulated samples are used to model SM processes and estimate the expected signal yields. All samples were produced using the ATLAS simulation infrastructure [90] and either GEANT4 [91] or a faster simulation based on a parameterisation of the calorimeter response and GEANT4 for the other detector systems. The effect of multiple interactions in the same and neighbouring bunch crossings (pile-up) was modelled by overlaying each simulated hard-scattering event with inelastic *pp* events generated with PYTHIA 8.186 [92] using the NNPDF2.3LO set of parton distribution functions (PDFs) [93] and the A3 set of tuned parameters [94]. The MC simulated samples were reweighted to match the actual distribution of the mean number of interactions per bunch crossing observed in data in 2015–2018.

The electroweakino signal samples were generated with MADGRAPH5_AMC@NLO 2.9.9 [95] at leading order (LO) and interfaced to PYTHIA 8.306 [96] for the modelling of the parton showering (PS), hadronisation and underlying event. In the wino scenarios, $\Delta m(\tilde{\chi}_1^{\pm}, \tilde{\chi}_1^0)$ is dependent upon $m(\tilde{\chi}_1^{\pm})$ and follows from the calculations in Refs. [44, 45]. In the higgsino scenarios, the mass splitting is dependent upon $m(\tilde{\chi}_1^{\pm})$ and is set according to the calculations in Ref. [50]. The CMSSM τ-slepton signals were generated with MADGRAPH5_AMC@NLO 2.9.5 at LO and interfaced to PYTHIA 8.306, while the GMSB τ-slepton signals used MADGRAPH5_AMC@NLO 2.6.1 at LO and PYTHIA 8.230.

For all signal scenarios the underlying event was modelled with the A14 [97] set of tuned parameters. The matrix element (ME) calculation was performed at tree level and includes the emission of up to two additional partons. The ME–PS merging was

done using the CKKW-L [98] prescription. The NNPDF3.0LO set of PDFs was used throughout [99]. To ensure efficient sample generation, a lifetime reweighting procedure was used, where a single signal-mass scenario and lifetime has a set of event weights allowing the signal to be reweighted to different proper lifetimes of the long-lived particle. The charginos and τ-sleptons are propagated through the detector to their decay point using the standard simulation, including magnetic field effects and electromagnetic interactions with detector material.

Signal cross-sections are calculated to next-to-leading order (NLO) in the strong coupling constant, adding the resummation of soft gluon emission at next-to-leading-logarithm (NLL) accuracy [100–108] using RESUMMINO 2.0.1. The nominal cross-section and its uncertainty are taken from an envelope of cross-section predictions using different PDF sets and factorisation and renormalisation scales, as described in Ref. [109]. For the wino and higgsino signal samples, only processes involving the direct production of a $\tilde{\chi}_1^{\pm}$ are considered in order to produce the disappearing-track signature. Therefore, the wino samples include $\tilde{\chi}_1^{+}\tilde{\chi}_1^{-}$ and $\tilde{\chi}_1^{\pm}\tilde{\chi}_1^{0}$ production, while the higgsino signal samples include $\tilde{\chi}_1^{+}\tilde{\chi}_1^{-}$, $\tilde{\chi}_1^{\pm}\tilde{\chi}_1^{0}$, and $\tilde{\chi}_1^{\pm}\tilde{\chi}_2^{0}$. Taking an example for higgsino production with $m(\tilde{\chi}_1^{\pm}) = 300\,\text{GeV}$ and $m(\tilde{\chi}_2^{0}) = m(\tilde{\chi}_1^{0}) = 299\,\text{GeV}$, the cross-section value for each of the $\tilde{\chi}_1^{\pm}\tilde{\chi}_2^{0}$ and $\tilde{\chi}_1^{\pm}\tilde{\chi}_1^{0}$ processes is 90.8 fb, while the cross-section is 53 fb for $\tilde{\chi}_1^{+}\tilde{\chi}_1^{-}$ production. For wino production with $m(\tilde{\chi}_1^{\pm}) = 300\,\text{GeV}$ and $m(\tilde{\chi}_1^{0}) = 299\,\text{GeV}$, the cross-section values are 387 fb and 190 fb for $\tilde{\chi}_1^{0}\tilde{\chi}_1^{\pm}$ and $\tilde{\chi}_1^{+}\tilde{\chi}_1^{-}$ production, respectively. Finally, the cross-section for τ-slepton pair production of $m(\tilde{\tau}) = 300\,\text{GeV}$ is 6.3 fb in both the CSSM and GMSB models.

MC simulation of V+jets events was used to study the fake-tracklet background. They were simulated with the SHERPA 2.2.1 [110] generator using NLO matrix elements for up to two partons, and LO matrix elements for up to four partons, calculated with the Comix [111] and OPENLOOPS [112–114] libraries. The matrix elements were matched with the SHERPA parton shower [115] using the MEPS@NLO prescription [116–119] and

the set of tuned parameters developed by the SHERPA authors. The NNPDF3.0NNLO set of PDFs [99] was used and the samples were normalised to a NNLO prediction [120].

To evaluate the detector response when reconstructing short tracks and to calculate the associated reconstruction efficiencies, a set of so-called 'particle gun' samples are used. These samples do not represent a specific physical event or process; instead, for each generated event the particle of interest is placed at the centre of the detector with a certain momentum and direction and can be used to investigate detector reconstruction capabilities. These samples do not include pile-up. The analysis uses three 'particle gun' samples, corresponding to electrons, muons and charged pions, generated uniformly across a transverse momentum range of $10-100\,\text{GeV}$; they are used to estimate the reconstruction efficiencies as needed for the data-driven background estimation methods employed.

6.5 Event reconstruction

The analysis uses standard ATLAS reconstruction techniques to reconstruct leptons and jets, and to calculate the missing transverse momentum, enabling the identification of potential events of interest before employing a dedicated tracklet algorithm to specifically identify events containing disappearing tracks.

Standard tracks are reconstructed in the ID within $|\eta| < 2.5$ [121] and subsequently combined to create primary vertex candidates formed from at least two tracks with $p_{\text{T}} > 500\,\text{MeV}$ [122]. Among these, the primary vertex is identified as the vertex with the largest $\sum p_{\text{T}}^2$, where the sum runs over tracks associated with the vertex. All events considered in the analysis are required to have a primary vertex. The transverse and longitudinal impact parameters of all tracks, denoted by d_0 and z_0 respectively, are calculated relative to the beamline. The z-position of the primary vertex is used to calculate the point of closest approach, which is used as the reference point to calculate z_0.

Electron candidates are reconstructed from clustered energy deposits in the electromagnetic calorimeter matched to tracks re-fitted to account for bremsstrahlung losses [123]. They are required to have $p_{\mathrm{T}} > 10\,\mathrm{GeV}$ and $|\eta| < 2.47$, and must satisfy the 'LooseAndBLayer' quality criteria [124]. In order to ensure that the trajectories of the electrons are consistent with originating from the primary vertex, the longitudinal impact parameter must satisfy $|z_0 \sin\theta| < 0.5\,\mathrm{mm}$, while the significance of the transverse impact parameter, $|d_0|/\sigma(d_0)$, must be less than 5. Electrons are required to be isolated from other objects by assessing a combination of track- and calorimeter-based information at the 'FCLoose' working point [125].

Muon candidates are reconstructed by combining ID tracks with matching MS tracks. They are required to have $p_{\mathrm{T}} > 10$ GeV and $|\eta| < 2.7$, and must satisfy the 'Medium' quality criteria [126]. Muons originating from the primary vertex are selected by requiring $|z_0 \sin\theta| < 0.5\,\mathrm{mm}$ and $|d_0|/\sigma(d_0) < 3$. The muons must satisfy isolation requirements similar to those applied to electrons, but using the 'Loose_FixedRad' working point [127]. Muons reconstructed purely from MS information are used to estimate muon backgrounds, and are referred to as stand-alone muons.

Hadronic jets are reconstructed using the anti-k_t algorithm [128] as implemented in `FastJet` [129] with a jet radius parameter $R = 0.4$. The input to this algorithm consists of particle flow (PFlow) objects [130], which combine measurements from the ID and calorimeters [131] to improve the jet energy resolution and increase the jet reconstruction efficiency, especially at low jet p_{T}. Calibrations are applied to the jet energy scale and resolution, and these include components derived from both simulation and in situ measurements [132]. The analysis uses jets within $|\eta| < 2.8$ with a calibrated $p_{\mathrm{T}} > 20\,\mathrm{GeV}$. In order to reduce contributions from jets produced in pile-up interactions, all jets with $|\eta| < 2.5$ and $p_{\mathrm{T}} < 60\,\mathrm{GeV}$ are required to satisfy the jet-to-vertex tagger (JVT) [133] 'Tight' working point requirements. The tagger is configured to identify jets from the hard-scatter vertex with 92% efficiency.

An overlap removal procedure is applied to avoid double counting of energy from different types of objects. If an electron and a jet are reconstructed within $\Delta R < 0.2$, the jet is rejected, while the electron candidate is kept. Subsequently, if an electron or muon is separated from a jet by $\Delta R < 0.4$, the electron or muon is discarded and the jet is kept.

The missing transverse momentum, with magnitude $E_{\mathrm{T}}^{\mathrm{miss}}$, is calculated as the negative vector sum of the transverse momenta of all identified hard physics objects (electrons, muons, jets), plus a contribution from an additional 'soft term'. Forward jets within $2.8 < |\eta| < 4.5$ are also included in the $E_{\mathrm{T}}^{\mathrm{miss}}$ calculation. The soft term is calculated from tracks matched to the primary vertex and not assigned to any of the hard objects [134] but does not contain the reconstructed tracklets or charged pions described in the following paragraphs.

To reconstruct the disappearing track due to a charged particle decaying after passing through the pixel detector, a dedicated tracklet reconstruction algorithm is applied after the standard reconstruction techniques described above are performed [22]. The tracking-detector hits already associated with reconstructed standard tracks are excluded from this tracklet-finding iteration. The algorithm attempts to identify tracklets having three or four hits in the pixel detector. The procedure attempts to extend the tracks into the SCT and TRT detectors and vetoes the tracklet if it can be associated with additional hits. Compared to the previous ATLAS analysis using the disappearing-track signature [71], the veto does not consider an association if more SCT hits are only found multiple layers away from the tracklet. This reduces cases where tracklets would have been vetoed due to spurious SCT hits [22] further into the detector. To improve the momentum resolution of the tracklets, they are re-fitted, adding the primary vertex as an additional constraint, and the tracklet is required to have $|d_0|/\sigma(d_0) < 1.5$ and $|z_0 \sin\theta| < 0.2\,\mathrm{mm}$. An overlap removal procedure discards tracklets within $\Delta R = 0.4$ of a jet, a lepton, or a track in the MS. Isolation requirements are also applied to the

tracklets: the scalar sum of the p_{T} of all tracks within a cone of radius $\Delta R = 0.4$ around the tracklet, $p_{\mathrm{T}}^{\mathrm{cone40}}$, must satisfy $p_{\mathrm{T}}^{\mathrm{cone40}}/p_{\mathrm{T}}^{\mathrm{tracklet}} < 0.04$ and the total transverse energy of all topological clusters within the $\Delta R = 0.4$ cone, $E_{\mathrm{T}}^{\mathrm{topoclus40}}$, must be less than 5 GeV. Tracklets are required to have $|\eta| > 0.1$, vetoing the central region where MS coverage is reduced. Figure 6.3(a) shows that the reconstruction efficiency for three- and four-layer tracklets can reach 80% depending upon the distance travelled by the chargino before decaying.

To identify low-energy charged pions, indicative of the electroweakino signal scenario, a boosted decision tree (BDT) machine-learning algorithm is used. After performing the tracklet reconstruction described above, a set of low-momentum tracks ('soft tracks') are reconstructed from the remaining hits. These low-momentum tracks are seeded from at least three SCT hits that are within $\Delta R = 0.8$ of a tracklet and are then extended using further SCT or TRT hits. A minimum of six hits, and at most two holes[2] [22], are required to reconstruct a soft track and a requirement of $p_{\mathrm{T}} > 200$ MeV is applied. As only a limited number of four-layer tracklet events have a matching soft-track that satisfies the soft-track reconstruction requirements, only events containing tracklets produced with three pixel hits are used when performing the pion reconstruction. The BDT is used to select viable charged pion candidates and to reject events with coincidental hits forming a soft track. The algorithm is trained with MC signal simulation, using soft tracks that have been 'truth-matched' at generator level to charged pions from long-lived chargino decays using a ΔR-matching criterion.

The background is taken from data, selecting tracklets that have large impact parameter values with respect to the primary vertex. From MC studies this is expected to be dominated by accidental crossings, referred to as the 'fake track' background. The algorithm uses eight input variables related to the properties of the soft tracks, including

[2]A hole is a missing hit on a reconstructed track trajectory, possibly due to a non-functioning strip which was not masked.

the kinematic properties p_{T} and η, the number of hits/holes associated with the track in the SCT, the number of hits associated with the track in the TRT, the distance in ΔR between the soft track and the tracklet, the distance in z between the soft track and the tracklet, and the χ^2 value of the soft track when fitted to the tracklet's endpoint. The TMVA architecture [135] is used with gradient boost, and a hyperparameter optimisation is performed to prevent overtraining. Figure 6.3(b) displays the BDT output score. A low-energy charged pion is identified if the score for a soft track is >0.8 and, to reduce the misidentification rate, a transverse impact parameter requirement of $|d_0|/\sigma(d_0) < 40$ is satisfied. The latter rejects an additional 4% of the tracklet background with minimal impact on the signal, according to MC simulation. Figure 6.3(c) shows that the pion reconstruction efficiency, measured as a function of the true pion p_{T} in the lab-frame, is as high as 70% for p_{T} near 2 GeV.

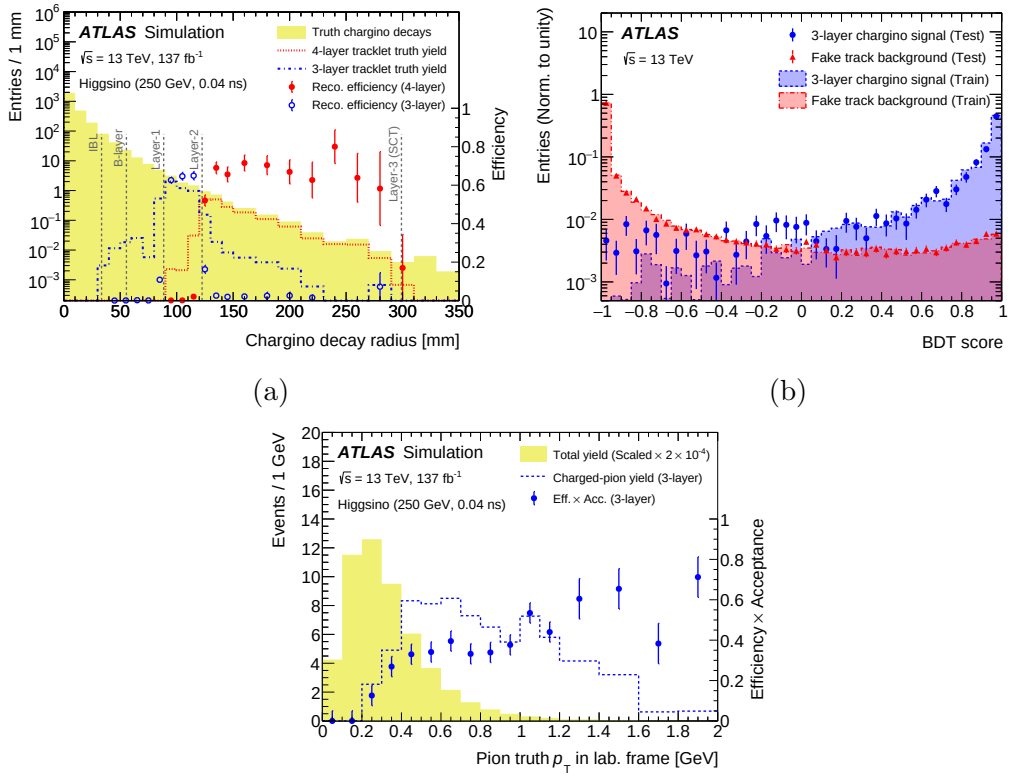


Figure 6.3. Representative distributions related to the reconstruction of tracklets and charged pions: (a) event yields and reconstruction efficiencies for three- and four-layer tracklet reconstruction as a function of $\tilde{\chi}_1^{\pm}$ decay radius; (b) BDT output score used to judge if an event contains a low-energy pion, showing the training dataset (solid histogram) and the test dataset (points); (c) event yields and reconstruction efficiency for charged pions as a function of the true pion transverse momentum as measured in the lab-frame, where the acceptance includes all charged-pion reconstruction effects but not geometric acceptance from tracklet reconstruction (which is assumed to already have been reconstructed). The true transverse momentum is defined as $p_{\mathrm{T}} = \sqrt{p_x^2 + p_y^2}$ in the global detector coordinate system with the z-axis along the beam pipe. For (a) and (c) the filled histogram displays the total yield without applying a selection, while the dashed lines present the yield after applying the tracklet selection or tracklet+pion selection. The points denote the reconstruction efficiency. A representative higgsino signal scenario with $m(\tilde{\chi}_1^{\pm}) = 250\,\mathrm{GeV}$ and $\tau(\tilde{\chi}_1^{\pm}) = 0.04\,\mathrm{ns}$ is shown.

Table 6.1. Summary of the signal region selection requirements.

Variable	SR^{4High}	SR^{4Mid}	$\text{SR}^{\text{3High1}\pi}$	$\text{SR}^{\text{3High0}\pi}$
$E_{\text{T}}^{\text{miss}}$ trigger	Passed			
Number of leptons	$= 0$			
Number of jets ($p_{\text{T}} > 20\,\text{GeV}$)	≥ 1			
Leading jet p_{T}	$> 100\,\text{GeV}$			
$\lvert\Delta\phi(j_1, \vec{p}_{\text{T}}^{\text{miss}})\rvert$	> 1.0			
Number of four-layer tracklets	≥ 1		$= 0$	
Number of three-layer tracklets	-		≥ 1	
Number of charged pions	-		≥ 1	$= 0$
Tracklet p_{T}	$> 60\,\text{GeV}$	$> 60\,\text{GeV}$	$> 60\,\text{GeV}$	$> 60\,\text{GeV}$
Tracklet $\lvert\eta\rvert$	0.1–1.9	0.1–1.9	0.1–1.9	0.1–1.7
$E_{\text{T}}^{\text{miss}}$	$> 300\,\text{GeV}$	$150-300\,\text{GeV}$	$> 240\,\text{GeV}$	$> 280\,\text{GeV}$

6.6 Analysis strategy

The signal scenarios investigated contain a tracklet, $E_{\text{T}}^{\text{miss}}$, and in the case of the chargino production scenarios a low-energy charged pion. In all considered signal scenarios, the $E_{\text{T}}^{\text{miss}}$ is however too small to satisfy the $E_{\text{T}}^{\text{miss}}$ trigger requirements. Therefore, events are required to contain a high-p_{T} initial-state radiation (ISR) jet to boost the SUSY particle system and achieve enough $E_{\text{T}}^{\text{miss}}$ to exceed the trigger threshold. Signal regions (SRs) are defined using kinematic variable selections to enhance the contribution from signal processes relative to the background processes. All SRs require events to have zero leptons, at least one jet, and a large azimuthal separation between the highest-p_{T} jet and the $\vec{p}_{\text{T}}^{\text{miss}}$, denoted by ($\lvert\Delta\phi(j_1, \vec{p}_{\text{T}}^{\text{miss}})\rvert$. Four orthogonal SRs are defined in the analysis, two requiring the presence of a tracklet reconstructed from four pixel layers, and another two requiring the presence of a tracklet reconstructed from three pixel layers and differing mainly in whether or not a low-energy charged pion is required. Table 6.1 provides a summary of all SR selections used in the analysis.

The four-hit SRs (SR^{4High} and SR^{4Mid}) require events to contain a tracklet that is reconstructed from four pixel-detector hits and has tracklet $p_{\text{T}} > 60\,\text{GeV}$. Tracklets with hits in four layers provide sensitivity to a wide range of $\tilde{\chi}^{\pm}/\tau$-slepton lifetimes, from

0.02 to 10 ns. No requirement is placed on the presence of a low-energy charged pion. $\mathrm{SR}^{\mathrm{4High}}$ requires high $E_{\mathrm{T}}^{\mathrm{miss}}$, whereas $\mathrm{SR}^{\mathrm{4Mid}}$ selects events with lower $E_{\mathrm{T}}^{\mathrm{miss}}$. The two SRs containing tracklets reconstructed from hits in three layers are defined in order to target very short-lived charged SUSY particles, which is the phase space of interest for the higgsino-like case, where $\tau(\tilde{\chi}_1^{\pm}) \sim 0.02{-}0.2\,\mathrm{ns}$. A tracklet $p_{\mathrm{T}} > 60\,\mathrm{GeV}$ requirement is applied for both three-layer tracklet SRs and the main difference between the two is the absence or presence of a low-energy charged pion. $\mathrm{SR}^{\mathrm{3High1}\pi}$ requires the presence of at least one low-energy charged pion and requires $E_{\mathrm{T}}^{\mathrm{miss}} > 240\,\mathrm{GeV}$, whereas $\mathrm{SR}^{\mathrm{3High0}\pi}$ applies a low-energy charged-pion veto and applies a slightly tighter $E_{\mathrm{T}}^{\mathrm{miss}} > 280\,\mathrm{GeV}$ selection.

In all regions, the backgrounds arise either from events containing particles that are misidentified as tracklets or from unrelated coincidental pixel-layer hits that form a tracklet. Figure 6.4 presents schematically how background events might be mis-reconstructed and satisfy the SR selections. The $\tilde{\chi}_1^{\pm}$ signal scenario is also shown, in the case where the charged pion is reconstructed from the track it leaves in the SCT detector, and in the case where the charged pion does not have enough energy to reach the SCT and leave any hits. Background events may have tracklets reconstructed from pixel hits which belong to known SM particles (electrons, muons, hadrons) or from coincidentally combined hits (referred to as the 'fake' background).

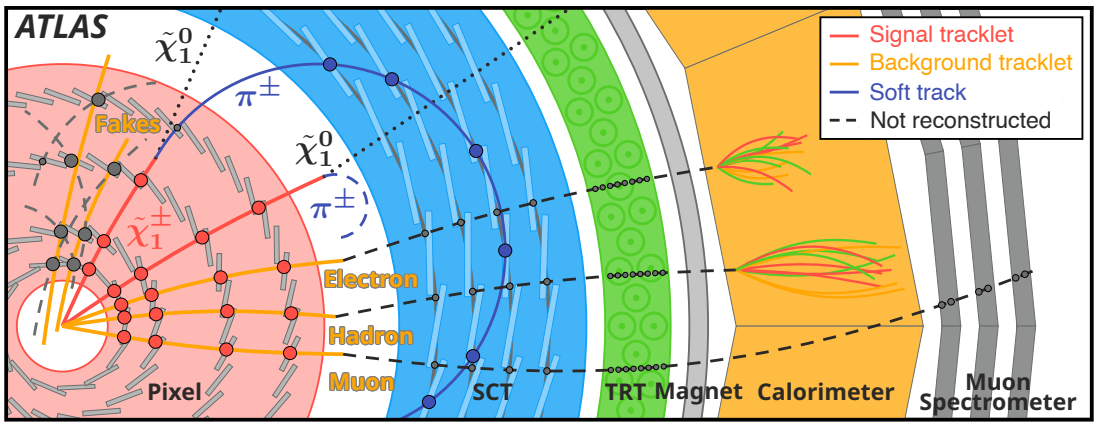


Figure 6.4. Schematic diagram illustrating how the signal scenarios are detected and how the background processes may enter the SR selections. The detector layers are not shown to scale. Taken from Ref. [71].

6.7 Background estimation

Data-driven methods are used to estimate all backgrounds in the analysis and a similar approach is used for all backgrounds sources. Template regions (TRs) are used to calculate an initial tracklet p_{T} distribution/template by selecting events containing the background under consideration. A set of alternative regions, with relaxed reconstruction selections, are used to calculate transfer factors (TFs) that are then applied to the tracklet p_{T} template to correct for the rate of electrons, muons, hadrons, and spurious signals/fakes misidentified as tracklets. This approach produces a purely data-driven estimate of the SR background from electrons and muons. However, MC simulation is used to calculate the TFs for the hadronic and fake backgrounds, so control regions (CRs) are used to normalise the tracklet p_{T} distribution and predict the expected yields in the SRs.

The electron and muon backgrounds arise due to bremsstrahlung from interactions with the inner-detector material resulting in an abrupt increase in the electron/muon track curvature. This causes the lepton to not satisfy the standard tracking requirements for lepton reconstruction and it is instead incorrectly reconstructed as a tracklet. Hadrons can also be misidentified as tracklets because of similar sudden increases in track

curvature due to bremsstrahlung or hadronic interactions in the inner-detector material, or charged hadron decays inside the inner detector. Fake tracklets can be formed with spurious pixel hits from low-p_{T} particles that do not belong to the primary interaction (pile-up), from the underlying event, or from detector noise. The methods described below are used to estimate the expected tracklet p_{T} distributions ($f_{\mathrm{SR}}^{\mathrm{bkg}}$) in each SR.

The dominant background contribution in all SRs is due to fake tracklets. From MC studies it is found that true tracklets usually exhibit a correlation between the true particle p_{T} and the tracklet p_{T}, whereas fake tracklets do not have this correlation. For each SR the p_{T} distribution of fake tracklets is estimated by

$$f_{\mathrm{SR}}^{\mathrm{fake}}(p_{\mathrm{T}}) = N^{\mathrm{TRfake}}(p_{\mathrm{T}}) \times \mathrm{TF}_{d_0\text{-correction}}^{\mathrm{fake}}(d_0) \times \mathrm{TF}_{\mathrm{hybrid}}^{\mathrm{fake}}(p_{\mathrm{T}}) \times \mathrm{SF}_{z_0}^{\mathrm{fake}} \times \mathrm{SF}_{E_{\mathrm{T}}^{\mathrm{miss}}}^{\mathrm{fake}},$$

using the yields in TRs modified by TFs and scale factors (SFs), which are described further below. In total, three tracklet p_{T} templates ($N^{\mathrm{TRfake}}(p_{\mathrm{T}})$) are extracted from three TRs (TRfake), each defined with the same selection as the SRs, but with orthogonal selections of $E_{\mathrm{T}}^{\mathrm{miss}} < 150\,\mathrm{GeV}$ and $|z_0 \sin\theta| > 2.5\,\mathrm{mm}$. Due to this inverted $E_{\mathrm{T}}^{\mathrm{miss}}$ selection, the same TRfake is used for $\mathrm{SR}^{\mathrm{4High}}$ and $\mathrm{SR}^{\mathrm{4Mid}}$. The $E_{\mathrm{T}}^{\mathrm{miss}}$ trigger can be safely used with this lower selection because the trigger efficiency does not need to be well understood in this region since it is not used to predict the overall event yield. Furthermore, because the tracklets are not included in the $E_{\mathrm{T}}^{\mathrm{miss}}$ calculation, the shape of the p_{T} distribution is independent of $E_{\mathrm{T}}^{\mathrm{miss}}$. All three TRs select tracklets reconstructed from hits in three layers to ensure a high-statistics p_{T} template. Figure 6.5(a) presents an example of the $N^{\mathrm{TRfake}}(p_{\mathrm{T}})$ distribution extracted from the TR associated with $\mathrm{SR}^{\mathrm{4High}}$ and $\mathrm{SR}^{\mathrm{4Mid}}$.

From studies using V+jets MC events, it is found that extrapolating from the high-$|z_0 \sin\theta|$ TR to regions with low $|z_0 \sin\theta|$ introduces a $|d_0|/\sigma(d_0)$ dependence. This is corrected for by using $|d_0|/\sigma(d_0)$-binned correction factors, $\mathrm{TF}_{d_0\text{-correction}}^{\mathrm{fake}}$, defined as the

ratio of the $|d_0|/\sigma(d_0)$ distribution shape for tracklets with $|z_0 \sin\theta| < 0.2\,\text{mm}$ to that for those with $|z_0 \sin\theta| > 2.5\,\text{mm}$ and are taken directly from data. Figure 6.5(b) shows the difference in $|d_0|/\sigma(d_0)$ between the TR and a low-$|z_0 \sin\theta|$ region, with the $\text{TF}^{\text{fake}}_{d_0\text{-correction}}$ shown in the lower panel.

Studies of V+jets MC events show that the fake-tracklet background has two sources: 'pure' fakes, where the tracklet is reconstructed from unrelated coincidental hits in the pixel layers, and 'hybrid' fakes, where at least one hit is not from a true hadron. In these studies it is found that at low $E_{\text{T}}^{\text{miss}}$ the dominant component comes from pure fakes, while at higher $E_{\text{T}}^{\text{miss}}$ there is a mixture of both contributions. To account for the different contributions when extrapolating from low- to high-$E_{\text{T}}^{\text{miss}}$ regions, the tracklet p_{T} template is adjusted by a p_{T}-dependent transfer factor, $\text{TF}^{\text{fake}}_{\text{hybrid}}$, derived from V+jets MC samples and calculated as the ratio of the tracklet p_{T} distributions for pure fakes and hybrid fakes. The TFs are used to scale the pure fake p_{T} distribution to the hybrid fake distribution, and the sum of the pure fakes and hybrid fakes is then used for the final tracklet p_{T} shape. Figure 6.5(c) shows the relative contributions of pure fakes and hybrid fakes from MC simulation studies, and the ratio of the two is fitted with a falling exponential-plus-constant distribution as shown in the bottom panel.

To scale the template to data, a set of regions enriched in fake tracklets are used; these select events with a low-p_{T} tracklet ($p_{\text{T}} < 35\,\text{GeV}$), low $E_{\text{T}}^{\text{miss}}$ ($E_{\text{T}}^{\text{miss}} < 150\,\text{GeV}$), and a high-$p_{\text{T}}$ 'unconstrained' tracklet ($p_{\text{T}} > 100\,\text{GeV}$), while keeping all other SR selections the same. The unconstrained tracklet is produced from the same hits as a typical tracklet, but there is no requirement to re-fit this tracklet to the primary vertex, so a significantly different p_{T} measurement can result. A set of scale factors, $\text{SF}^{\text{fake}}_{z_0}$, are calculated as the ratio of events in the fake tracklet enhanced regions to the events in the associated TRfake region but with an alternative selection of tracklet $p_{\text{T}} < 35\,\text{GeV}$ and unconstrained-tracklet $p_{\text{T}} < 100\,\text{GeV}$ ensuring orthogonality.

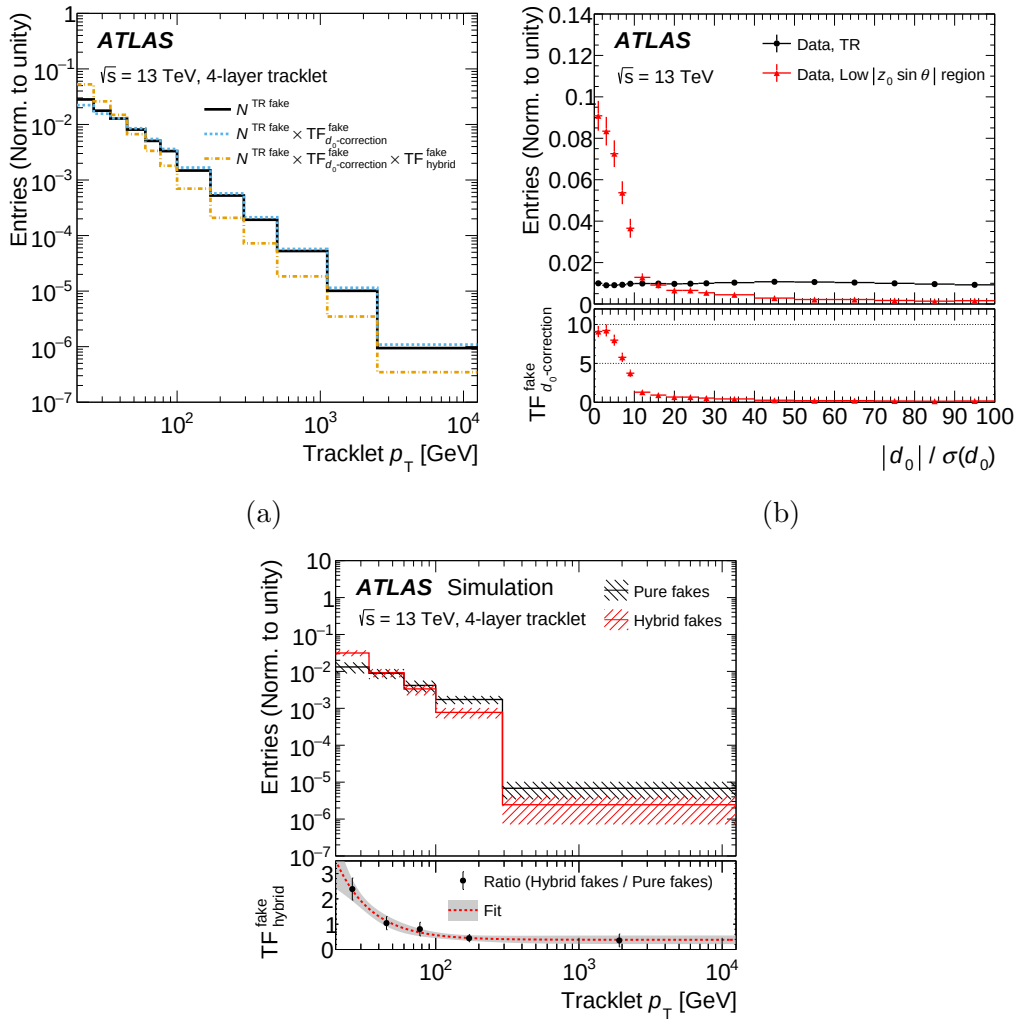


Figure 6.5. Individual components used in the estimation of the fake background: (a) shows the original template, $N^{\mathrm{TRfake}}(p_{\mathrm{T}})$, as a solid line. The templates after the application of the transfer factors are shown as dashed lines; (b) shows the $|d_0|/\sigma(d_0)$ dependence introduced when extrapolating over $|z_0 \sin\theta|$ and the binwise, with respect to $|d_0|/\sigma(d_0)$, transfer factors $\mathrm{TF}^{\mathrm{fake}}_{d_0\text{-correction}}(d_0)$ used to remove the dependence; and (c) shows a comparison between the pure fake and hybrid fake contributions and the p_{T}-dependent transfer factors $\mathrm{TF}^{\mathrm{fake}}_{\mathrm{hybrid}}(p_{\mathrm{T}})$ used to extrapolate from the template region that contains pure fakes to the SR, which contains a mixture of hybrid and pure fake components.

A final set of scale factors, $\mathrm{SF}^{\mathrm{fake}}_{E_{\mathrm{T}}^{\mathrm{miss}}}$, are used to extrapolate the template from the low-$E_{\mathrm{T}}^{\mathrm{miss}}$ region to the SRs with tighter $E_{\mathrm{T}}^{\mathrm{miss}}$ selections. The scale factors are derived

from CRs which use high values of the tracklet $|d_0|/\sigma(d_0)$ (>1.5), a loosened tracklet p_{T} selection (>20 GeV), but otherwise the same selections as the SRs. MC simulation shows the normalisation regions are >99% pure in fake tracklets, with a ratio of pure to hybrid fakes similar to that in the SRs. Table 6.2 defines the control regions $\mathrm{CR}^{\mathrm{4Low}}$ and $\mathrm{CR}^{\mathrm{4High}}$, with the ratio of events in the low-CR to the high-CR used to derive the fake background $\mathrm{SF}^{\mathrm{fake}}_{E_{\mathrm{T}}^{\mathrm{miss}}}$ in the signal regions $\mathrm{SR}^{\mathrm{4High}}$ and $\mathrm{SR}^{\mathrm{4Mid}}$. Table 6.3 defines the control regions $\mathrm{CR}^{\mathrm{3Low1}\pi}$ and $\mathrm{CR}^{\mathrm{3High1}\pi}$ used to calculate $\mathrm{SF}^{\mathrm{fake}}_{E_{\mathrm{T}}^{\mathrm{miss}}}$ for the fake background in $\mathrm{SR}^{\mathrm{3High1}\pi}$, and Table 6.4 defines $\mathrm{CR}^{\mathrm{3Low0}\pi}$ and $\mathrm{CR}^{\mathrm{3High0}\pi}$, which are used to scale this background in $\mathrm{SR}^{\mathrm{3High0}\pi}$. The remaining two CRs, $\mathrm{CR}^{\mathrm{3Mid1}\pi}$ and $\mathrm{CR}^{\mathrm{3Mid0}\pi}$, are used to calculate $\mathrm{SF}^{\mathrm{fake}}_{E_{\mathrm{T}}^{\mathrm{miss}}}$ for the validation regions, introduced later in the section.

The background from electrons reconstructed as tracklets is given by

$$f^{e}_{\mathrm{SR}}(p_{\mathrm{T}},\eta) = N^{\mathrm{TR}e}(p_{\mathrm{T}},\eta) \times \mathrm{TF}^{e}_{\mathrm{tracklet}}(p_{\mathrm{T}},\eta) \times \mathrm{TF}^{e}_{\text{calo-veto}}(p_{\mathrm{T}},\eta) \times f^{e}_{\mathrm{smear}}(p_{\mathrm{T}}),$$

which uses the yields in TRs modified by TFs and a smearing function that is described further below. Four electron-enriched TRs (TRe), with the same selections as the associated SRs but with the presence of exactly one electron instead of a tracklet, are used to extract a set of templates for the tracklet p_{T} spectrum ($N^{\mathrm{TR}e}(p_{\mathrm{T}},\eta)$). An example of the template p_{T} spectrum is presented in Figure 6.6(a) for the TRe associated with $\mathrm{SR}^{\mathrm{4High}}$. The TR$e$ events must fire the single-electron trigger, with an offline p_{T} requirement of 27 GeV. To mimic the expected $E_{\mathrm{T}}^{\mathrm{miss}}$ distribution in the SR, the electrons are removed from the $E_{\mathrm{T}}^{\mathrm{miss}}$ calculation in this region, allowing the same $E_{\mathrm{T}}^{\mathrm{miss}}$ selection as in the SR to be applied. A data-driven tag-and-probe method using $Z \to ee$ events is used to derive correction factors to estimate the likelihood that a standard electron is reconstructed as a tracklet ($\mathrm{TF}^{e}_{\mathrm{tracklet}}$) by identifying probe electrons that have a calorimeter energy cluster but no associated standard track. Figure 6.6(b) shows the p_{T} dependence of the $\mathrm{TF}^{e}_{\mathrm{tracklet}}$ distributions. A further transfer factor

($\mathrm{TF}^{e}_{\text{calo-veto}}$) is calculated, again using a data-driven tag-and-probe method in $Z \to ee$ events, to estimate the likelihood that an electron with a standard track does not have an associated calorimeter energy cluster. Figure 6.6(c) shows the p_{T} dependence of $\mathrm{TF}^{e}_{\text{calo-veto}}$ for three- and four-layer tracklets, where both TFs are calculated in bins of tracklet p_{T} and η. A transfer factor ($\mathrm{TF}^{e}_{\text{tracklet}+\pi}$) is calculated and used specifically for

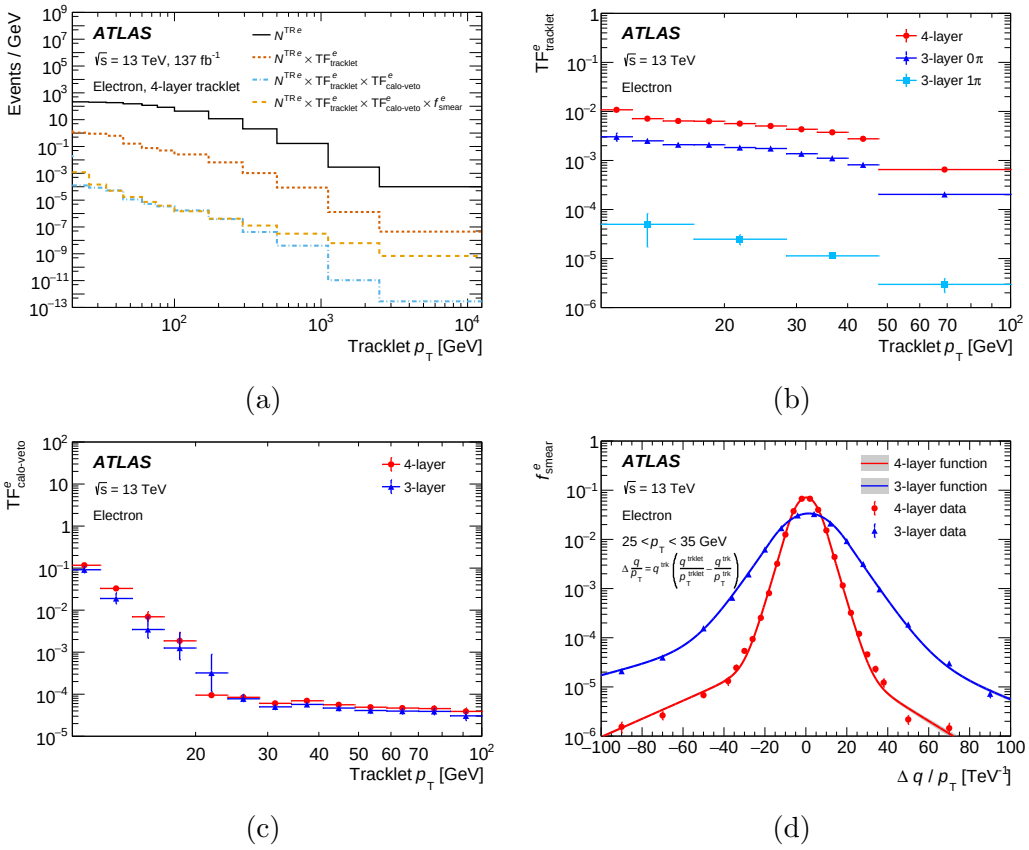


Figure 6.6. Individual contributions used in the estimation of the electron background: (a) presents the original electron p_{T} template, $N^{\mathrm{TRe}}(p_{\mathrm{T}})$, as a solid line, with the templates also shown after the application of each transfer/smearing factor as dashed lines; (b) shows the transfer factor, $\mathrm{TF}^{e}_{\text{tracklet}}$, used to correct for the likelihood of reconstructing an electron track as a tracklet; (c) shows the transfer factors, $\mathrm{TF}^{e}_{\text{calo-veto}}$, used to correct for the likelihood of an electron not being associated with a calorimeter energy cluster; and (d) shows the smearing functions, f^{e}_{smear}, used to correct the measured electron track p_{T} to the tracklet p_{T} (defined on the figure). While the tracklet p_{T} template and the TFs are dependent upon both p_{T} and η, the components are shown with their dependence upon the tracklet p_{T} distribution as a representative distribution.

the regions where the electron is associated with a low-energy charged-pion track and is used instead of $\mathrm{TF}^{e}_{\mathrm{tracklet}}$ when considering the regions requiring the presence of a pion. The application of these TFs allows the electron p_{T} template taken from the TR to be scaled in a way that takes into account the likelihood that an electron may not satisfy both of the tracking and calorimeter requirements, and thus is reconstructed as a tracklet. To account for the differences between a standard reconstructed electron track and a reconstructed tracklet, a p_{T}-dependent smearing function (f^{e}_{smear}) is applied. To calculate the smearing function, the tracklet reconstruction is applied to a standard track associated with an electron (again using $Z \to ee$ data) and the difference between the charge and p_{T} values of the standard track and tracklet are calculated. This function is fitted using a Gaussian core with exponential tails. Figure 6.6(d) shows the smearing functions used for three- and four-layer tracklets.

A similar method is used to constrain the muon backgrounds. The tracklet p_{T} distribution due to muons in a SR is calculated as

$$f^{\mu}_{\mathrm{SR}}(p_{\mathrm{T}},\eta) = N^{\mathrm{TR}\mu}(p_{\mathrm{T}},\eta) \times \mathrm{TF}^{\mu}_{\mathrm{tracklet}}(p_{\mathrm{T}},\eta) \times \mathrm{TF}^{\mu}_{\text{MS-veto}}(p_{\mathrm{T}},\eta) \times f^{\mu}_{\mathrm{smear}}(p_{\mathrm{T}}).$$

This is used in the same way as for the electron background and the individual terms are derived in a similar manner as discussed below. Four muon-enriched TRs (TRμ) are defined and the tracklet p_{T} template is taken from events passing the same selection as in the SRs but containing exactly one muon instead of a tracklet. The TRμ events must fire the single-muon trigger, with an offline p_{T} requirement of 27 GeV. As with the electrons, the expected $E^{\mathrm{miss}}_{\mathrm{T}}$ distribution in the SR is emulated by removing the muons from the $E^{\mathrm{miss}}_{\mathrm{T}}$ calculation. Correction factors to account for muons reconstructed as tracklets ($\mathrm{TF}^{\mu}_{\mathrm{tracklet}}$), and muons that do not have an associated track in the MS ($\mathrm{TF}^{\mu}_{\text{MS-veto}}$), are calculated in bins of tracklet p_{T} and η using a tag-and-probe method in $Z \to \mu\mu$ events. A transfer factor ($\mathrm{TF}^{\mu}_{\mathrm{tracklet}+\pi}$) is calculated specifically for the cases

where the muon is associated with a low-energy charged-pion track and is used instead of $\mathrm{TF}^{\mu}_{\mathrm{tracklet}}$ in the regions requiring the presence of a pion. A p_{T}-dependent smearing function (f^{μ}_{smear}) is applied to account for differences between the measured muon track p_{T} in the TR and the reconstructed tracklet p_{T}.

The final background considered in the analysis, the one due to hadronic interactions, is calculated as

$$f^{\mathrm{had}}_{\mathrm{SR}}(p_{\mathrm{T}},\eta) = N^{\mathrm{TRhad}}(p_{\mathrm{T}},\eta) \times \mathrm{TF}^{\mathrm{had}}_{\mathrm{tracklet}}(p_{\mathrm{T}},\eta) \times \mathrm{TF}^{\mathrm{had}}_{\mathrm{calo\text{-}veto}}(p_{\mathrm{T}},\eta) \times f^{\mathrm{had}}_{\mathrm{smear}}(p_{\mathrm{T}}).$$

Similarly to the other backgrounds, yields in TRs are modified by TFs and a smearing function, which is described below. Four hadronic TRs (TRhad) are defined to extract the tracklet p_{T} template ($N^{\mathrm{TRhad}}(p_{\mathrm{T}},\eta)$) by applying the same selections as the associated SR, but with changed tracklet reconstruction requirements. In the TRs the track with the highest p_{T} is required to have at least 14 hits in the TRT detector, at least five hits in the SCT, and be matched, within $\Delta R < 0.2$, to a calorimeter energy cluster with $E^{\mathrm{clus}}_{\mathrm{T}} > 3\,\mathrm{GeV}$, and $E^{\mathrm{topoclus40}}_{\mathrm{T}}/p^{\mathrm{track}}_{\mathrm{T}} > 0.5$, resulting in a pure sample of hadronic tracks. Due to the unavailability of a data-driven tag-and-probe method to calculate the transfer factors, pion and electron 'particle gun' simulation is used to estimate the probability to misidentify a hadron as a short track ($\mathrm{TF}^{\mathrm{had}}_{\mathrm{tracklet}}$) by calculating the ratio of hadron MC events reconstructed as tracklets to electron MC events reconstructed as tracklets and multiplying this by the $\mathrm{TF}^{e}_{\mathrm{tracklet}}$ value calculated from data as described above. A similar procedure is followed to calculate $\mathrm{TF}^{\mathrm{had}}_{\mathrm{tracklet}+\pi}$, which is subsequently used instead of $\mathrm{TF}^{\mathrm{had}}_{\mathrm{tracklet}}$ to calculate the SR contribution containing a low-energy pion. A transfer factor $\mathrm{TF}^{\mathrm{had}}_{\mathrm{calo\text{-}veto}}$ is applied to estimate the likelihood of reconstructing a hadron without an associated calorimeter energy cluster; it is calculated as the ratio of MC events containing a tracklet associated with a calorimeter energy cluster within $\Delta R = 0.4$ of the tracklet (when requiring $E^{\mathrm{clus}}_{\mathrm{T}} > 10\,\mathrm{GeV}$) to those without (when

Table 6.2. Summary of the event and tracklet selection requirements for the CRs associated with the four-layer SRs.

Variable	CR^{4Low}	CR^{4High}	CR^{4LowS}	CR^{4MidS}
E_T^{miss} trigger	Passed			
Number of leptons	$= 0$			
Number of jets ($p_T > 20\,GeV$)	$= 1$			
Leading jet p_T	$> 100\,GeV$			
$\lvert\Delta\phi(j_1, \vec{p}_T^{miss})\rvert$	> 1.0			
Number of four-layer tracklets	≥ 1			
Tracklet p_T	$> 20\,GeV$	$20-60\,GeV$	$> 20\,GeV$	$20-60\,GeV$
Tracklet E_T^{clus}	$< 5\,GeV$	$< 5\,GeV$	$> 5\,GeV$	$> 5\,GeV$
E_T^{miss}	$< 150\,GeV$	$> 300\,GeV$	$< 150\,GeV$	$150-300\,GeV$

requiring $E_T^{clus} < 5\,GeV$). Both TFs are dependent upon p_T and η. A p_T-dependent smearing function (f_{smear}^{had}) is applied to take into account differences between the hadronic track and the reconstructed tracklet.

After evaluating the tracklet p_T distributions for the electron, muon, hadron and fake backgrounds, they are used as the input to a binned likelihood fit (as described in Section 6.9) to provide a final estimate of the background distributions in the SRs, performing an extrapolation to higher values of E_T^{miss}. The hadronic background tracklet distributions are normalised using 'sideband' CRs: CR^{4LowS} and CR^{4MidS} (defined in Table 6.2) for the four-layer SRs, and $CR^{3Low1\pi S}$ and $CR^{3Mid1\pi S}$ (defined in Table 6.3) for both three-layer SRs, where the 'S' in the superscript denotes the sideband CR for the region. Applying this normalisation mitigates the MC dependence introduced when calculating the hadronic transfer factors. Figure 6.7 presents a schematic overview of the general background estimation strategy with the usage of CRs to normalise the hadronic background while the remaining backgrounds are taken from their templates as described above.

To evaluate the fit procedure and background modelling, orthogonal validation regions (VRs) are constructed by selecting events kinematically closer to the SR, and an extrapolation of the CR backgrounds to the VRs is performed. Five VRs are defined, as shown in Table 6.5, with reversed selections on the tracklet p_T, tracklet E_T^{clus}, or E_T^{miss} in order to remain orthogonal to both the SRs and CRs.

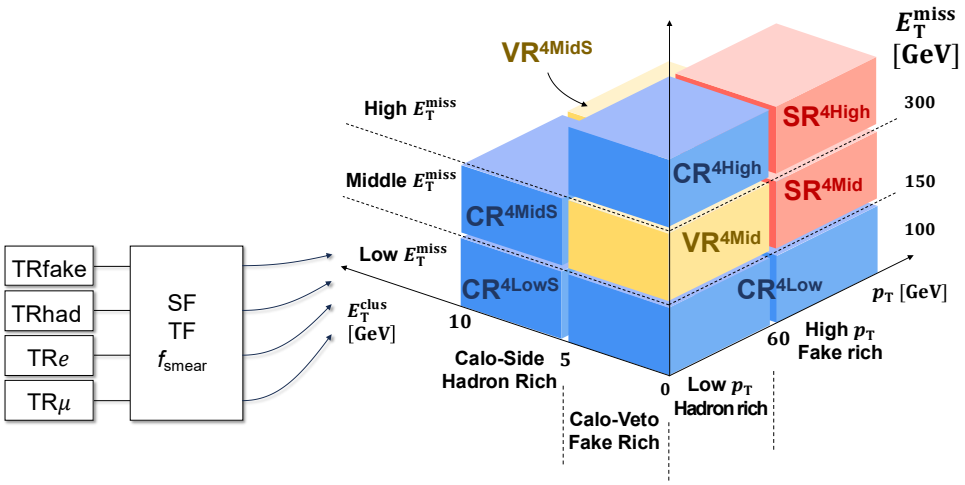


Figure 6.7. Schematic diagram for the background estimation strategy, describing the usage of template regions (TRs), and relaxed selections to calculate transfer factors (TFs) before performing the fit using control regions (CRs). The kinematic regions are orthogonal due to selections on $E_{\mathrm{T}}^{\mathrm{miss}}$, tracklet p_{T}, and tracklet $E_{\mathrm{T}}^{\mathrm{clus}}$, with high calorimeter energies ('calo-side') dominated by the hadron background, and low calorimeter energies ('calo-veto') dominated by the fake background.

Table 6.3. Summary of the event and tracklet selection requirements for the CRs associated with the three-layer SRs that contain a low-energy charged pion.

Variable	$\mathrm{CR}^{\mathrm{3Low1}\pi}$	$\mathrm{CR}^{\mathrm{3Mid1}\pi}$	$\mathrm{CR}^{\mathrm{3High1}\pi}$	$\mathrm{CR}^{\mathrm{3Low1}\pi\mathrm{S}}$	$\mathrm{CR}^{\mathrm{3Mid1}\pi\mathrm{S}}$
$E_{\mathrm{T}}^{\mathrm{miss}}$ trigger	Passed				
Number of leptons	$= 0$				
Number of jets ($p_{\mathrm{T}} > 20$ GeV)	$= 1$				
Leading jet p_{T}	> 100 GeV				
$\lvert\Delta\phi(j_1, \vec{p}_{\mathrm{T}}^{\mathrm{miss}})\rvert$	> 1.0				
Number of three-layer tracklets	≥ 1				
Number of charged pions	≥ 1				
Tracklet p_{T}	> 20 GeV	20−60 GeV	20−60 GeV	> 20 GeV	20−60 GeV
Tracklet $E_{\mathrm{T}}^{\mathrm{clus}}$	< 5 GeV	< 5 GeV	< 5 GeV	> 5 GeV	> 5 GeV
$E_{\mathrm{T}}^{\mathrm{miss}}$	< 150 GeV	150−240 GeV	> 240 GeV	< 150 GeV	150−240 GeV

Table 6.4. Summary of the event and tracklet selection requirements for the CRs associated with the three-layer SRs that veto a low-energy charged pion.

Variable	$CR^{3Low0\pi}$	$CR^{3Mid0\pi}$	$CR^{3High0\pi}$
E_T^{miss} trigger		Passed	
Number of leptons		$= 0$	
Number of jets ($p_T > 20$ GeV)		$= 1$	
Leading jet p_T		> 100 GeV	
$\lvert\Delta\phi(j_1, \vec{p}_T^{miss})\rvert$		> 1.0	
Number of three-layer tracklets		≥ 1	
Number of charged pions		$= 0$	
Tracklet p_T	> 20 GeV	20−60 GeV	20−60 GeV
Tracklet E_T^{clus}	< 5 GeV	< 5 GeV	< 5 GeV
E_T^{miss}	< 150 GeV	150−280 GeV	> 280 GeV

Table 6.5. Summary of the event and tracklet selection requirements for the validation regions.

Variable	VR^{4Mid}	VR^{4MidS}	$VR^{3Mid1\pi}$	$VR^{3Mid1\pi S}$	$VR^{3High0\pi}$
E_T^{miss} trigger			Passed		
Number of leptons			$= 0$		
Number of jets ($p_T > 20$ GeV)			$= 1$		
Leading jet p_T			> 100 GeV		
$\lvert\Delta\phi(j_1, \vec{p}_T^{miss})\rvert$			> 1.0		
Number of four-layer tracklets	≥ 1		$= 0$		
Number of three-layer tracklets	-		≥ 1		
Number of charged pions	-		≥ 1		$= 0$
Tracklet p_T	< 60 GeV	> 60 GeV	> 60 GeV	> 60 GeV	> 60 GeV
Tracklet E_T^{clus}	< 5 GeV	> 5 GeV	< 5 GeV	> 5 GeV	< 5 GeV
E_T^{miss}	150−300 GeV	150−300 GeV	150−240 GeV	150−240 GeV	> 280 GeV

6.8 Systematic uncertainties

Systematic uncertainties in the background estimates are driven by the uncertainties in the transfer factors, normalisations and shape of the tracklet p_{T} templates for the electron, muon, hadron and fake backgrounds. These uncertainties are dominated by the statistical uncertainties of the data in regions used to derive the background estimates, and are always below 10%. When calculating values of parameters which are based on data, such as the TFs and smearing functions, the statistical uncertainty of the data is used as a $\pm 1\sigma$ variation. When performing the statistical fit, the values of the transfer factors and the individual bins of each tracklet p_{T} template are allowed to vary within their statistical uncertainties. Each source of background uncertainty (p_{T} template statistical uncertainties, TFs, and smearing functions) is treated as correlated across each set of associated CRs and SRs but uncorrelated between backgrounds, except $\mathrm{TF}^{\mathrm{had}}_{\mathrm{tracklet}}$, which is correlated with $\mathrm{TF}^{e}_{\mathrm{tracklet}}$ since both TFs are used in the estimation of the hadronic background. No dedicated uncertainty is associated with the overall background estimation methodology as, within other sources of uncertainties including the statistics of the data, the predicted post-fit tracklet p_{T} distributions in the VRs are consistent with the data.

Several sources of experimental uncertainty in the SUSY signal estimates are considered. The uncertainties are included in the likelihood fit as Gaussian nuisance parameters that affect the expectation values for each SR bin. Jet energy scale and resolution uncertainties are derived as a function of the jet p_{T}, η, and flavour, using data and simulated events, as detailed in Ref. [132]. Lepton reconstruction and identification uncertainties [125, 126] are included in the fit, but are found to have negligible impact. Uncertainties in the tracklet reconstruction efficiency are estimated to be 10% due to inactive pixel modules and 6% due to selection differences between data and MC $V+$jets events. An uncertainty related to the low-energy charged pions is also applied, combining uncertainties of 10% in the reconstruction efficiency, taken from Ref. [136], and 6% in

the BDT selection efficiency, evaluated by varying the BDT input parameters by 1σ and examining the effect on the output score. All uncertainties in the final-state object reconstruction are propagated to the $E_{\mathrm{T}}^{\mathrm{miss}}$ calculation, including an additional term taking into account uncertainties in the scale and resolution of the soft term [134]. In the $\mathrm{SR}^{\mathrm{4Mid}}$ region, the $E_{\mathrm{T}}^{\mathrm{miss}}$ selection used is in the 'turn-on' region of the $E_{\mathrm{T}}^{\mathrm{miss}}$ trigger where the trigger is found to be between 85% and 90% efficient for the signal event topology. Therefore, a trigger efficiency uncertainty is also applied, as an uncertainty in the signal yield.

The theoretical uncertainties originating from the choice of factorisation and renormalisation scales for the SUSY signal samples are evaluated by varying the corresponding MC generator parameters by a factor of two around their nominal values. The uncertainties associated with the choice of PDF set [99] and the value of the strong coupling constant are also considered. Finally, five variations of the A14 tune of Pythia are used to account for ISR modelling effects due to the underlying event, jet structure, and different aspects of extra jet production. The total uncertainty from experimental sources is found to be $\sim$5% for all signal scenarios. The theoretical modelling uncertainties contribute up to 20%, increasing with increasing $\tilde{\chi}_1^{\pm}/\tau$-slepton mass, and are primarily driven by the ISR modelling uncertainty.

Figure 6.8 presents a breakdown of systematic uncertainties affecting the background estimates in the SRs, grouped by the source of the uncertainty. The total uncertainty may not simply be the sum in quadrature of the individual uncertainties, because the fit can induce correlations between the components. In all SRs, the dominant uncertainty comes from the normalisation of the fake background, and the subdominant uncertainty in most regions arises from the shape of the fake background. Due to the limited number of tracklets available for the tracklet p_{T} templates in the $\mathrm{SR}^{\mathrm{3High1}\pi}$ region, the statistical uncertainty of the template shape contributes significantly to the background uncertainty in this region.

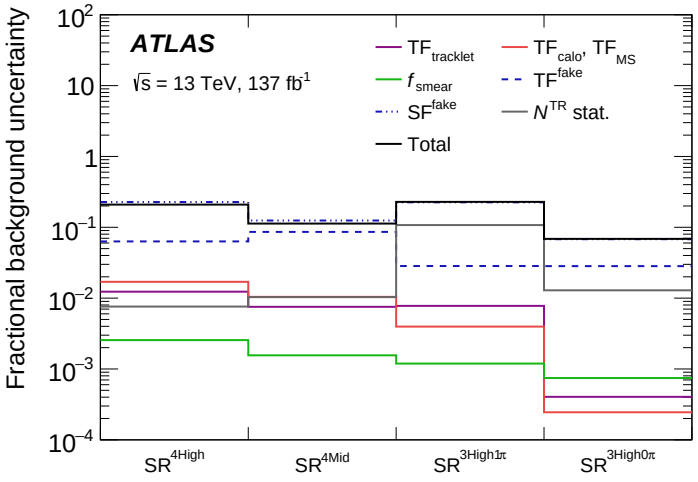


Figure 6.8. A summary of the systematic uncertainties affecting the background estimates in the SRs after the likelihood fit to data in the CRs is performed ('Post-fit'). The total uncertainty is indicated by a solid black line. The individual uncertainties may not sum in quadrature to the total uncertainty, due to correlations between the different components. The uncertainties arising from the estimation of the fake-tracklet background, which are the dominant uncertainties, are shown as blue dashed lines.

6.9 Results

Three profile likelihood fits are performed: to assess the accuracy of the SM background determination (*background-only* fit), to compute the p-value of the SM-only hypothesis (*model-independent* fit), and to evaluate the confidence level (CL) for excluding a specific new-physics hypothesis (*model-dependent* fit) [137]. Due to the low event yields in the SRs, pseudoexperiments are used for statistical interpretation of the results when performing the model-independent fit, while the asymptotic approximation [138] is used when performing the model-dependent fit.

When performing the background-only fit, the hadronic background yield is allowed to float in the CRs, resulting in a set of normalisation factors which are uncorrelated between SRs. One hadronic normalistion factor is calculated for each SR and is propagated as a general scaling factor to the SR's tracklet p_{T} distribution. Only

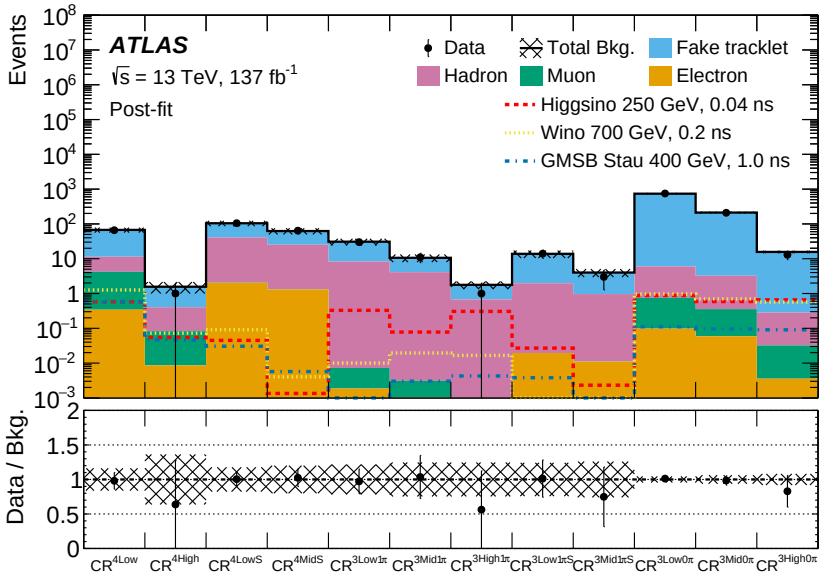


Figure 6.9. The post-fit yields in the CRs. All statistical and systematic uncertainties are considered in the error bands. Three representative pre-fit signal yields are indicated with dashed lines.

the CRs, and not the SRs, are used to constrain the SM background. The electron, muon and fake-tracklet background yields are allowed to vary within their uncertainties when the fit is performed, but no overall normalisation is derived for these backgrounds.

Figure 6.9 presents an overview of the CRs after the background-only fit. The CRs that are used to normalise the hadronic backgrounds have, by design, a ratio of data to background event yield of one, whereas the other CRs that are used to derive the tracklet p_{T} distribution for the fake background are not normalised and the data–MC difference is applied as the $\mathrm{SF}^{\mathrm{fake}}_{E_{\mathrm{T}}^{\mathrm{miss}}}$ value from the fake-background estimation procedure before performing the fit.

To evaluate the fit procedure and background modelling, the CR normalisations are extrapolated to the VRs and the results are compared with data and validated before performing the same extrapolation to the SRs. Good agreement is seen between the data and prediction when examining the modelling of the tracklet p_{T} shape in three of the

VRs as shown in Figure 6.10. The tracklet p_{T} distribution differs between the electron and muon backgrounds because an electron is more likely to undergo bremsstrahlung than a muon.

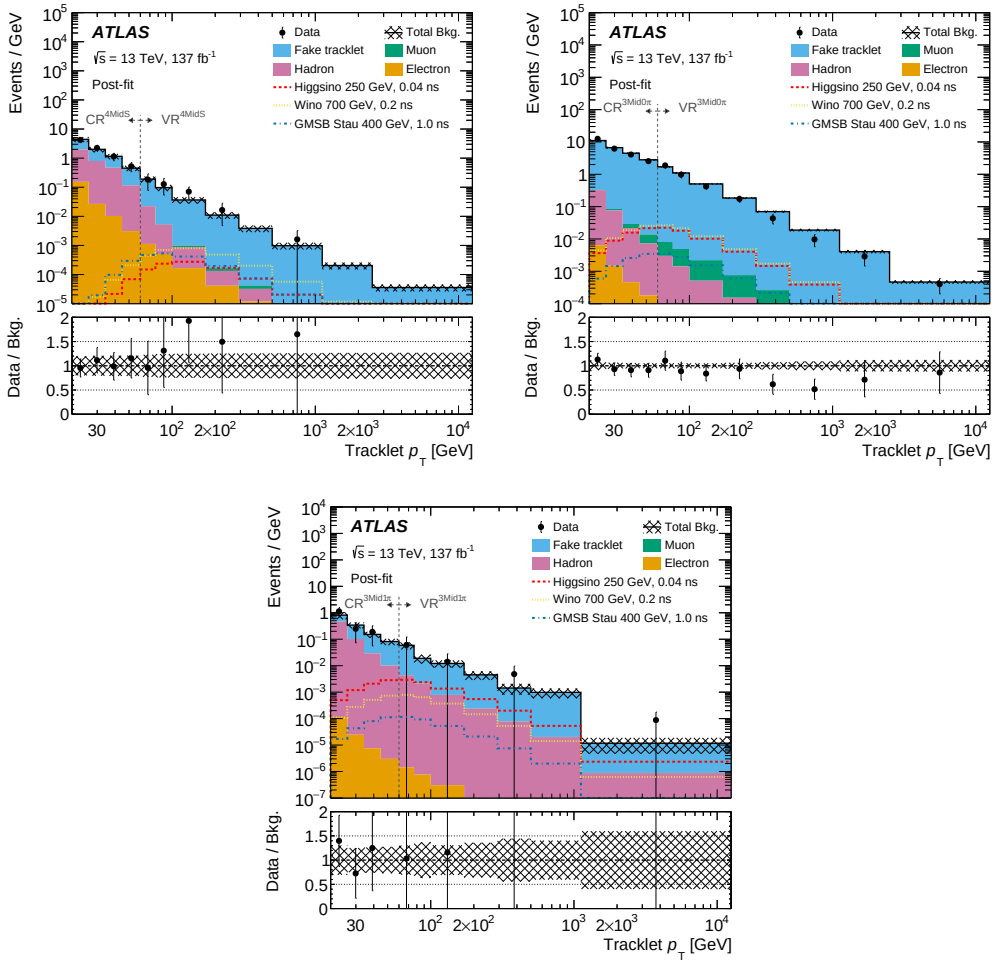


Figure 6.10. The post-fit tracklet p_{T} distributions in () $\mathrm{VR}^{\mathrm{4MidS}}$, () $\mathrm{VR}^{\mathrm{3High0}\pi}$, and () $\mathrm{VR}^{\mathrm{3Mid1}\pi}$. The dashed vertical line denotes the boundary between the CR and VR selections. The pre-fit signal distributions are indicated with dashed lines. The lower pad shows the ratio of the observed yields to the post-fit predicted background yields. The last bin includes overflow events. All statistical and systematic uncertainties are considered in the error bands.

The level of post-fit agreement in the VRs and SRs is shown in Figure 6.11, which also shows the statistical significance [139] of the observed data yields and the

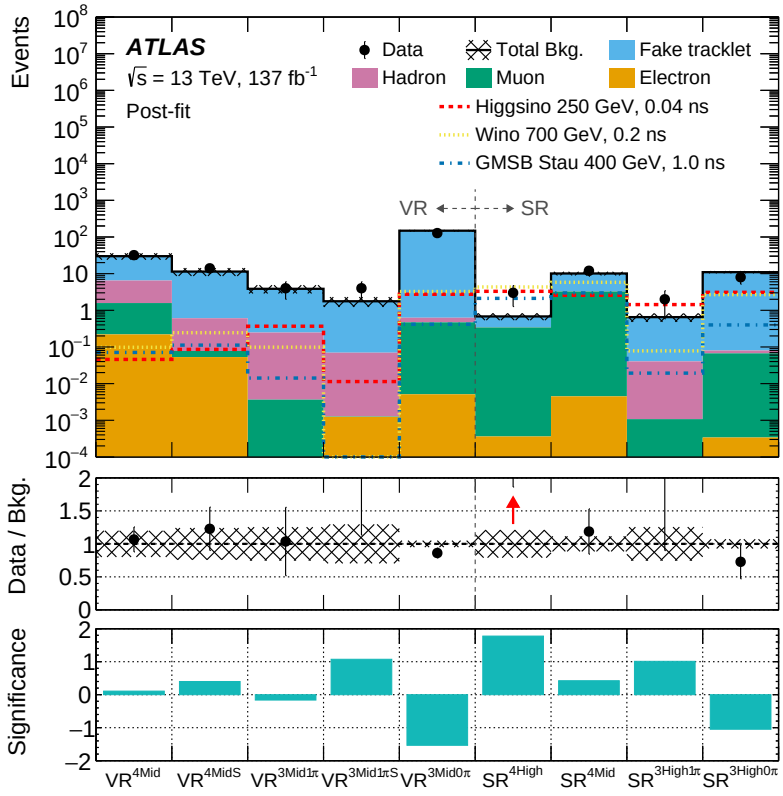


Figure 6.11. The observed and expected event yields in the VRs and SRs. The lower pads show the ratio of the observed yields to the post-fit predicted background yields and the statistical significance [139] of the observed data. A red arrow is used to indicate that a ratio value is outside the displayed interval. The background estimates are calculated from the background-only fit. All statistical and systematic uncertainties are considered in the error bands. Three representative pre-fit signal yields are indicated with dashed lines.

background prediction in each of the regions. Good agreement is seen in the VRs. Small excesses are seen in $\mathrm{SR}^{4\mathrm{High}}$ and $\mathrm{SR}^{3\mathrm{High}1\pi}$, corresponding to local significances of 1.9σ and 1.0σ respectively. These discrepancies and how the events compare with the previous analysis are discussed further at the end of this section.

Figure 6.12 presents post-fit distributions of the tracklet p_{T} in each SR. In the regions where a relatively high number of background events are expected ($\mathrm{SR}^{4\mathrm{Mid}}$ and $\mathrm{SR}^{3\mathrm{High}0\pi}$), the data are in good agreement with the background estimates, with the distributions agreeing within uncertainties. Due to the small number of events in $\mathrm{SR}^{4\mathrm{High}}$

and $\mathrm{SR}^{\mathrm{3High1}\pi}$, less can be discerned from the level of agreement of the tracklet p_{T} distributions. Figure 6.12(a) shows the presence of three data events in a single $\mathrm{SR}^{\mathrm{4High}}$ bin, corresponding to tracklet p_{T} values of 139 GeV, 142 GeV and 152 GeV.

Table 6.6 shows the observed and expected yields in the SRs, as well as the model-independent fit results in each SR. The model-independent fit uses the same CRs as the background-only fit. A single-bin SR is also included in the fit by summing the individual tracklet-p_{T} bins in a given region. The hadronic background is then allowed to float in the CRs and the single-bin SR. This method uses a profile-likelihood-ratio test statistic [138], where a generic new-physics signal of intensity μ_{sig} is assumed to contribute exclusively to each individual, single-bin SR, and is used to assess the p-value of the background-only hypothesis (corresponding to $\mu_{\mathrm{sig}} = 0$) and to extract S^{95}_{exp} and S^{95}_{obs}, i.e. the expected and observed 95% CL limits on the number of signal events in the SR, using the $\mathrm{CL_s}$ prescription [140]. The S^{95}_{obs} limit is also converted to a limit on the visible cross-section $\sigma^{95}_{\mathrm{obs}}$ by dividing by the total integrated luminosity.

Table 6.6. Summary of the observed and post-fit expected SR yields, with 'Bkg.' denoting background, and the model-independent fit results. All systematic and statistical uncertainties are considered. The calculated p_0-value is capped at 0.5 and shown together with the corresponding significance in standard deviations (Z).

	$\mathrm{SR}^{\mathrm{4High}}$	$\mathrm{SR}^{\mathrm{4Mid}}$	$\mathrm{SR}^{\mathrm{3High1}\pi}$	$\mathrm{SR}^{\mathrm{3High0}\pi}$
Fake Bkg.	0.33 ± 0.14	6.8 ± 1.1	0.62 ± 0.16	10.9 ± 0.8
Hadron Bkg.	$(5 \pm 4) \times 10^{-4}$	$(7 \pm 7) \times 10^{-3}$	0.029 ± 0.014	0.011 ± 0.021
Electron Bkg.	$(3.7 \pm 2.1) \times 10^{-4}$	$(4.6 \pm 2.7) \times 10^{-3}$	$(10 \pm 9) \times 10^{-6}$	$(2.5 \pm 1.3) \times 10^{-4}$
Muon Bkg.	0.342 ± 0.015	3.28 ± 0.14	$(1.1 \pm 0.6) \times 10^{-3}$	0.068 ± 0.009
Total Bkg.	0.68 ± 0.14	10.1 ± 1.1	0.65 ± 0.16	11.0 ± 0.8
Observed	3	12	2	8
p_0 (Z)	0.033 (1.9)	0.26 (0.6)	0.14 (1.1)	0.5 (0)
S^{95}_{exp}	$3.7^{+0.8}_{-0.6}$	$12.3^{+3.6}_{-2.9}$	$3.2^{+1.0}_{-0.2}$	$8.3^{+2.8}_{-2.6}$
S^{95}_{obs}	6.0	12.4	5.0	5.8
$\sigma^{95}_{\mathrm{obs}}$ [fb]	0.044	0.090	0.037	0.043

In the absence of a significant excess in the observed data, 95% CL exclusion limits are placed on the SUSY signal scenarios by statistically combining all SRs, binned in tracklet p_{T}, which provides greater sensitivity than simply considering only one SR at a time. The binning is chosen such that the low tracklet-p_{T} bins retain sufficient granularity to ensure fit stability and signal sensitivity, with wider bins used as tracklet p_{T} increases, reflecting the poorer tracklet p_{T} resolution and limited discrimination power of the highest bins. A model-dependent fit is used, where each signal scenario is introduced and a fit to the tracklet p_{T} distribution is performed, with CRs and SRs used to normalise the hadronic background and determine the signal strength for a specific signal model. The four-layer regions dominate the sensitivity, and although the expected sensitivity in the SUSY models is significantly better than in the previous analysis [71], by around 100 GeV in SUSY particle masses, the small excess in $\mathrm{SR}^{\mathrm{4High}}$ weakens the observed exclusion limit.

The model-dependent limits for wino pair production are shown in Figure 6.13, where wino-like charginos with lifetimes of 1 ns and masses up to 1020 GeV are expected to be excluded. The small excess observed in the signal regions results in a weaker observed mass exclusion limit of 880 GeV. Figure 6.14 shows the model-dependent limits for higgsino pair production, where in the long-lifetime region of $\sim$1 ns, the sensitivity extends up to masses of 720 GeV (840 GeV expected). Figures 6.13 and 6.14 also show the exclusion sensitivities when converting the chargino lifetime to the mass-splitting between the electroweakinos and when comparing it with the theoretical expectation for mass splitting in wino- or higgsino-like scenarios. In the wino-like case, charginos are excluded for masses up to 670 GeV (770 GeV expected), while in the higgsino-like case, charginos are excluded for masses up to 225 GeV (250 GeV expected), improving upon previous results by 15 GeV. Compared to the previous analysis, this search is able to exclude smaller values of the signal cross-section. For example, when considering a higgsino signal scenario of $m(\tilde{\chi}_1^{\pm}) = 300$ GeV and $\tau(\tilde{\chi}_1^{\pm}) = 0.05$ ns the signal cross-section

exclusion limit is a factor of 2.5 times lower than the previous result. When considering $m(\tilde{\chi}_1^{\pm}) = 500\,\text{GeV}$ and $\tau(\tilde{\chi}_1^{\pm}) = 0.1\,\text{ns}$ the signal cross-section exclusion limit is a factor of 1.8 lower than in the previous analysis.

The 95% CL exclusion limits in the τ-slepton scenarios are presented in Figure 6.15. Due to the small cross-section for $\tilde{\tau}\tilde{\tau}$ production, the signal yield is too low in the three-layer SRs to offer sensitivity, so only the four-layer SRs and associated CRs are used in the model-dependent fit. The sensitivity in CMSSM- and GMSB-inspired scenarios is comparable, with τ-sleptons excluded for masses up to around 320 GeV and 300 GeV (390 GeV and 380 GeV expected), respectively, for a mass difference of $\sim$2 GeV between the τ-slepton and $\tilde{\chi}_1^0/\tilde{G}$ (corresponding to τ-slepton lifetimes of $\sim$1 ns).

Due to changes in the analysis strategy since the previous analysis in Ref. [71], particularly in the reconstruction of the tracklets, a direct comparison of the SRs is non-trivial, as the previous analyses used five-layer tracking and did not use the additional SCT data quality veto. Despite this, it is found that one of the events selected by SR^{4High} was also one of the three events selected by the previous analysis. The two new events in SR^{4High} are selected because of improvements in track reconstruction. The two events selected by $\text{SR}^{\text{3High1}\pi}$ are likely to stem from a hadronic interaction in the ID material as a secondary vertex is reconstructed in a region with known material. The resulting kink in the particle path results in a reconstructed tracklet rather than a standard track. A 'material veto' was considered in the analysis design to avoid such events, but was not adopted as it had a highly detrimental impact on the signal acceptance.

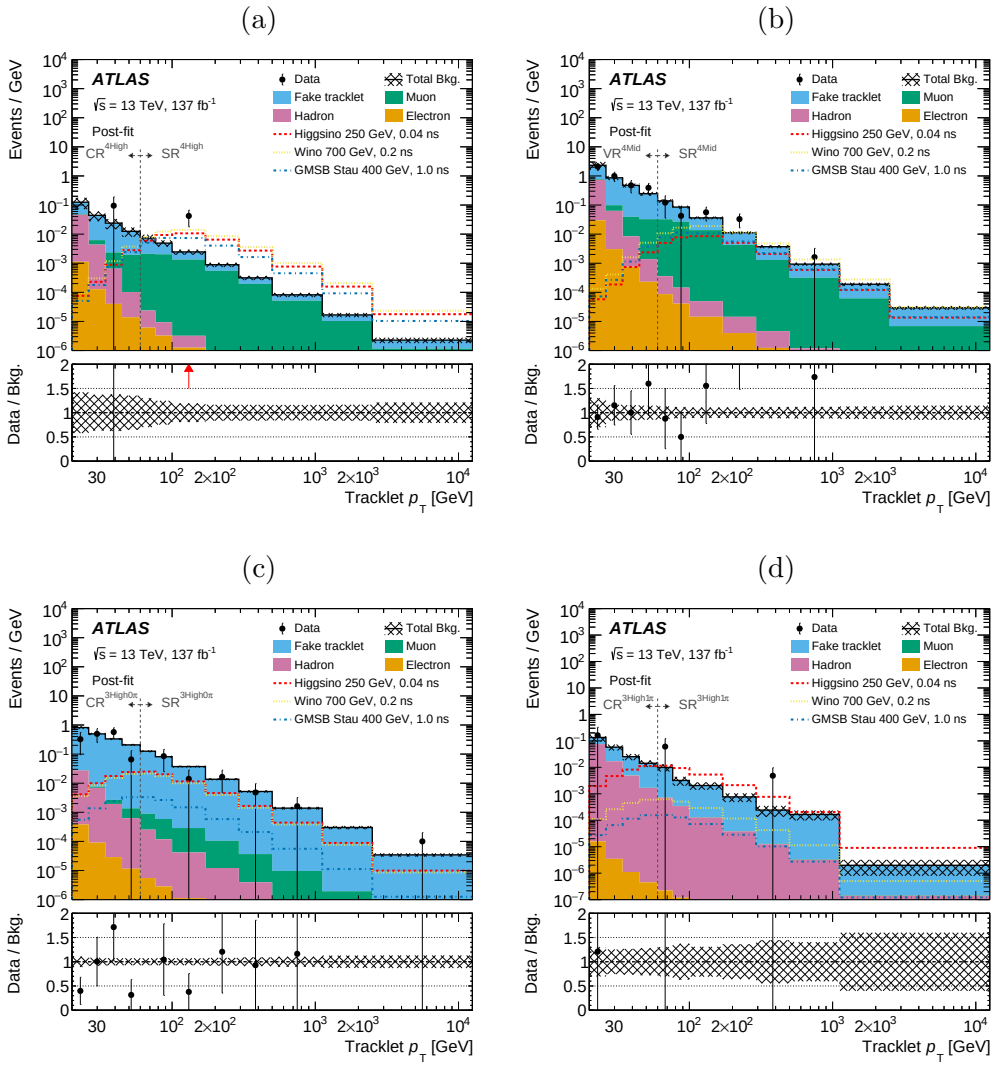


Figure 6.12. The post-fit tracklet p_{T} distributions in (a) $\mathrm{SR}^{\mathrm{4High}}$, (b) $\mathrm{SR}^{\mathrm{4Mid}}$, (c) $\mathrm{SR}^{\mathrm{3High0}\pi}$, and (d) $\mathrm{SR}^{\mathrm{3High1}\pi}$. The dashed vertical line denotes the boundary between the CR/VR and SR selections. The lower pad shows the ratio of the observed data yields to the post-fit predicted background estimates. A red arrow is used to indicate that a ratio value is outside the displayed interval. The last bin includes overflow events. All statistical and systematic uncertainties are considered in the error bands. Three representative pre-fit signal yields are indicated with dashed lines.

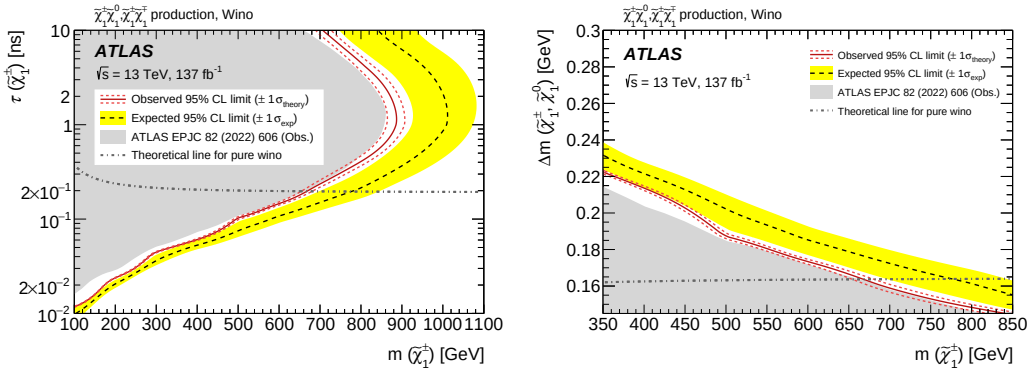


Figure 6.13. The expected (dashed line) and observed (solid line) 95% CL exclusion contours for wino production as a function of the chargino mass and () lifetime, or () mass splitting of the electroweakinos. The dotted lines indicates the $\pm\sigma_{\text{theory}}$ from signal cross-section uncertainties, while the solid band indicates the $\pm\sigma_{\text{exp}}$ from experimental systematic uncertainties and statistical uncertainties on the data yields. The solid grey area shows the region excluded by Ref. [71]. The dashed-dotted line is the prediction of the chargino lifetime or wino mass splitting as a function of the chargino mass as predicted by the SM loop corrections [42].

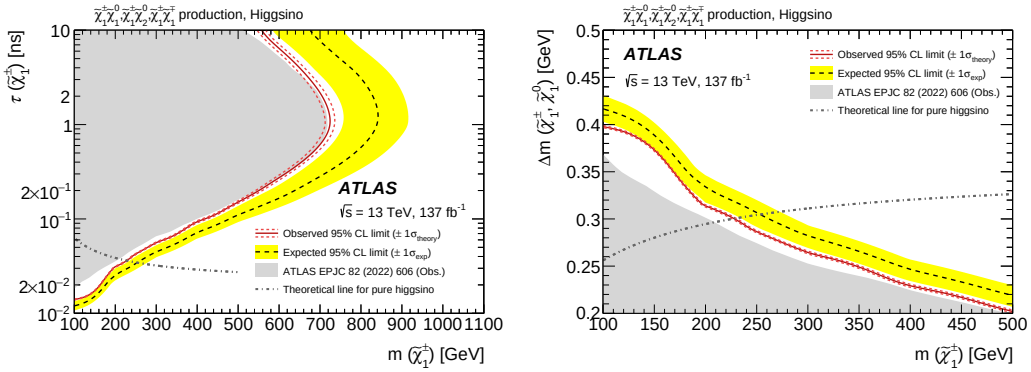


Figure 6.14. The expected (dashed line) and observed (solid line) 95% CL exclusion contours for higgsino production as a function of the chargino mass and () lifetime, or () mass splitting of the electroweakinos. The dotted lines indicates the $\pm\sigma_{\text{theory}}$ from signal cross-section uncertainties, while the solid band indicates the $\pm\sigma_{\text{exp}}$ from experimental systematic uncertainties and statistical uncertainties on the data yields. The solid grey area shows the region excluded by Ref. [71]. The dashed-dotted line is the prediction of the chargino lifetime or higgsino mass splitting as a function of the chargino mass as predicted by the SM loop corrections [49].

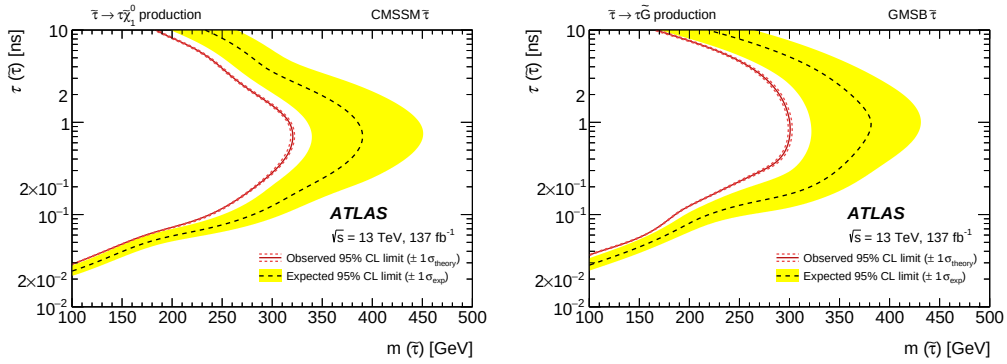


Figure 6.15. The expected (dashed line) and observed (solid line) 95% CL exclusion contours for τ-slepton production in () CMSSM-inspired scenarios and () GMSB-inspired scenario. The dotted lines indicates the $\pm\sigma_{\text{theory}}$ from signal cross-section uncertainties, while the solid band indicates the $\pm\sigma_{\text{exp}}$ from experimental systematic uncertainties and statistical uncertainties on the data yields.

6.10 Conclusion

A search for new physics in final states containing a disappearing track and $E_{\mathrm{T}}^{\mathrm{miss}}$, indicative of a heavy charged particle decaying after traversing only the innermost layers of the ATLAS detector, has been performed using $137\,\mathrm{fb}^{-1}$ of data from $\sqrt{s} = 13\,\mathrm{TeV}$ pp collisions at the LHC. Two BSM scenarios are considered, the first being electroweakino pair production with at least one chargino, where $\tilde{\chi}_1^{\pm} \to \pi^{\pm}\tilde{\chi}_1^0$. The second set of scenarios considered are those of τ-slepton pair production: a CMSSM-inspired scenario where the τ-slepton decays as $\tilde{\tau} \to \tau\tilde{\chi}_1^0$, and a GMSB-inspired scenario where it decays as $\tilde{\tau} \to \tau\tilde{G}$. The analysis uses four signal regions for a final state with zero leptons, one jet, high $E_{\mathrm{T}}^{\mathrm{miss}}$, and a tracklet. Improvements in the analysis techniques, including the reconstruction of tracklets from hits in only three pixel layers and a dedicated BDT to reconstruct low-energy pions, increased the sensitivity compared to the previous Run-2 analysis. Data-driven methods are used to estimate the backgrounds, which arise when a stable particle is incorrectly reconstructed as a tracklet or when random combinations of inner-detector hits are incorrectly identified as a tracklet.

The data obervations agree with the SM expectation to within 2σ. The results are interpreted in simplified SUSY models. For higgsino production, chargino masses of up to 225 GeV (250 GeV) are observed (expected) to be excluded at 95% CL in the lifetime regime $\tau < 0.03\,\mathrm{ns}$ where the electroweakino mass splitting is motivated by loop corrections due to SM bosons. These are currently the strongest exclusion limits in this region of phase space. For longer lifetimes up to 1 ns, exclusion limits of up to 720 GeV (840 GeV) are set. For wino production, charginos with masses of up to 880 GeV (1020 GeV) are excluded for lifetimes of around 1 ns. In CMSSM- and GMSB-inspired τ-slepton production scenarios, the observed (expected) τ-slepton mass exclusion limits reach 320 GeV (390 GeV) and 300 GeV (380 GeV) respectively, in the case of τ-slepton lifetimes of around 1 ns.

CHAPTER VII

DISAPPEARING TRACKS WITH HIGH IONIZATION ENERGY LOSS

7.1 Analysis Introduction

This analysis searches for heavy long-lived charged particles using disappearing track signatures characterized by high ionization energy loss ($\mathrm{d}E/\mathrm{d}x$). Such signatures are predicted in several BSM theories, including GMSB and AMSB SUSY as discussed in Sec. 2.3.1 and 2.3.2. In these scenarios, long-lived particles arise naturally due to small mass splittings or weak couplings. Given the current limits on SUSY [141], low mass, 200 GeV and lower, SUSY particles are largely excluded, motivating the search for heavier particles.

A disappearing track is a reconstructed pixel track that hits at least the first four pixel layers of the Inner Detector but doesn't hit the required number of silicon layers to be reconstructed as a track. These tracks are associated with three physical phenomena: the decay of a particle, scattering of a particle, or uncorrelated hits that are reconstructed as a track. These short tracks, called tracklets, provide a unique experimental signature not common from standard model particles.

There are three sources of background in the disappearing track searches, fakes, hadronic scattering, and leptonic scattering. These three sources of background nominally have low $\mathrm{d}E/\mathrm{d}x$; however, due to the statistical nature of ionization energy loss can have large $\mathrm{d}E/\mathrm{d}x$.

7.2 Data

Full run 2 and partial run 3 data is used in this search. The data is from pp collisions at a center of mass energy for run 2 of $\sqrt{s} = 13\text{TeV}$ and for run 3 of $\sqrt{s} = 13.6\text{TeV}$. The total integrated luminosity used for this search is about $300\,\text{fb}^{-1}$.

The datasets used were produced using a non-standard reconstruction chain. This analysis requires information not retained in standard DAODs and is typically only available in the RAW data, such as pixel cluster charge, size and shape; normally, these

values are dropped to reduce the size of the AOD files and reduce computation time. Dropping cluster information is a reasonable choice for ATLAS as a whole as cluster level information is not needed in the vast majority of physics analyses, not even among the long-lived particle searches. To retain these non-standard variables in the DAOD, event picking was used to select the data. Event picking is a method for selecting specific events to be reconstructed in a non-standard reconstruction chain, allowing great flexibility in choosing what information is saved.

Event picking relies on the EventIndex system designed for direct selection and retrieval of individual events. By retrieving only the required subset of the full dataset, the number of files that must be staged from tape is significantly reduced, decreasing the total reprocessing time. Event picking consists of three main steps.

7.2.0.1 Event selection. A subset of the total dataset to be reconstructed must be identified. This is done by analyzing the standard DAOD files produced in the nominal reconstruction chain to determine which events are relevant for the analysis. The selected events include those in the signal region, validation regions, control regions, and additional events required for dedicated studies. Once the events are identified, their corresponding run and event numbers are extracted.

The event selections used for event picking are defined in Sec. 7.4.1.

7.2.0.2 Event retrieval. The selected event and run numbers, together with any needed metadata (E.G. trigger stream information or run years), are provided to the event picking service. The event picking service queries the EventIndex and retrieves the corresponding RAW events. These events are then collected into containers that can be managed via rucio and stored in group storage.

7.2.0.3 Event reconstruction. The selected RAW events are reconstructed using a dedicated reconstruction designed to preserve information that is normally not saved during the reconstruction stage. These DAODs are then

compared to the datasets from the nominal reconstruction chain to check for issues in the reconstruction and to ensure that all selected events are present in the DAODs.

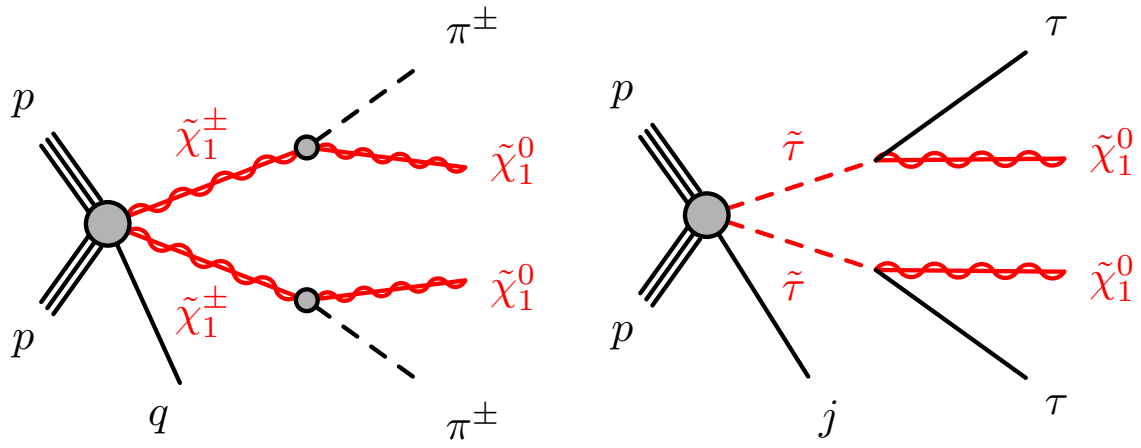
7.3 Simulation

The Monte Carlo (MC) samples used probe a largely unexplored region of parameter space in searches for physics BSM. The targeted phase space corresponds to heavy particles with masses of $\mathcal{O}$(100–1000 GeV) and lifetimes of $\mathcal{O}$(0.1–10 ns). This search targets the direct detection of long-lived charged particles and is therefore designed to be as model-agnostic as reasonably possible, allowing future reinterpretations of other BSM models more straight forward. The benchmark models considered are motivated by SUSY, which naturally provides mechanisms for long-lived particles. In particular, the analysis focuses on GMSB stau scenarios and AMSB wino scenarios.

7.3.1 Wino. For the wino benchmark, the SUSY scenario considered is AMSB. In this framework, the lightest neutralino is typically the LSP, while the chargino (wino-like) is the NLSP, as shown in Fig. 7.1(a). The small mass splitting between the chargino and the neutralino leads to a suppressed phase space for the chargino decay, resulting in a long lifetime.

The wino samples are generated using a simplified AMSB inspired model in which only the masses and lifetimes of the charginos and neutralinos are varied to determine the kinematics. This approach assumes that the slepton masses are sufficiently large to be neglected. The simplified model has been validated against full AMSB simulations and shows good agreement. Although the branching ratio of the chargino must be set manually in this framework, the simplified setup significantly streamlines the generation of samples.

The wino samples were generated using MadGraph5_aMC@NLO v3.5.1 interfaced with Pythia 8.308 and EvtGen v2.1.1. The A14 tune with the NNPDF23LO PDF set was used.



(a) (b)

Figure 7.1. Feynman diagrams for (left) pair-produced charginos and (right) pair-produced staus.

7.3.2 Stau. The stau benchmark is based on a GMSB scenario. In this case, the gravitino is the LSP and nearly massless. The stau is the NLSP and decays to a tau lepton and a gravitino, as shown in Fig. 7.1(b). Due to the very small coupling to the gravitino, the stau can acquire a long lifetime.

The stau samples were generated using MadGraph5_aMC@NLO v3.3.1 interfaced with Pythia 8.308 and EvtGen v2.1.1. The A14 tune with the NNPDF23LO PDF set was used.

7.4 Signal Region and Selections

To achieve optimal sensitivity across a range of signal models and mass scales, this analysis defines four signal regions, grouped into two categories: decay-agnostic and decay-specific. The decay-agnostic regions are designed to remain largely independent of the underlying decay mode, focusing instead on the identification of disappearing tracks with high ionization energy loss. These regions are further subdivided into two categories targeting high mass and low mass particles, respectively. In contrast, the decay-specific regions explicitly target particular decay signatures. One region selects events containing a kinked tracklet, indicative of a decay, while the other applies a veto on such kinks to

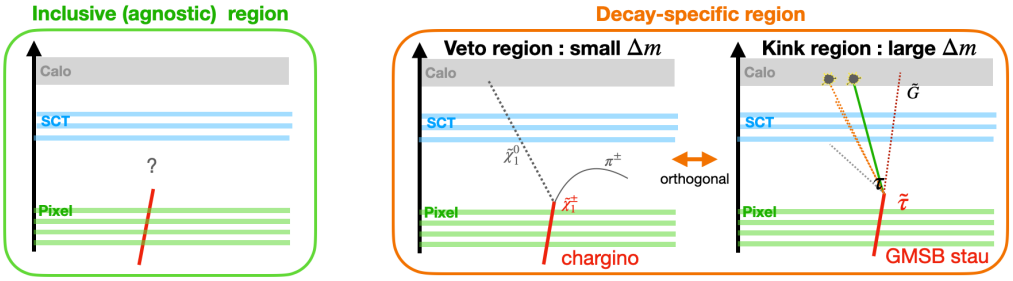


Figure 7.2. Schematic view of the signal regions. On the left being for decay-agnostic signal regions. On the right being for decay-specific regions. Note that in this case the Δm is specifically the mass splitting between the BSM particle and the sum of decay products. Credit: Yoshifumi Narukawa.

target models with soft decay products that cannot be reconstructed. Together, these signal regions provide broad and complementary sensitivity to multiple models while enabling more robust future reinterpretations of the results. A schematic overview of the regions is shown in Fig. 7.2.

7.4.1 Event Picking. To further exploit the discriminating power of ionization energy loss, it is necessary to incorporate cluster level information in the event reconstruction. This additional granularity improves the performance of $\mathrm{d}E/\mathrm{d}x$-based selections, motivating the need for event picking strategy.

As described in Sec. 7.2, not all events can be reconstructed with the full cluster information. Therefore, an event picking procedure is applied. To efficiently utilize this procedure, a set of preliminary selections is defined with the goal of retaining approximately 10^6 events. These selected events include signal, validation, and control regions.

The selection strategy proceeds in stages. First, poorly reconstructed tracklets are removed using quality criteria. Subsequently, requirements on MET, p_T, and track based isolation are applied to suppress background contributions while retaining signal efficiency.

A key aspect of this strategy is that certain potentially powerful background rejection selections are intentionally not applied at this stage. Instead, they are reserved to define dedicated validation and control regions, ensuring robust background modeling and cross-checks. The full set of selections is summarized in Tab. 7.1.

The variables MET, p_T, and track based isolation are found to provide the most effective discrimination between signal and background while maintaining high signal acceptance. The impact of the MET, p_T, and track-based isolation requirements on both signal efficiency and background rejection were evaluated, results can be seen in Fig. 7.3.

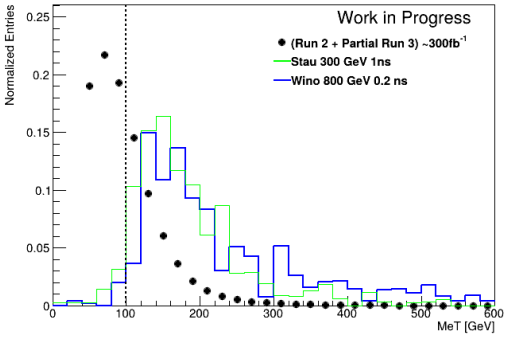
7.4.1.1 Tracklet Momentum. It is observed that p_T exhibits a rapidly falling distribution for background, whereas the signal exhibits a broad, smeared peak at higher p_T, with a strong suppression of events at low p_T. Motivating the selections shown in Fig. 7.3

7.4.1.2 Event Missing Transverse Energy. MET is used for removing a significant number of background events. The MET requirement is observed to alter the relative composition of background processes. At MET $< 100\,\text{GeV}$ QCD contributions begin to dominate the events selected, thus necessitating a MET $> 100\,\text{GeV}$ for all studies. In addition, the chosen MET threshold preserves a low MET validation region for background estimation and is therefore lower than the expected optimal value for background rejection and signal acceptance. The final MET selection is further optimized within each signal region using cluster level selections. The distributions of MET for signal and background are shown in Fig. 7.3.

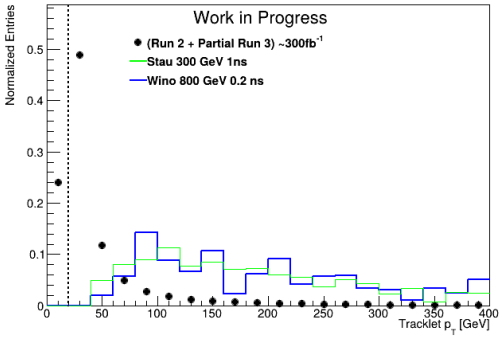
7.4.1.3 Track Isolation. The last major selection used to remove background is track level isolation. The track level isolation is found to remove hadronic decays and jets efficiently without removing signal. This can be seen in Fig. 7.3.

The full cutflow for event picking can be seen in Fig. 7.4

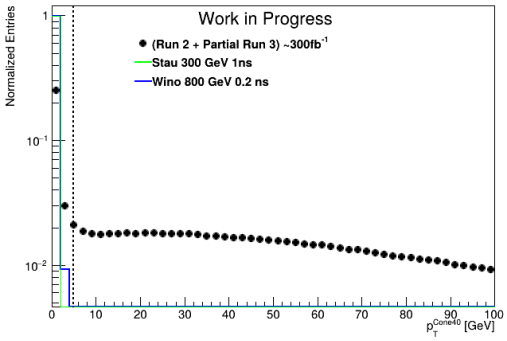
7.4.2 Baseline Tracklet Selections. In addition to the selections for event picking baseline selections were defined and are listed in Tab. 7.2



(a) MET distribution



(b) p_T distribution



(c) Tracklet based isolation distribution

Figure 7.3. Distributions of the key selection variables for signal and background processes, with $\mathrm{d}E/\mathrm{d}x <$ 1.2 to avoid signal region. (a) MET distribution, (b) p_T, (c) ptcone40 Clear separation between signal and background is observed, motivating the chosen selection thresholds at the dashed lines shown.

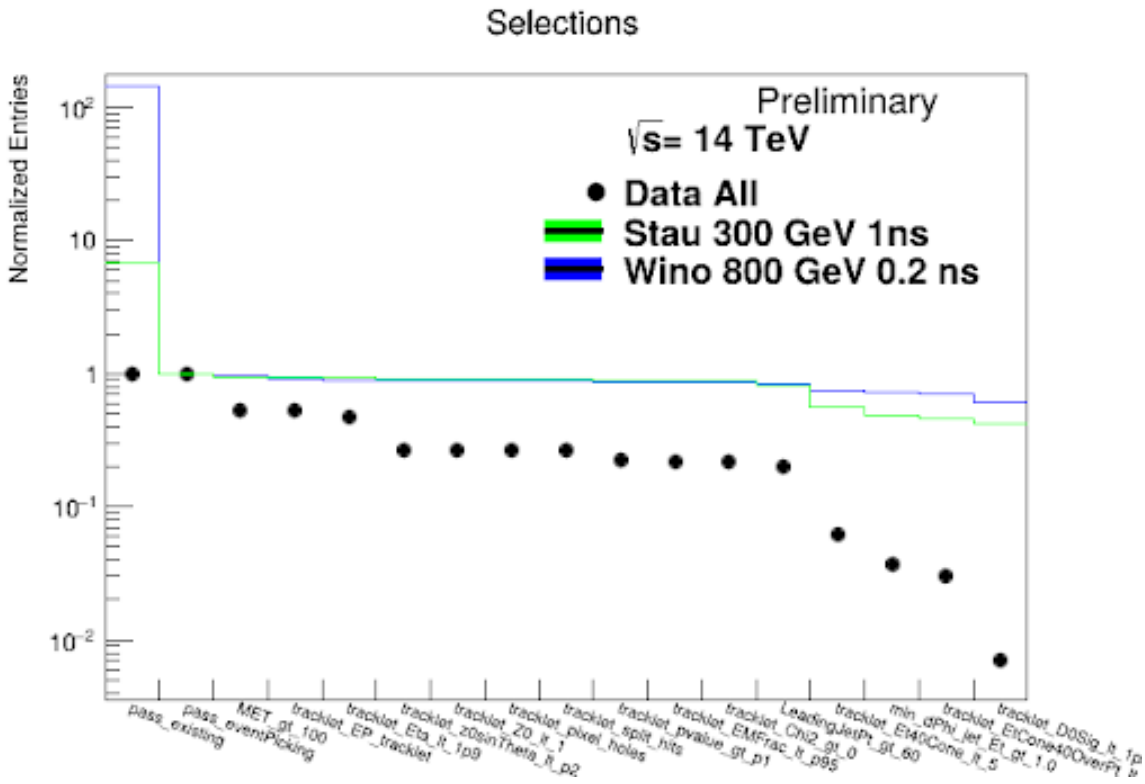


Figure 7.4. Final signal cutflow for event picking selections.

Table 7.1. Event Picking Selections applied to run 2 and partial run 3 dataset.

Event Level Selections

Item	Description
Event Cleaning	Cleans poor quality events with low quality objects
GRL pass	Require run to be in good run list (GRL)
No Bad LLP Jets	Place quality cuts on jets in event
Trigger	Lowest unprescaled E_T^{miss} trigger.
Offline Missing E_t	$MET > 100$ GeV
Disappearing track	Must have a tracklet that satisfies the following requirements.

Tracklet Level Selections

Item	Description
Four Layer Tracklet	Tracklet must have hit all four barrel pixel layers
Tracklet Momentum	$p_T >$ 20 GeV
No Ganged Flag	Tracklet quality selection
No Spoiled Hits	Tracklet quality selection
No Outliers Hits	Tracklet quality selection
NumberdE/dx measurements	Two or more pixel hits used for dE/dx measurement
ptCone 40	Track Isolation p_T Cone40 < 5 GeV

7.4.3 Signal Regions: inclusive Regions. The inclusive signal regions are split into two regions, high-mass and low-mass. In addition to the baseline selections the high mass inclusive signal region only has an additional requirement on dE/dx and p_T. Similar to the high-mass inclusive signal region the low-mass inclusive region uses all the baseline selections with an additional requirement on dE/dx and p_T. This choice was motivated by the relationship between dE/dx and mass shown in Eq. 5.23.

The selections are summarized in Tab. 7.3

7.4.4 Signal Regions: kinked tracklet. The kinked tracklet requirement and veto are based on targeting the specific decay modes of various models. The kinked tracklet definition and description can be found in Sec. 5.1.4

7.4.4.1 Kinked veto. The kinked veto region is meant to target models with small mass splitting between the long-lived particle and decay products, such as in

Table 7.2. The baseline tracklet selections used for all signal regions, applied in addition to baseline selections.

Baseline Selections

Item	Description
MET	MET > 120GeV
Relative Tracklet Isolation	LLP $Pt_{cone40}/p_T < 0.04$
Longitudinal Impact Parameter Significance	$\sigma_{d_0} < 1.5$
Nearest Vertex Impact Parameter	$z_0 < 0.2$ mm
P Value	$p < 0.1$
Pseudorapidity	$\eta < 1.9$
Tracklet Momentum	$p_T >$ 20 GeV (Note non vertex constrained see Sec. 5.1.3)

Table 7.3. Signal region selections. Note these are in addition to the baseline selections defined in 7.4.2

(a) Additional selections used for high-mass signal region selections.

Inclusive Signal Region high-mass

Item	Description
Tracklet Momentum	$p_T > 60$ GeV
Ionization Energy Loss	$\mathrm{d}E/\mathrm{d}x > 1.6$

(b) Additional selections used for low-mass signal region selections.

Inclusive Signal Region low-mass

Item	Description
Tracklet Momentum	$p_T > 60$ GeV
Ionization Energy Loss	$\mathrm{d}E/\mathrm{d}x > 1.4$

Table 7.4. Kinked Veto event selections.

Kinked Veto Event Selections

Item	Description
Event Picking Selections	Pass event picking selections (Sec. 7.4.1)
Baseline Selections	Pass baseline selections (Sec. 7.4.2)
TightBadJet Veto	
Lepton Veto	nElectrons = 0 and nMuons = 0
ISR requirement	Leading jet $p_T > 60$ GeV
Jet kinematics	min $d\phi$ (jet, MET)> 1.0
Offline $E_{\mathrm{T}}^{\mathrm{miss}}$	$E_{\mathrm{T}}^{\mathrm{miss}} > 100$ GeV
Tracklet Pass	At least one tracklet that passes
the tracklet requirements in Tab. 7.5	

Table 7.5. Additional selections used for low-mass signal region selections.

Kinked Veto Tracklet Requirements

Cluster level quality cut	
Momentum	$p_{\mathrm{T}} > 20$ GeV and vertex-constrained $p_{\mathrm{T}} > 100$ GeV
Impact parameters	$\lvert d_0/\sigma_{d_0}\rvert < 1.5$ and $\mathrm{DZ}_{\mathrm{nearestvertex}} < 0.2$ mm
	and $\lvert z_0 \sin\theta\rvert < 0.2$ mm
Pseudorapidity	$0.1 < \lvert\eta\rvert < 1.9$
Calorimeter Veto	$E_{\mathrm{T}}^{\mathrm{topoclus40}} < 5$ GeV
Jet isolation	$\Delta R(\text{tracklet}, \text{jet}^{\mathrm{p_T}>50\,\mathrm{GeV}}) > 0.4$
Muon isolation	$\Delta R(\text{tracklet}, \text{MStrack}^{\mathrm{p_T}>10\,\mathrm{GeV}}) > 0.4$
Kink veto	$\neg\left(110 < r < 400 \text{ mm},\ \text{perigee} < 1.5 \text{ mm},\ p_T^{\mathrm{LRT}} > 10 \text{ GeV}\right)$
Tracklet Momentum	$p_T > 60$ GeV
Ionization Energy Loss	$\mathrm{d}E/\mathrm{d}x > 1.4$

the AMSB Wino case. In these models the small mass splitting is expected to result in soft particles that are not reconstructed.

The kinked tracklet region selections are defined in Tab. 7.4 and 7.5.

7.4.4.2 Kinked tracklet requirement. The kinked required region targets models with a large mass splitting between the long-lived particle and the decay products, as in models like the GMSB stau. With the large mass splitting one of the decay particles, which must carry charge due to charge conservation, leaves a track that can be reconstructed. These tracks would originate from the end of the tracklet

motivating the selection in the kinked tracklet region. The selections for the kinked tracklet can be seen in Tab. 7.5

This idea is new to ATLAS; however, kinked tracks has historical precedence in LEP where, due to the energies involved and models targeted, it was a typical long-lived particle signature.

Table 7.6. Event selections for the kink-required SR, which targets large mass-splitting signals like the GMSB stau. A kinked tracklet is required as a unique probe for these signal events. Since significant background rejection is achieved from the kink and the $\mathrm{d}E/\mathrm{d}x$ requirement, the $E_{\mathrm{T}}^{\mathrm{miss}}$ and vertex-constrained p_{T} thresholds are loosened to 100 GeV and 40 GeV, respectively, to maximize signal acceptance.

Item	**Description**
passEP	
pass Baseline Selection	
Offline $E_{\mathrm{T}}^{\mathrm{miss}}$	$E_{\mathrm{T}}^{\mathrm{miss}} > 100$ GeV

Table 7.7. Tracklet selections for the kink-required SR, which targets large mass-splitting signals like the GMSB stau. A kinked tracklet is required as a unique probe for these signal events. Since significant background rejection is achieved from the kink and the $\mathrm{d}E/\mathrm{d}x$ requirement, the $E_{\mathrm{T}}^{\mathrm{miss}}$ and vertex-constrained p_{T} thresholds are loosened to 100 GeV and 40 GeV, respectively, to maximize signal acceptance.

Category	**Item**
Cluster level quality cut	
Momentum	$p_{\mathrm{T}} > 20$ GeV and vertex-constrained $p_{\mathrm{T}} > 40$ GeV
Calorimeter Veto	$E_{\mathrm{T}}^{\mathrm{topoclus40}} < 5$ GeV
Kink veto	$\big(110 < r < 400$ mm, perigee < 1.5 mm, $p_T^{\mathrm{LRT}} > 10$ GeV$\big)$

7.5 Background Estimation

For this search there are two primary sources of backgrounds, fakes and scattering backgrounds.

Fakes are mis-combinations of hits from multiple real low-momentum particles that are reconstructed as a single high-momentum tracklet. These fake tracklets can

exhibit high ionization energy loss as the underlying particles interacting with the sensors can be low-momentum and therefore can have a large ionization energy loss. Fake tracklets are a challenging background as they originate from mis-combinations of particles and are therefore heavily influenced by pileup conditions and detector performance. As a result it is difficult to reliably model the abundance using Monte Carlo simulation.

The scattering background originates from real high-energy electrons, muons, or hadrons that undergo material interactions, or more rarely decay, such that they produce a tracklet signature. Although these particles are typically minimum ionizing at the relevant energies, the statistical nature of ionization energy loss, as well as occasional overlaps with other particles, can cause them to appear as highly ionizing. Consequently, the scattering background is strongly influenced by the detector material and detector conditions, making accurate modeling in Monte Carlo simulation challenging.

For this analysis, two background estimation methods have been developed in parallel. Due to the challenging conditions that lead to the background sources in this analysis both techniques are fully data driven. The first technique developed is a ABCD method relying on p_T and $\mathrm{d}E/\mathrm{d}x$. The second technique is a two component $\mathrm{d}E/\mathrm{d}x$ shape fit. Both methods have been developed together and use the same baseline selections described in Sec. 7.4.2 This approach allows different estimation strategies to be tested and validated against each other. Additionally, the two component $\mathrm{d}E/\mathrm{d}x$ shape fit requires large number of statistics in the SR while the ABCD method retains sensitivity with much lower number of statistics regions.

7.5.1 ABCD Method in $\mathrm{d}E/\mathrm{d}x$ and p_T. For the ABCD background estimates p_T and $\mathrm{d}E/\mathrm{d}x$ are used to define four different regions. The signal regions and three control regions are constructed using simple threshold selections in p_T and $\mathrm{d}E/\mathrm{d}x$. The expected background yield in the signal region is predicted from the control regions

according to Eq. 7.1. This estimation assumes that p_T and $\mathrm{d}E/\mathrm{d}x$ are uncorrelated.

$$N_A = \frac{N_B \cdot N_C}{N_D} \tag{7.1}$$

To validate the assumption that the background $\mathrm{d}E/\mathrm{d}x$ distribution is independent of p_T, the correlation between these two variables is studied. This correlation is evaluated in a low-MET control region; the low-MET control region has the same selections as baseline except, $80\,\mathrm{GeV} < \mathrm{MET} < 100\,\mathrm{GeV}$. The low-MET control region is expected to be dominated by background processes.

Two complementary approaches are used to test this assumption. First, the $\mathrm{d}E/\mathrm{d}x$ distributions are directly compared across different p_T bins to examine whether the overall shape varies with transverse momentum. Second, the data are divided into p_T slices and the fraction of events in the high-$\mathrm{d}E/\mathrm{d}x$ tail is evaluated in each bin. Since relatively few events populate the high-$\mathrm{d}E/\mathrm{d}x$ region, non-uniform binning is used to ensure sufficient statistical precision across the full range.

The results of these studies are shown in Fig. 7.5 and Fig. 7.6. The tail fractions are observed to be consistent with a flat distribution across p_T bins within statistical uncertainties, indicating that the Landau tail does not exhibit significant momentum dependence. Similarly, the $\mathrm{d}E/\mathrm{d}x$ distributions remain stable across the full p_T range. These results support the assumption that the background $\mathrm{d}E/\mathrm{d}x$ distribution is effectively independent of p_T, validating its use in the background estimation procedure.

The background estimation is validated in several independent regions designed to test closure and correlation with different background compositions:

- A low-p_T region between 20 and 60 GeV
- a minimum-ionizing region
- a fake enriched region
- a low-E_T^{miss} region between 100 and 120 GeV

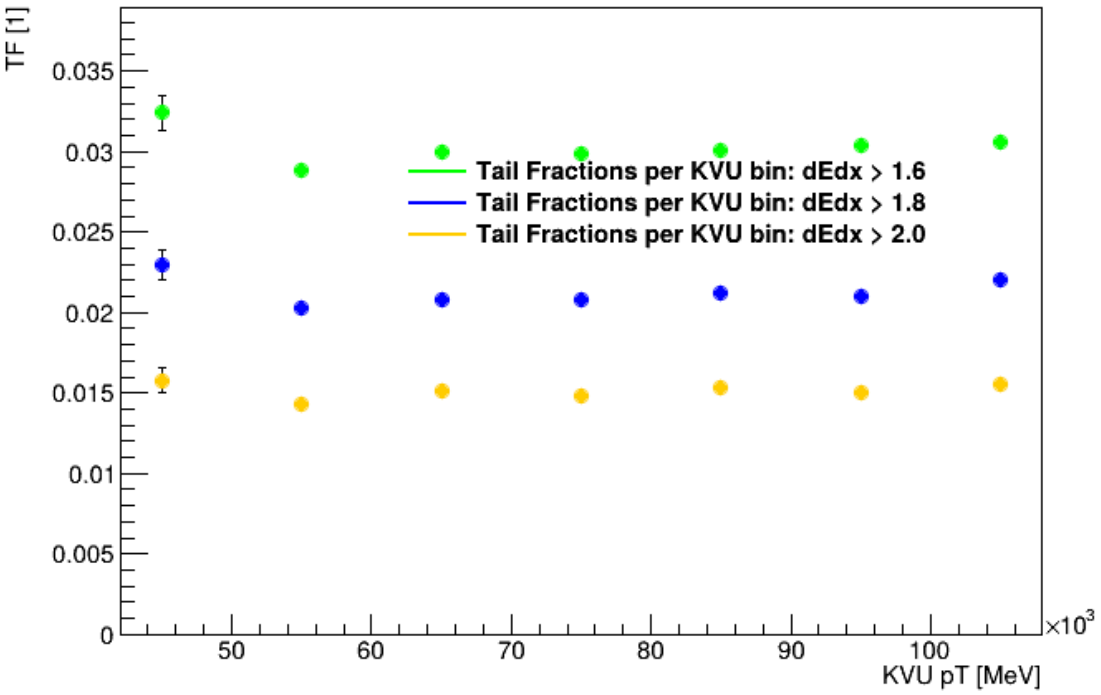


Figure 7.5. Tail fraction percentages in the low-MET control.

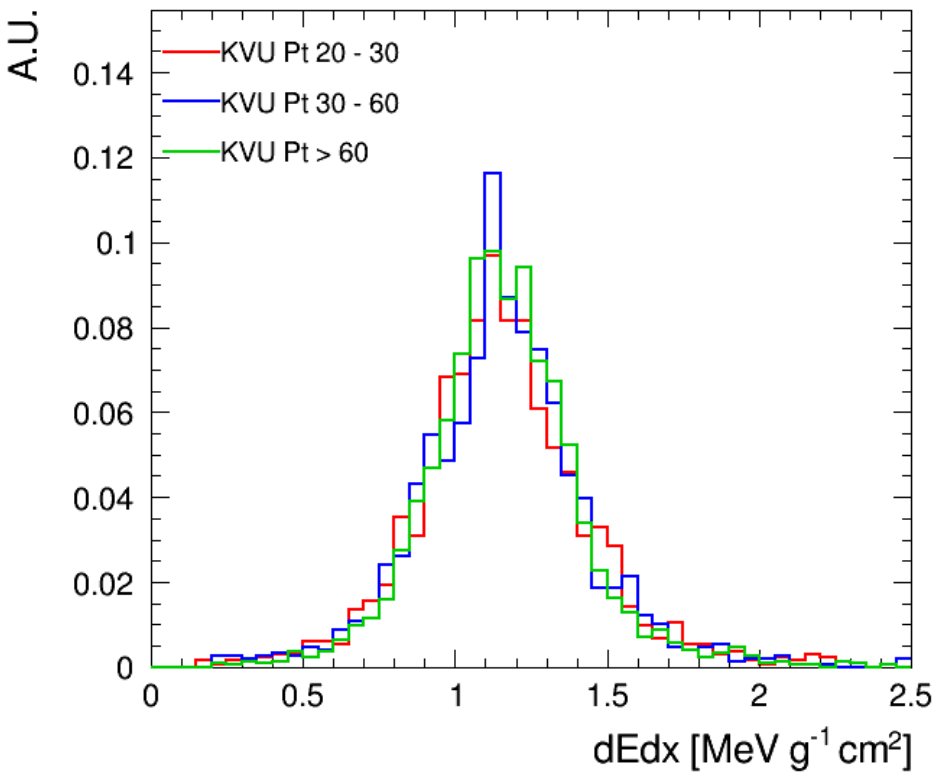


Figure 7.6. dEdx shapes of different slices of p_T in the low-MET control. All slices are normalized to show relative differences.

The results of these regions as well as the signal region can be seen in fig 7.8

To further study the behavior of the $\mathrm{d}E/\mathrm{d}x$ tails and optimize the signal region selection used in the ABCD method, a template-based toy model of the expected background in the signal region is constructed. The toy model is built using templates extracted from data after the baseline event selections have been applied. A $\mathrm{d}E/\mathrm{d}x$ template is obtained from the low-momentum control region, defined as $p_T < 50\,\mathrm{GeV}$, while the p_T template is extracted from the low-$\mathrm{d}E/\mathrm{d}x$ control region, defined as $\mathrm{d}E/\mathrm{d}x < 1.2\,\mathrm{MeV\,g^{-1}\,cm^2}$. These templates are normalized to probability distribution functions and are sampled independently to generate pseudo-events, with each event assigned a randomly sampled $\mathrm{d}E/\mathrm{d}x$ and p_T value.

The generated pseudo-events are then used in a cut-and-count procedure to estimate the expected background yield in the signal region. By scanning over different signal region boundary definitions, the predicted background yields can be compared with simulated signal expectations to optimize sensitivity across a range of signal models. In addition, comparison of the toy model prediction with the nominal ABCD estimate provides a consistency check of the background estimation procedure.

Table 7.8. Inclusive Region background estimation.

Inclusive region					
Channel	High p_T $\mathrm{d}E/\mathrm{d}x \leq 1.2$	Low p_T $\mathrm{d}E/\mathrm{d}x > 1.6$	Low p_T $\mathrm{d}E/\mathrm{d}x \leq 1.2$	High p_T $\mathrm{d}E/\mathrm{d}x > 1.6$	
	B	C	D	Pre. A	Obs. A
Low MET VR	58	1682	1052	36.3 ± 6.0	35
Fake VR	30	663	221	10.0 ± 3.2	15
MIP VR	49	3423	3152	45.1 ± 6.7	42
Electron VR	34	2276	852	12.7 ± 3.6	13
Hadron VR	2	218	0	N/A	0
Muon VR	13	929	2300	32.2 ± 5.7	29
High MET SR	151	1810	2627	$219. \pm 14.$	Blind

7.5.2 Two component $\mathrm{d}E/\mathrm{d}x$ template. The two component $\mathrm{d}E/\mathrm{d}x$ background estimation is done using the $\mathrm{d}E/\mathrm{d}x$ as the final discriminate. This is done

by extracting the background $\mathrm{d}E/\mathrm{d}x$ templates from specific validation regions and then applying the component fits to extract the background estimation in the signal regions. This method relies on the assumption that background consists of only two unique shapes, fakes and MIPs. The background fit is then simplified to two parameters and the resulting background pdf is given by Eq. 7.2.

$$\mathrm{pdf}_{\mathrm{B-only}} = N_{\mathrm{CR}} \cdot (f_{\mathrm{fake}} \cdot \mathrm{pdf}_{\mathrm{fake}} + (1 - f_{\mathrm{fake}}) \cdot \mathrm{pdf}_{\mathrm{MIP}}) \ . \tag{7.2}$$

Where the indivuidal $\mathrm{pdf}_{\mathrm{fake}}$ and $\mathrm{pdf}_{\mathrm{MIP}}$ are extracted from dedicated control regions and the parameters N_{CR} and f_{fake} are left as the component fits.

7.5.2.1 Template Extraction: MIPs. The MIP template, $\mathrm{pdf}_{\mathrm{MIP}}$, is extracted from multiple MIP enhanced regions. There are three sources of MIPs: electrons, muons, and hadrons. The MIP $\mathrm{d}E/\mathrm{d}x$ shape is extracted individually for each source. The resulting $\mathrm{d}E/\mathrm{d}x$ shapes are consistent across the different background sources.

Electrons, muons, and hadrons exhibit the same $\mathrm{d}E/\mathrm{d}x$ shape, indicating that all three background sources are well described by a common MIP $\mathrm{d}E/\mathrm{d}x$ template. This can be seen in Fig. 7.7. The final extracted MIP template is shown in Fig. 7.8.

7.5.3 Template Extraction: Fakes. Fakes do not have a similar $\mathrm{d}E/\mathrm{d}x$ shape to other sources of background due to multiple effects. The reconstructed path length of fake tracklets is miscalculated because the particles producing the hits do not necessary follow the trajectory of the reconstructed tracklet. In addition, fakes can include hits from low-momentum, high- $\mathrm{d}E/\mathrm{d}x$ particles that are not typically reconstructed.

These effects result in a unique $\mathrm{d}E/\mathrm{d}x$ shape that must be extracted separately from other background sources. The fake template, $\mathrm{pdf}_{\mathrm{fake}}$, is extracted from a fake

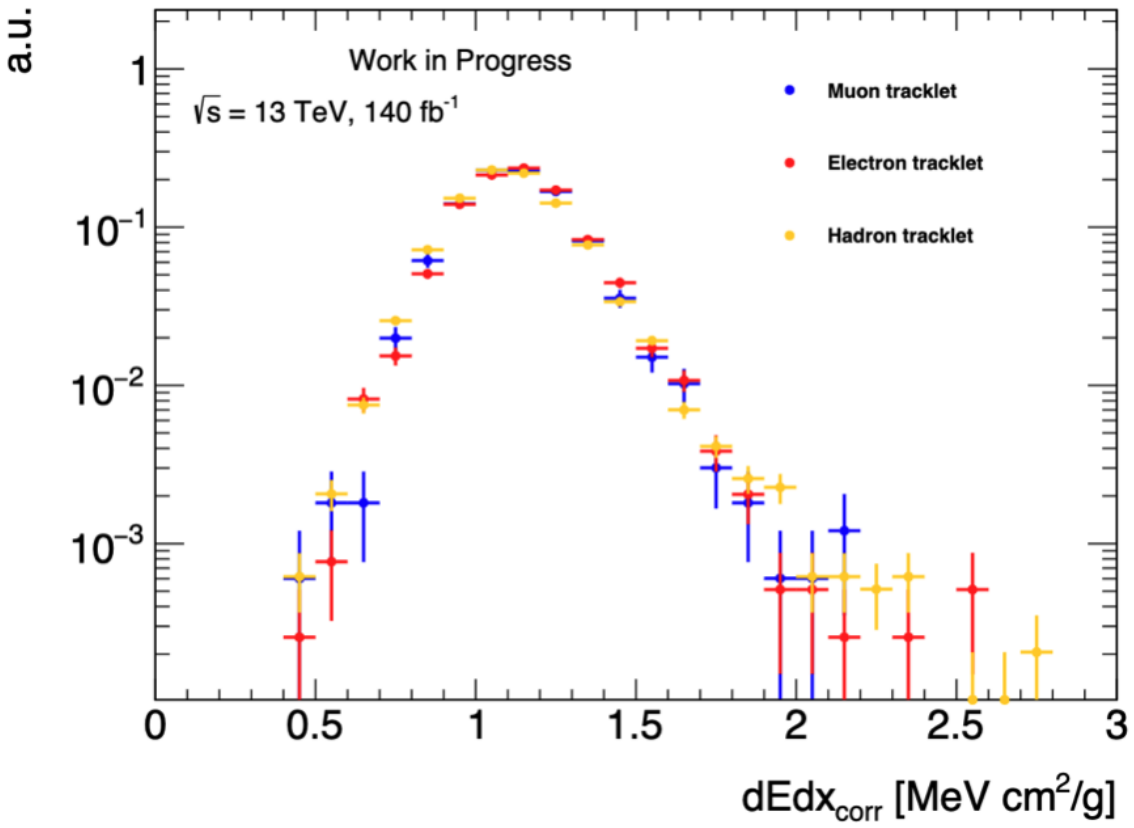


Figure 7.7. Electron, muon, and hadron $\mathrm{d}E/\mathrm{d}x$ templates.

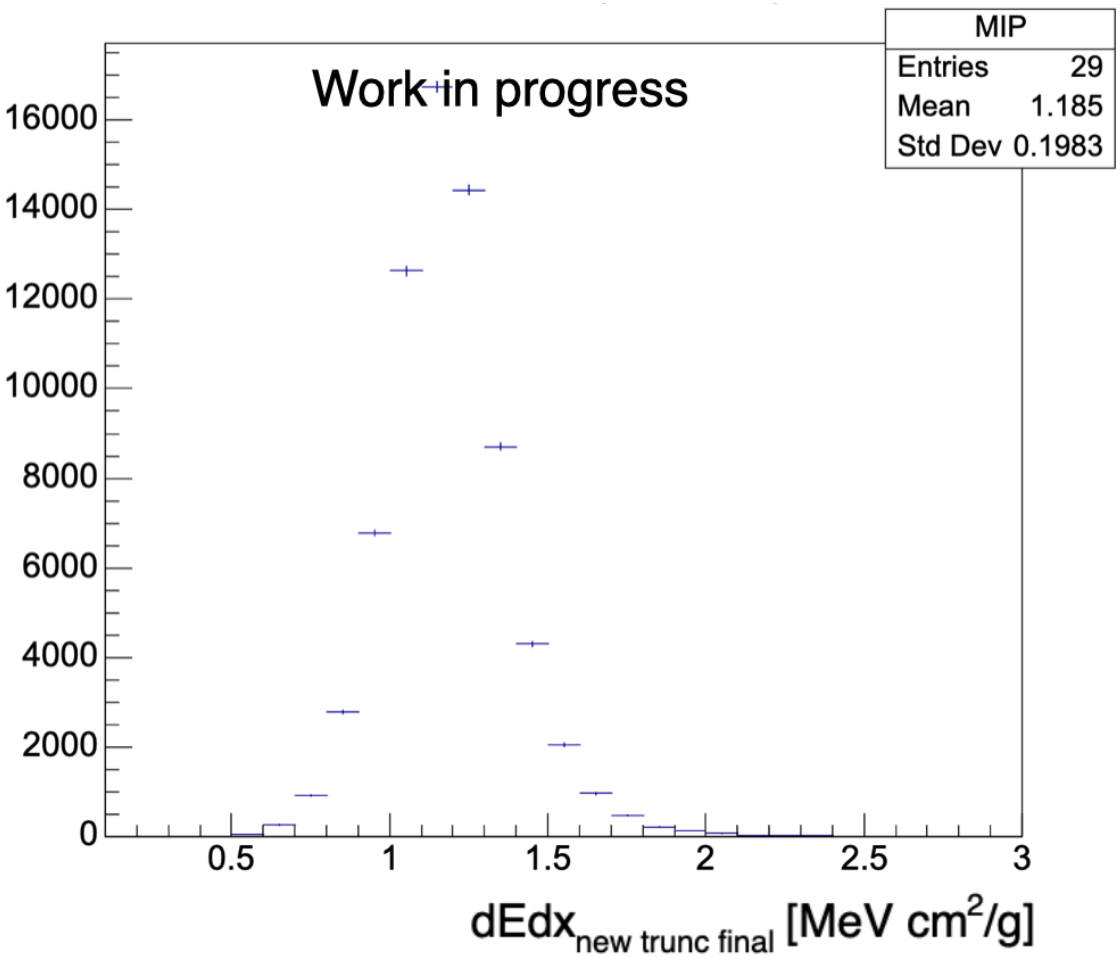


Figure 7.8. Extracted MIP $\mathrm{d}E/\mathrm{d}x$ template, $\mathrm{pdf}_{\mathrm{MIP}}$.

enriched region defined by the selections in Tab. 7.9. The resulting template is shown in Fig. 7.9.

Table 7.9. Tracklet selections used to define the fake enriched region.

Fake Enriched Tracklet Selections	
Calo veto	$E_{\mathrm{T}}^{\mathrm{topoclus40}} < 5$ GeV
Muon isolation	$\Delta R(\text{tracklet, MStrack}^{p_{\mathrm{T}}>10\,\mathrm{GeV}}) > 0.4$
DZ sideband	$1.0 < \mathrm{DZ} < 10.0$ mm

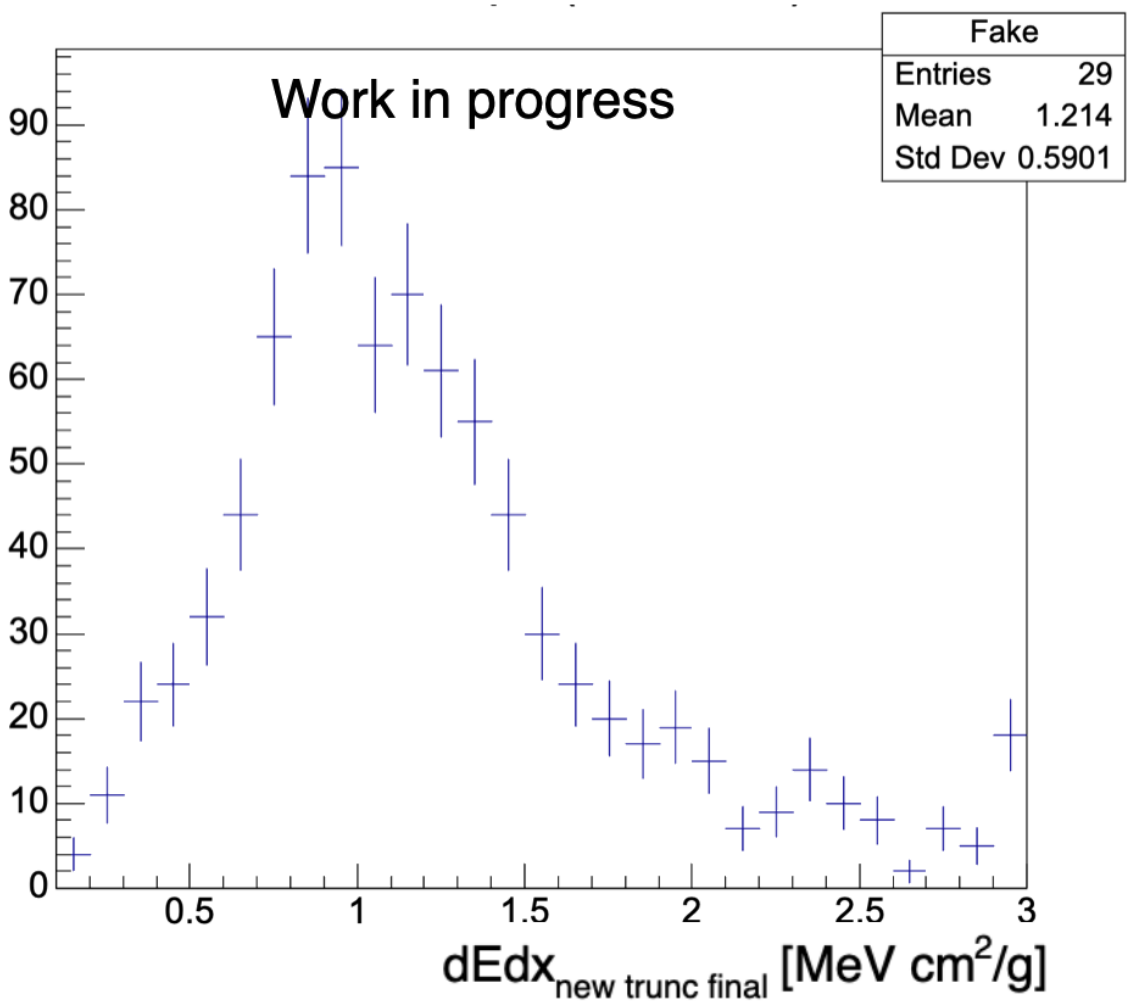
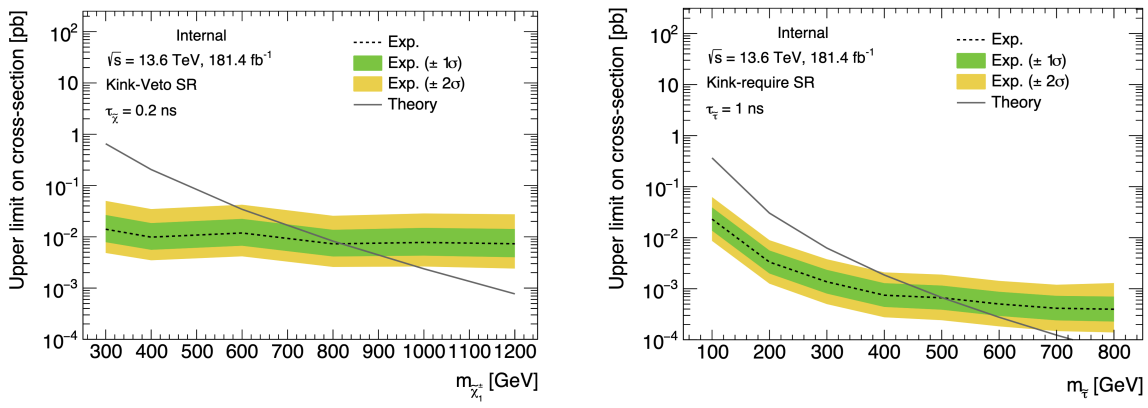


Figure 7.9. Extracted fake $\mathrm{d}E/\mathrm{d}x$ template, $\mathrm{pdf}_{\mathrm{fake}}$.



(a) (b)

Figure 7.10. Expected exclusion limits for $\tilde{\tau}$ and $\tilde{\chi}_1^{\pm}$ models for lifetime of 1 ns.

7.6 Results and Conclusion

The current projected sensitivities for 1 ns $\tilde{\tau}$ and $\tilde{\chi}_1^{\pm}$ benchmark models are shown in Fig. 7.10. Both the ABCD and template-based background estimation methods demonstrate good closure in the validation regions, providing confidence in the robustness of the background prediction. Studies of the correlation between $\mathrm{d}E/\mathrm{d}x$ and p_{T} show no significant dependence, validating the key assumption underlying the ABCD method and supporting its application in the signal region. These studies provide the basis for a search extending sensitivity to charged long-lived particles in the 1 ns lifetime regime.

CHAPTER VIII

CONCLUSION

This dissertation has presented my contributions to particle physics as part of the ATLAS collaboration. The work has focused on long-lived particle searches and on supporting the development and construction of the ITk upgrade in preparation for the HL-LHC era.

In particular, this work contributed to two complementary searches for BSM particles. Within the Disappearing track search, two $\tilde{\tau}$ signal models were incorporated, enabling the search to put limits on a model that was previously unexplored in ATLAS. This search is designed to use tracklets originating from long-lived charged particles that decay within the Inner Detector volume. The analysis reconstructs these tracklets and, for the shortest tracklets, searches for an associated soft pion originating from the decay at the end of the tracklet. This included searches in four channels, three layer with soft pion, three layer without soft pion, four layer with high MET, and four layer with medium MET. The observed data is consistent with the Standard Model predictions to within 2σ, allowing limits to be set on the SUSY scenarios. Exclusion limits were placed at 320 GeV for lifetime of 1ns in the CMSSM $\tilde{\tau}$ coannihilation scenario and 300 GeV for a lifetime of 1ns in the GMSB $\tilde{\tau}$ scenario.

In addition, a new analysis strategy combining disappearing track signatures with high ionization energy loss measurements was developed. This approach will extend the sensitivity to the heavy long-lived particle phase space at lifetimes around 1 ns. The inclusion of ionization energy loss provides an additional discriminating handle that significantly reduces fake backgrounds and enables more robust data driven background estimation techniques. The search is still under development, with expected sensitivity of 500 GeV for 1 ns lifetime in the GMSB $\tilde{\tau}$ scenario and significant improvements for winos are expects as well.

This dissertation has contributed to the development and preparation of the ITk for HL-LHC operation. This includes work on module testing, integration procedures, and validation of detector performance under realistic operating conditions. In particular, studies of thermal cycling and mechanical stability demonstrated the robustness of pixel modules under extreme temperature variations, providing confidence in the long-term reliability of the detector. A contribution of this work was the design and partial construction of dedicated test infrastructure for loaded local supports. These test boxes were developed to enable validation of both stave and ring assemblies under realistic thermal and operational conditions prior to their installation into larger shell structures. Their design addressed critical technical requirements, including efficient environmental control to prevent condensation, flexible accommodation of multiple detector geometries, robust electrical and cooling interfaces, and integrated safety interlocks for detector protection. This infrastructure provides an essential validation stage in the assembly workflow, reducing integration risk and enabling early identification of potential mechanical or electrical issues. These efforts support the successful production, assembly, and deployment of the ITk Inner System, which is critical for maintaining tracking performance in the high pileup environment of the HL-LHC.

Together, these contributions advance both the experimental techniques and detector capabilities required to search for physics beyond the Standard Model. As the LHC continues operation, the methods and detector developments presented in this dissertation will play a role in the continued success of the ATLAS experiment and the search for new physics.

REFERENCES CITED

[1] ATLAS Collaboration. *Search for long-lived chargingand τ-sleptons using final states with a disappearing track in pp collisions at $\sqrt{s} = 13$ TeV with the ATLAS detector*. 2026. arXiv: 2603.08315 [hep-ex]. URL: https://arxiv.org/abs/2603.08315.

[2] CMS Collaboration. *Seeking SUSY*. https://cms.cern/physics/seeking-susy. (Visited on 05/05/2026).

[3] M. E. Peskin. *What is the Hierarchy Problem?* 2025. arXiv: 2505.00694 [hep-ph]. URL: https://arxiv.org/abs/2505.00694.

[4] K. Freese. *DARK MATTER IN GALAXIES AND CLUSTERS*. https://ned.ipac.caltech.edu/level5/Sept17/Freese/Freese2.html. 2026. (Visited on 03/02/2026).

[5] S. Navas et al. 'Review of particle physics'. In: *Phys. Rev. D* 110.3 (2024), p. 030001. DOI: 10.1103/PhysRevD.110.030001.

[6] S. P. MARTIN. 'A SUPERSYMMETRY PRIMER'. In: *Perspectives on Supersymmetry*. WORLD SCIENTIFIC, July 1998, pp. 1–98. ISBN: 9789812839657. DOI: 10.1142/9789812839657_0001. URL: http://dx.doi.org/10.1142/9789812839657_0001.

[7] K. Griest and D. Seckel. 'Three exceptions in the calculation of relic abundances'. eng. In: *Physical review. D, Particles and fields* 43.10 (1991), pp. 3191–3203. ISSN: 0556-2821.

[8] M. Citron et al. 'End of the CMSSM coannihilation strip is nigh'. In: *Physical Review D* 87.3 (Feb. 2013). ISSN: 1550-2368. DOI: 10.1103/physrevd.87.036012. URL: http://dx.doi.org/10.1103/PhysRevD.87.036012.

[9] M. Fujii and T. Yanagida. 'Natural gravitino dark matter and thermal leptogenesis in gauge-mediated supersymmetry-breaking models'. In:

Physics Letters B 549.3–4 (Dec. 2002), pp. 273–283. ISSN: 0370-2693. DOI: 10.1016/s0370-2693(02)02958-1. URL: https://arxiv.org/abs/hep-ph/0208191.

[10] M. Ibe, S. Matsumoto and R. Sato. 'Mass splitting between charged and neutral winos at two-loop level'. In: *Physics Letters B* 721.4–5 (Apr. 2013), pp. 252–260. ISSN: 0370-2693. DOI: 10.1016/j.physletb.2013.03.015. URL: https://arxiv.org/abs/1212.5989.

[11] M. Ibe et al. 'Precise estimate of charged Wino decay rate'. In: *Journal of High Energy Physics* 2023.1 (Jan. 2023). ISSN: 1029-8479. DOI: 10.1007/jhep01(2023)017. URL: http://dx.doi.org/10.1007/JHEP01(2023)017.

[12] ATLAS Collaboration. *THE CERN ACCELERATOR COMPLEX, Complexe des accélérateurs du CERN*. https://cds.cern.ch/record/2693837. 2019. (Visited on 03/02/2026).

[13] H. Bartosik and G. Rumolo. *Performance of the LHC injector chain after the upgrade and potential development*. 2022. arXiv: 2203.09202 [physics.acc-ph]. URL: https://arxiv.org/abs/2203.09202.

[14] ATLAS Collaboration. *Computer generated image of the whole ATLAS detector*. https://cds.cern.ch/record/1095924. 2008. (Visited on 03/02/2026).

[15] C. Grupen, B. A. Shwartz and H. Spieler. *Particle detectors*. eng. Cambridge, UK ; 2008. URL: http://catdir.loc.gov/catdir/enhancements/fy0803/2007036197-t.html.

[16] M. E. Stramaglia. *Calibration Analysis Software for the ATLAS Pixel Detector*. Tech. rep. Geneva: CERN, 2016. DOI: 10.1016/j.nima.2015.11.120. URL: https://cds.cern.ch/record/2027805.

[17] C. Grupen and B. Shwartz. *Particle Detectors*. One Liberty Plaza, 20th Floor, New York, NY 10006, USA: Cambridge University Press, 2008.

[18] J. Pequenao. *Computer generated image of the ATLAS Muons subsystem.* https://cds.cern.ch/record/1095929. 2008. (Visited on 03/02/2026).

[19] ATLAS Collaboration. *Technical Design Reportfor the ATLAS Inner Tracker Strip Detector.* https://cds.cern.ch/record/2257755/. 2017. (Visited on 03/02/2026).

[20] ATLAS Collaboration. *Technical Design Report for the ATLAS Inner Tracker Pixel Detector.* https://cds.cern.ch/record/2285585. 2017. (Visited on 03/02/2026).

[21] *Expected tracking and related performance with the updated ATLAS Inner Tracker layout at the High-Luminosity LHC.* Tech. rep. Geneva: CERN, 2021. URL: https://cds.cern.ch/record/2776651.

[22] *Performance of tracking and vertexing techniques for a disappearing track plus soft track signature with the ATLAS detector.* Tech. rep. All figures including auxiliary figures are available at https://atlas.web.cern.ch/Atlas/GROUPS/PHYSICS/PUBNOTES/ATL-PHYS-PUB-2019-011. Geneva: CERN, 2019. URL: https://cds.cern.ch/record/2669015.

[23] J. Pequenao. 'Event Cross Section in a computer generated image of the ATLAS detector.' 2008. URL: https://cds.cern.ch/record/1096081.

[24] M. and Aaboud et al. 'Electron reconstruction and identification in the ATLAS experiment using the 2015 and 2016 LHC proton-proton collision data at $\sqrt{s}$ = 13 TeV'. In: *The European Physical Journal C* 79.8 (Aug. 2019). ISSN: 1434-6052. DOI: 10.1140/epjc/s10052-019-7140-6. URL: http://dx.doi.org/10.1140/epjc/s10052-019-7140-6.

[25] G. and Aad et al. 'Muon reconstruction performance of the ATLAS detector in proton-proton collision data at $\sqrt{s}$ s =13 TeV'. In: *The European Physical Journal C* 76.5 (May 2016). ISSN: 1434-6052. DOI: 10.1140/epjc/s10052-016-4120-y. URL: http://dx.doi.org/10.1140/epjc/s10052-016-4120-y.

[26] S. Schramm. *ATLAS Jet Reconstruction, Calibration, and Tagging of Lorentz-boosted Objects*. Tech. rep. Geneva: CERN, 2017. URL: https://cds.cern.ch/record/2291608.

[27] M. Cacciari, G. P. Salam and G. Soyez. 'The anti-kt jet clustering algorithm'. In: *Journal of High Energy Physics* 2008.04 (Apr. 2008), pp. 063–063. ISSN: 1029-8479. DOI: 10.1088/1126-6708/2008/04/063. URL: http://dx.doi.org/10.1088/1126-6708/2008/04/063.

[28] *SUSY March 2026 Summary Plot Update*. Tech. rep. Geneva: CERN, 2026. URL: https://cds.cern.ch/record/2957067.

[29] Y. Gol'fand and E. Likhtman. 'Extension of the Algebra of Poincare Group Generators and Violation of P Invariance'. In: *JETP Lett.* 13 (1971). [Pisma Zh. Eksp. Teor. Fiz. **13** (1971) 452], p. 323. DOI: 10.1142/9789814542340_0001.

[30] D. V. Volkov and V. P. Akulov. 'Is the neutrino a goldstone particle?' In: *Phys. Lett. B* 46 (1973), p. 109. DOI: 10.1016/0370-2693(73)90490-5.

[31] J. Wess and B. Zumino. 'Supergauge transformations in four dimensions'. In: *Nucl. Phys. B* 70 (1974), p. 39. DOI: 10.1016/0550-3213(74)90355-1.

[32] J. Wess and B. Zumino. 'Supergauge invariant extension of quantum electrodynamics'. In: *Nucl. Phys. B* 78 (1974), p. 1. DOI: 10.1016/0550-3213(74)90112-6.

[33] S. Ferrara and B. Zumino. 'Supergauge invariant Yang-Mills theories'. In: *Nucl. Phys. B* 79 (1974), p. 413. DOI: 10.1016/0550-3213(74)90559-8.

[34] A. Salam and J. Strathdee. 'Super-symmetry and non-Abelian gauges'. In: *Phys. Lett. B* 51 (1974), p. 353. DOI: 10.1016/0370-2693(74)90226-3.

[35] N. Sakai. 'Naturalness in supersymmetric GUTS'. In: *Z. Phys. C* 11 (1981), p. 153. DOI: 10.1007/BF01573998.

[36] S. Dimopoulos, S. Raby and F. Wilczek. 'Supersymmetry and the scale of unification'. In: *Phys. Rev. D* 24 (1981), p. 1681. DOI: 10.1103/PhysRevD.24.1681.

[37] L. E. Ibáñez and G. G. Ross. 'Low-energy predictions in supersymmetric grand unified theories'. In: *Phys. Lett. B* 105 (1981), p. 439. DOI: 10.1016/0370-2693(81)91200-4.

[38] S. Dimopoulos and H. Georgi. 'Softly broken supersymmetry and SU(5)'. In: *Nucl. Phys. B* 193 (1981), p. 150. DOI: 10.1016/0550-3213(81)90522-8.

[39] G. R. Farrar and P. Fayet. 'Phenomenology of the production, decay, and detection of new hadronic states associated with supersymmetry'. In: *Phys. Lett. B* 76 (1978), p. 575. DOI: 10.1016/0370-2693(78)90858-4.

[40] H. Goldberg. 'Constraint on the Photino Mass from Cosmology'. In: *Phys. Rev. Lett.* 50 (1983), p. 1419. DOI: 10.1103/PhysRevLett.50.1419. Erratum: in: *Phys. Rev. Lett.* 103 (2009), p. 099905. DOI: 10.1103/PhysRevLett.103.099905.

[41] J. Ellis et al. 'Supersymmetric relics from the big bang'. In: *Nucl. Phys. B* 238 (1984), p. 453. DOI: 10.1016/0550-3213(84)90461-9.

[42] M. Ibe, S. Matsumoto and R. Sato. 'Mass Splitting between Charged and Neutral Winos at Two-Loop Level'. In: *Phys. Lett. B* 721 (2013), pp. 252–260. DOI: 10.1016/j.physletb.2013.03.015. arXiv: 1212.5989 [hep-ph].

[43] H. Fukuda et al. 'Higgsino Dark Matter or Not: Role of Disappearing Track Searches at the LHC and Future Colliders'. In: *Phys. Lett. B* 781 (2018), pp. 306–311. DOI: 10.1016/j.physletb.2018.03.088. arXiv: 1703.09675 [hep-ph].

[44] G. F. Giudice et al. 'Gaugino mass without singlets'. In: *JHEP* 12 (1998), p. 027. DOI: 10.1088/1126-6708/1998/12/027. arXiv: hep-ph/9810442.

[45] L. Randall and R. Sundrum. 'Out of this world supersymmetry breaking'. In: *Nucl. Phys. B* 557 (1999), p. 79. DOI: 10.1016/S0550-3213(99)00359-4. arXiv: hep-th/9810155.

[46] M. Papucci, J. T. Ruderman and A. Weiler. 'Natural SUSY Endures'. In: *JHEP* 09 (2012), p. 035. DOI: 10.1007/JHEP09(2012)035. arXiv: 1110.6926 [hep-ph].

[47] R. Barbieri and G. F. Giudice. 'Upper bounds on supersymmetric particle masses'. In: *Nucl. Phys. B* 306 (1988), p. 63. DOI: 10.1016/0550-3213(88)90171-X.

[48] B. de Carlos and J. A. Casas. 'One-loop analysis of the electroweak breaking in supersymmetric models and the fine-tuning problem'. In: *Phys. Lett. B* 309 (1993), p. 320. DOI: 10.1016/0370-2693(93)90940-J. arXiv: hep-ph/9303291.

[49] S. D. Thomas and J. D. Wells. 'Phenomenology of Massive Vectorlike Doublet Leptons'. In: *Phys. Rev. Lett.* 81 (1998), pp. 34–37. DOI: 10.1103/PhysRevLett.81.34. arXiv: hep-ph/9804359.

[50] N. Nagata and S. Shirai. 'Higgsino Dark Matter in High-Scale Supersymmetry'. In: *JHEP* 01 (2015), p. 029. DOI: 10.1007/JHEP01(2015)029. arXiv: 1410.4549 [hep-ph].

[51] D. Albornoz Vásquez, G. Bélanger and C. Bœhm. 'Revisiting light neutralino scenarios in the MSSM'. In: *Phys. Rev. D* 84 (2011), p. 095015. DOI: 10.1103/PhysRevD.84.095015. arXiv: 1108.1338 [hep-ph].

[52] G. Belanger et al. 'WMAP constraints on SUGRA models with non-universal gaugino masses and prospects for direct detection'. In: *Nucl. Phys. B* 706 (2005), p. 411. DOI: 10.1016/j.nuclphysb.2004.11.036. arXiv: hep-ph/0407218.

[53] S. King, J. Roberts and D. Roy. 'Natural dark matter in SUSY GUTs with non-universal gaugino masses'. In: *JHEP* 10 (2007), p. 106. DOI: 10.1088/1126-6708/2007/10/106. arXiv: 0705.4219 [hep-ph].

[54] J. R. Ellis, T. Falk and K. A. Olive. 'Neutralino - Stau coannihilation and the cosmological upper limit on the mass of the lightest supersymmetric particle'. In: *Phys. Lett. B* 444 (1998), pp. 367–372. DOI: 10.1016/S0370-2693(98)01392-6. arXiv: hep-ph/9810360.

[55] T. Jittoh et al. 'Long life stau in the minimal supersymmetric standard model'. In: *Phys. Rev. D* 73 (2006). [Erratum: Phys. Rev. D **87** (2013) 019901], p. 055009. DOI: 10.1103/PhysRevD.73.055009. arXiv: hep-ph/0512197.

[56] S. Kaneko et al. 'Measuring lepton flavor violation at LHC with a long-lived slepton in the coannihilation region'. In: *Phys. Rev. D* 78.11 (2008). [Erratum: Phys. Rev. D **87** (2013) 039904], p. 116013. DOI: 10.1103/PhysRevD.78.116013. arXiv: 0811.0703 [hep-ph].

[57] M. Dine and W. Fischler. 'A phenomenological model of particle physics based on supersymmetry'. In: *Phys. Lett. B* 110 (1982), p. 227. DOI: 10.1016/0370-2693(82)91241-2.

[58] L. Alvarez-Gaumé, M. Claudson and M. B. Wise. 'Low-energy supersymmetry'. In: *Nucl. Phys. B* 207 (1982), p. 96. DOI: 10.1016/0550-3213(82)90138-9.

[59] C. R. Nappi and B. A. Ovrut. 'Supersymmetric extension of the SU(3) x SU(2) x U(1) model'. In: *Phys. Lett. B* 113 (1982), p. 175. DOI: 10.1016/0370-2693(82)90418-X.

[60] A. H. Chamseddine, R. L. Arnowitt and P. Nath. 'Locally Supersymmetric Grand Unification'. In: *Phys. Rev. Lett.* 49 (1982), p. 970. DOI: 10.1103/PhysRevLett.49.970.

[61] R. Barbieri, S. Ferrara and C. A. Savoy. 'Gauge Models with Spontaneously Broken Local Supersymmetry'. In: *Phys. Lett. B* 119 (1982), p. 343. DOI: 10.1016/0370-2693(82)90685-2.

[62] G. L. Kane et al. 'Study of constrained minimal supersymmetry'. In: *Phys. Rev. D* 49 (1994), p. 6173. DOI: 10.1103/PhysRevD.49.6173. arXiv: hep-ph/9312272.

[63] M. Cirelli, N. Fornengo and A. Strumia. 'Minimal dark matter'. In: *Nucl. Phys. B* 753 (2006), pp. 178–194. DOI: 10.1016/j.nuclphysb.2006.07.012. arXiv: hep-ph/0512090.

[64] X. Cid Vidal et al. 'Report from Working Group 3: Beyond the Standard Model physics at the HL-LHC and HE-LHC'. In: *CERN Yellow Rep. Monogr.* 7 (2019). Ed. by A. Dainese et al., pp. 585–865. DOI: 10.23731/CYRM-2019-007.585. arXiv: 1812.07831 [hep-ph].

[65] M. Saito et al. 'Discovery reach for wino and higgsino dark matter with a disappearing track signature at a 100 TeV *pp* collider'. In: *Eur. Phys. J. C* 79.6 (2019), p. 469. DOI: 10.1140/epjc/s10052-019-6974-2. arXiv: 1901.02987 [hep-ph].

[66] R. Capdevilla et al. 'Hunting wino and higgsino dark matter at the muon collider with disappearing tracks'. In: *JHEP* 06 (2021), p. 133. DOI: 10.1007/JHEP06(2021)133. arXiv: 2102.11292 [hep-ph].

[67] R. Capdevilla, F. Meloni and J. Zurita. 'Discovering Electroweak Interacting Dark Matter at Muon Colliders Using Soft Tracks'. In: *Phys. Rev. Lett.* 134.18 (2025), p. 181802. DOI: 10.1103/PhysRevLett.134.181802. arXiv: 2405.08858 [hep-ph].

[68] J. Alwall et al. 'Searching for directly decaying gluinos at the Tevatron'. In: *Phys. Lett. B* 666 (2008), p. 34. DOI: 10.1016/j.physletb.2008.06.065. arXiv: 0803.0019 [hep-ph].

[69] J. Alwall, P. C. Schuster and N. Toro. 'Simplified models for a first characterization of new physics at the LHC'. In: *Phys. Rev. D* 79 (2009), p. 075020. DOI: 10.1103/PhysRevD.79.075020. arXiv: 0810.3921 [hep-ph].

[70] D. Alves et al. 'Simplified models for LHC new physics searches'. In: *J. Phys. G* 39 (2012), p. 105005. DOI: 10.1088/0954-3899/39/10/105005. arXiv: 1105.2838 [hep-ph].

[71] ATLAS Collaboration. 'Search for long-lived charginos based on a disappearing-track signature using 136 fb^{-1} of pp collisions at $\sqrt{s} = 13\,\text{TeV}$ with the ATLAS detector'. In: *Eur. Phys. J. C* 82 (2022), p. 606. DOI: 10.1140/epjc/s10052-022-10489-5. arXiv: 2201.02472 [hep-ex].

[72] ATLAS Collaboration. 'Search for long-lived charginos based on a disappearing-track signature in pp collisions at $\sqrt{s} = 13\,\text{TeV}$ with the ATLAS detector'. In: *JHEP* 06 (2018), p. 022. DOI: 10.1007/JHEP06(2018)022. arXiv: 1712.02118 [hep-ex].

[73] ATLAS Collaboration. *Search for direct pair production of higgsinos by reinterpretation of the disappearing track analysis with* 36.1 fb^{-1} *of* $\sqrt{s} =$ 13 *TeV data collected with the ATLAS experiment*. ATL-PHYS-PUB-2017-019. 2017. URL: https://cds.cern.ch/record/2297480.

[74] ATLAS Collaboration. 'Search for charginos nearly mass degenerate with the lightest neutralino based on a disappearing-track signature in pp collisions at $\sqrt{s} = 8\,\text{TeV}$ with the ATLAS detector'. In: *Phys. Rev. D* 88 (2013), p. 112006. DOI: 10.1103/PhysRevD.88.112006. arXiv: 1310.3675 [hep-ex].

[75] CMS Collaboration. 'Search for disappearing tracks in proton–proton collisions at $\sqrt{s} = 13\,\text{TeV}$'. In: *Phys. Lett. B* 806 (2020), p. 135502. DOI: 10.1016/j.physletb.2020.135502. arXiv: 2004.05153 [hep-ex].

[76] ATLAS Collaboration. 'Search for long-lived charged particles using large specific ionisation loss and time of flight in 140 fb^{-1} of pp collisions at $\sqrt{s} = 13\,\text{TeV}$ with the ATLAS detector'. In: *JHEP* 07 (2025), p. 140. DOI: 10.1007/JHEP07(2025)140. arXiv: 2502.06694 [hep-ex].

[77] CMS Collaboration. 'Search for heavy long-lived charged particles with large ionization energy loss in proton–proton collisions at $\sqrt{s} = 13\,\text{TeV}$'. In: *JHEP* 04 (2024), p. 109. DOI: 10.1007/JHEP04(2025)109. arXiv: 2410.09164 [hep-ex].

[78] ATLAS Collaboration. 'The ATLAS Experiment at the CERN Large Hadron Collider'. In: *JINST* 3 (2008), S08003. DOI: 10.1088/1748-0221/3/08/S08003.

[79] ATLAS Collaboration. *ATLAS Insertable B-Layer: Technical Design Report*. ATLAS-TDR-19; CERN-LHCC-2010-013. 2010. URL: https://cds.cern.ch/record/1291633. Addendum: ATLAS-TDR-19-ADD-1; CERN-LHCC-2012-009. 2012. URL: https://cds.cern.ch/record/1451888.

[80] B. Abbott et al. 'Production and integration of the ATLAS Insertable B-Layer'. In: *JINST* 13 (2018), T05008. DOI: 10.1088/1748-0221/13/05/T05008. arXiv: 1803.00844 [physics.ins-det].

[81] G. Avoni et al. 'The new LUCID-2 detector for luminosity measurement and monitoring in ATLAS'. In: *JINST* 13 (2018), P07017. DOI: 10.1088/1748-0221/13/07/P07017.

[82] ATLAS Collaboration. 'Performance of the ATLAS trigger system in 2015'. In: *Eur. Phys. J. C* 77 (2017), p. 317. DOI: 10.1140/epjc/s10052-017-4852-3. arXiv: 1611.09661 [hep-ex].

[83] ATLAS Collaboration. 'Software and computing for Run 3 of the ATLAS experiment at the LHC'. In: *Eur. Phys. J. C* 85 (2025), p. 234. DOI: 10.1140/epjc/s10052-024-13701-w. arXiv: 2404.06335 [hep-ex]. Erratum: in: *Eur. Phys. J. C* 85 (2025), p. 907. DOI: 10.1140/epjc/s10052-025-14572-5.

[84] ATLAS Collaboration. 'ATLAS data quality operations and performance for 2015–2018 data-taking'. In: *JINST* 15 (2020), P04003. DOI: 10.1088/1748-0221/15/04/P04003. arXiv: 1911.04632 [physics.ins-det].

[85] ATLAS Collaboration. 'Luminosity determination in pp collisions at $\sqrt{s} =$ 13 TeV using the ATLAS detector at the LHC'. In: *Eur. Phys. J. C* 83 (2023), p. 982. DOI: 10.1140/epjc/s10052-023-11747-w. arXiv: 2212.09379 [hep-ex].

[86] ATLAS Collaboration. *2015 start-up trigger menu and initial performance assessment of the ATLAS trigger using Run-2 data*. ATL-DAQ-PUB-2016-001. 2016. URL: https://cds.cern.ch/record/2136007.

[87] ATLAS Collaboration. 'Performance of the missing transverse momentum triggers for the ATLAS detector during Run-2 data taking'. In: *JHEP* 08 (2020), p. 080. DOI: 10.1007/JHEP08(2020)080. arXiv: 2005.09554 [hep-ex].

[88] ATLAS Collaboration. 'Performance of the ATLAS muon triggers in Run 2'. In: *JINST* 15 (2020), P09015. DOI: 10.1088/1748-0221/15/09/p09015. arXiv: 2004.13447 [physics.ins-det].

[89] ATLAS Collaboration. 'Performance of electron and photon triggers in ATLAS during LHC Run 2'. In: *Eur. Phys. J. C* 80 (2020), p. 47. DOI: 10.1140/epjc/s10052-019-7500-2. arXiv: 1909.00761 [hep-ex].

[90] ATLAS Collaboration. 'The ATLAS Simulation Infrastructure'. In: *Eur. Phys. J. C* 70 (2010), p. 823. DOI: 10.1140/epjc/s10052-010-1429-9. arXiv: 1005.4568 [physics.ins-det].

[91] S. Agostinelli et al. 'GEANT4 – a simulation toolkit'. In: *Nucl. Instrum. Meth. A* 506 (2003), p. 250. DOI: 10.1016/S0168-9002(03)01368-8.

[92] T. Sjöstrand, S. Mrenna and P. Skands. 'A brief introduction to PYTHIA 8.1'. In: *Comput. Phys. Commun.* 178 (2008), pp. 852–867. DOI: 10.1016/j.cpc.2008.01.036. arXiv: 0710.3820 [hep-ph].

[93] NNPDF Collaboration, R. D. Ball et al. 'Parton distributions with LHC data'. In: *Nucl. Phys. B* 867 (2013), p. 244. DOI: 10.1016/j.nuclphysb.2012.10.003. arXiv: 1207.1303 [hep-ph].

[94] ATLAS Collaboration. *The Pythia 8 A3 tune description of ATLAS minimum bias and inelastic measurements incorporating the Donnachie–Landshoff diffractive model*. ATL-PHYS-PUB-2016-017. 2016. URL: https://cds.cern.ch/record/2206965.

[95] J. Alwall et al. 'The automated computation of tree-level and next-to-leading order differential cross sections, and their matching to parton shower simulations'. In: *JHEP* 07 (2014), p. 079. DOI: 10.1007/JHEP07(2014)079. arXiv: 1405.0301 [hep-ph].

[96] T. Sjöstrand et al. 'An introduction to PYTHIA 8.2'. In: *Comput. Phys. Commun.* 191 (2015), p. 159. DOI: 10.1016/j.cpc.2015.01.024. arXiv: 1410.3012 [hep-ph].

[97] ATLAS Collaboration. *ATLAS Pythia 8 tunes to 7 TeV data*. ATL-PHYS-PUB-2014-021. 2014. URL: https://cds.cern.ch/record/1966419.

[98] L. Lönnblad and S. Prestel. 'Merging Multi-leg NLO Matrix Elements with Parton Showers'. In: *JHEP* 03 (2013), p. 166. DOI: 10.1007/JHEP03(2013)166. arXiv: 1211.7278 [hep-ph].

[99] NNPDF Collaboration, R. D. Ball et al. 'Parton distributions for the LHC run II'. In: *JHEP* 04 (2015), p. 040. DOI: 10.1007/JHEP04(2015)040. arXiv: 1410.8849 [hep-ph].

[100] W. Beenakker et al. 'Production of Charginos, Neutralinos, and Sleptons at Hadron Colliders'. In: *Phys. Rev. Lett.* 83 (1999), p. 3780. DOI: 10.1103/PhysRevLett.83.3780. arXiv: hep-ph/9906298. Erratum: in: *Phys. Rev. Lett.* 100 (2008), p. 029901. DOI: 10.1103/PhysRevLett.100.029901.

[101] J. Debove, B. Fuks and M. Klasen. 'Threshold resummation for gaugino pair production at hadron colliders'. In: *Nucl. Phys. B* 842 (2011), p. 51. DOI: 10.1016/j.nuclphysb.2010.08.016. arXiv: 1005.2909 [hep-ph].

[102] B. Fuks et al. 'Gaugino production in proton-proton collisions at a center-of-mass energy of 8 TeV'. In: *JHEP* 10 (2012), p. 081. DOI: 10.1007/JHEP10(2012)081. arXiv: 1207.2159 [hep-ph].

[103] B. Fuks et al. 'Precision predictions for electroweak superpartner production at hadron colliders with RESUMMINO'. In: *Eur. Phys. J. C* 73 (2013), p. 2480. DOI: 10.1140/epjc/s10052-013-2480-0. arXiv: 1304.0790 [hep-ph].

[104] J. Fiaschi and M. Klasen. 'Neutralino-chargino pair production at NLO+NLL with resummation-improved parton density functions for LHC Run II'. In: *Phys. Rev. D* 98.5 (2018), p. 055014. DOI: 10.1103/PhysRevD.98.055014. arXiv: 1805.11322 [hep-ph].

[105] G. Bozzi, B. Fuks and M. Klasen. 'Threshold resummation for slepton-pair production at hadron colliders'. In: *Nucl. Phys. B* 777 (2007), p. 157. DOI: 10.1016/j.nuclphysb.2007.03.052. arXiv: hep-ph/0701202.

[106] B. Fuks et al. 'Revisiting slepton pair production at the Large Hadron Collider'. In: *JHEP* 01 (2014), p. 168. DOI: 10.1007/JHEP01(2014)168. arXiv: 1310.2621 [hep-ph].

[107] J. Fiaschi and M. Klasen. 'Slepton pair production at the LHC in NLO+NLL with resummation-improved parton densities'. In: *JHEP* 03 (2018), p. 094. DOI: 10.1007/JHEP03(2018)094. arXiv: 1801.10357 [hep-ph].

[108] J. Fiaschi et al. 'Electroweak superpartner production at 13.6 Tev with Resummino'. In: *Eur. Phys. J. C* 83 (2023), p. 707. DOI: 10.1140/epjc/s10052-023-11888-y. arXiv: 2304.11915 [hep-ph].

[109] C. Borschensky et al. 'Squark and gluino production cross sections in pp collisions at $\sqrt{s} = 13, 14, 33$ and 100 TeV'. In: *Eur. Phys. J. C* 74 (2014), p. 3174. DOI: 10.1140/epjc/s10052-014-3174-y. arXiv: 1407.5066 [hep-ph].

[110] E. Bothmann et al. 'Event generation with Sherpa 2.2'. In: *SciPost Phys.* 7.3 (2019), p. 034. DOI: 10.21468/SciPostPhys.7.3.034. arXiv: 1905.09127 [hep-ph].

[111] T. Gleisberg and S. Höche. 'Comix, a new matrix element generator'. In: *JHEP* 12 (2008), p. 039. DOI: 10.1088/1126-6708/2008/12/039. arXiv: 0808.3674 [hep-ph].

[112] F. Buccioni et al. 'OpenLoops 2'. In: *Eur. Phys. J. C* 79.10 (2019), p. 866. DOI: 10.1140/epjc/s10052-019-7306-2. arXiv: 1907.13071 [hep-ph].

[113] F. Cascioli, P. Maierhöfer and S. Pozzorini. 'Scattering Amplitudes with Open Loops'. In: *Phys. Rev. Lett.* 108 (2012), p. 111601. DOI: 10.1103/PhysRevLett.108.111601. arXiv: 1111.5206 [hep-ph].

[114] A. Denner, S. Dittmaier and L. Hofer. 'COLLIER: A fortran-based complex one-loop library in extended regularizations'. In: *Comput. Phys. Commun.* 212 (2017), pp. 220–238. DOI: 10.1016/j.cpc.2016.10.013. arXiv: 1604.06792 [hep-ph].

[115] S. Schumann and F. Krauss. 'A parton shower algorithm based on Catani–Seymour dipole factorisation'. In: *JHEP* 03 (2008), p. 038. DOI: 10.1088/1126-6708/2008/03/038. arXiv: 0709.1027 [hep-ph].

[116] S. Höche et al. 'A critical appraisal of NLO+PS matching methods'. In: *JHEP* 09 (2012), p. 049. DOI: 10.1007/JHEP09(2012)049. arXiv: 1111.1220 [hep-ph].

[117] S. Höche et al. 'QCD matrix elements + parton showers. The NLO case'. In: *JHEP* 04 (2013), p. 027. DOI: 10.1007/JHEP04(2013)027. arXiv: 1207.5030 [hep-ph].

[118] S. Catani et al. 'QCD Matrix Elements + Parton Showers'. In: *JHEP* 11 (2001), p. 063. DOI: 10.1088/1126-6708/2001/11/063. arXiv: hep-ph/0109231.

[119] S. Höche et al. 'QCD matrix elements and truncated showers'. In: *JHEP* 05 (2009), p. 053. DOI: 10.1088/1126-6708/2009/05/053. arXiv: 0903.1219 [hep-ph].

[120] C. Anastasiou et al. 'High-precision QCD at hadron colliders: Electroweak gauge boson rapidity distributions at next-to-next-to leading order'. In: *Phys. Rev. D* 69 (2004), p. 094008. DOI: 10.1103/PhysRevD.69.094008. arXiv: hep-ph/0312266.

[121] ATLAS Collaboration. 'Performance of the ATLAS track reconstruction algorithms in dense environments in LHC Run 2'. In: *Eur. Phys. J. C*

77 (2017), p. 673. DOI: 10.1140/epjc/s10052-017-5225-7. arXiv: 1704.07983 [hep-ex].

[122] ATLAS Collaboration. *Vertex Reconstruction Performance of the ATLAS Detector at* $\sqrt{s} = 13$ *TeV*. ATL-PHYS-PUB-2015-026. 2015. URL: https://cds.cern.ch/record/2037717.

[123] ATLAS Collaboration. 'Electron and photon performance measurements with the ATLAS detector using the 2015–2017 LHC proton–proton collision data'. In: *JINST* 14 (2019), P12006. DOI: 10.1088/1748-0221/14/12/P12006. arXiv: 1908.00005 [hep-ex].

[124] ATLAS Collaboration. 'Electron reconstruction and identification in the ATLAS experiment using the 2015 and 2016 LHC proton–proton collision data at $\sqrt{s} = 13$ TeV'. In: *Eur. Phys. J. C* 79 (2019), p. 639. DOI: 10.1140/epjc/s10052-019-7140-6. arXiv: 1902.04655 [physics.ins-det].

[125] ATLAS Collaboration. 'Electron and photon efficiencies in LHC Run 2 with the ATLAS experiment'. In: *JHEP* 05 (2024), p. 162. DOI: 10.1007/JHEP05(2024)162. arXiv: 2308.13362 [hep-ex].

[126] ATLAS Collaboration. 'Muon reconstruction and identification efficiency in ATLAS using the full Run 2 *pp* collision data set at $\sqrt{s} = 13$ TeV'. In: *Eur. Phys. J. C* 81 (2021), p. 578. DOI: 10.1140/epjc/s10052-021-09233-2. arXiv: 2012.00578 [hep-ex].

[127] ATLAS Collaboration. 'Studies of the muon momentum calibration and performance of the ATLAS detector with *pp* collisions at $\sqrt{s} = 13$ TeV'. In: *Eur. Phys. J. C* 83 (2023), p. 686. DOI: 10.1140/epjc/s10052-023-11584-x. arXiv: 2212.07338 [hep-ex].

[128] M. Cacciari, G. P. Salam and G. Soyez. 'The anti-k_t jet clustering algorithm'. In: *JHEP* 04 (2008), p. 063. DOI: 10.1088/1126-6708/2008/04/063. arXiv: 0802.1189 [hep-ph].

[129] M. Cacciari, G. P. Salam and G. Soyez. 'FastJet user manual'. In: *Eur. Phys. J. C* 72 (2012), p. 1896. DOI: 10.1140/epjc/s10052-012-1896-2. arXiv: 1111.6097 [hep-ph].

[130] ATLAS Collaboration. 'Jet reconstruction and performance using particle flow with the ATLAS Detector'. In: *Eur. Phys. J. C* 77 (2017), p. 466. DOI: 10.1140/epjc/s10052-017-5031-2. arXiv: 1703.10485 [hep-ex].

[131] ATLAS Collaboration. 'Topological cell clustering in the ATLAS calorimeters and its performance in LHC Run 1'. In: *Eur. Phys. J. C* 77 (2017), p. 490. DOI: 10.1140/epjc/s10052-017-5004-5. arXiv: 1603.02934 [hep-ex].

[132] ATLAS Collaboration. 'Jet energy scale and resolution measured in proton–proton collisions at $\sqrt{s} = 13\,\text{TeV}$ with the ATLAS detector'. In: *Eur. Phys. J. C* 81 (2021), p. 689. DOI: 10.1140/epjc/s10052-021-09402-3. arXiv: 2007.02645 [hep-ex].

[133] ATLAS Collaboration. 'Performance of pile-up mitigation techniques for jets in *pp* collisions at $\sqrt{s} = 8\,\text{TeV}$ using the ATLAS detector'. In: *Eur. Phys. J. C* 76 (2016), p. 581. DOI: 10.1140/epjc/s10052-016-4395-z. arXiv: 1510.03823 [hep-ex].

[134] ATLAS Collaboration. 'The performance of missing transverse momentum reconstruction and its significance with the ATLAS detector using $140\,\text{fb}^{-1}$ of $\sqrt{s} = 13\,\text{TeV}$ *pp* collisions'. In: *Eur. Phys. J. C* 85 (2025), p. 606. DOI: 10.1140/epjc/s10052-025-14062-8. arXiv: 2402.05858 [hep-ex].

[135] A. Hoecker et al. *TMVA - Toolkit for Multivariate Data Analysis*. 2009. arXiv: physics/0703039 [physics.data-an].

[136] ATLAS Collaboration. 'Performance of the reconstruction of large impact parameter tracks in the inner detector of ATLAS'. In: *Eur. Phys. J. C* 83 (2023), p. 1081. DOI: 10.1140/epjc/s10052-023-12024-6. arXiv: 2304.12867 [hep-ex].

[137] M. Baak et al. 'HistFitter software framework for statistical data analysis'. In: *Eur. Phys. J. C* 75 (2015), p. 153. DOI: 10.1140/epjc/s10052-015-3327-7. arXiv: 1410.1280 [hep-ex].

[138] G. Cowan et al. 'Asymptotic formulae for likelihood-based tests of new physics'. In: *Eur. Phys. J. C* 71 (2011), p. 1554. DOI: 10.1140/epjc/s10052-011-1554-0. arXiv: 1007.1727 [physics.data-an]. Erratum: in: *Eur. Phys. J. C* 73 (2013), p. 2501. DOI: 10.1140/epjc/s10052-013-2501-z.

[139] R. D. Cousins, J. T. Linnemann and J. Tucker. 'Evaluation of three methods for calculating statistical significance when incorporating a systematic uncertainty into a test of the background-only hypothesis for a Poisson process'. In: *Nucl. Instrum. Meth. A* 595.2 (2008), p. 480. DOI: 10.1016/j.nima.2008.07.086. arXiv: physics/0702156 [physics.data-an].

[140] A. L. Read. 'Presentation of search results: the CL_s technique'. In: *J. Phys. G* 28 (2002), p. 2693. DOI: 10.1088/0954-3899/28/10/313.

[141] ATLAS Collaboration. *ATLAS surpasses LEP limits in search for compressed higgsinos*. https://atlas.cern/Updates/Briefing/Surpassing-LEP-Limits. 2026. (Visited on 03/02/2026).